

The Vera C. Rubin Observatory Data Preview 1

1

2 VERA C. RUBIN OBSERVATORY TEAM,¹ TATIANA ACERO-CUELLAR ,² EMILY ACOSTA ,¹ CHRISTINA L. ADAIR ,³
3 PRAKRUTH ADARI ,⁴ JENNIFER K. ADELMAN-MCCARTHY ,⁵ ANASTASIA ALEXOV ,¹ RUSS ALLBERY ,¹
4 ROBYN ALLSMAN,¹ YUSRA ALSAYYAD ,⁶ JHONATAN AMADO ,⁵ NATHAN AMOUROUX ,⁷ PIERRE ANTILOGUS ,⁸
5 ALEXIS ARACENA ALCAYAGA,⁹ GONZALO ARAVENA-ROJAS ,⁹ CLAUDIO H. ARAYA CORTES,⁹ ÉRIC AUBOURG ,¹⁰
6 TIM S. AXELROD ,¹¹ JOHN BANOVETZ ,¹² CARLOS BARRÍA,⁹ AMANDA E. BAUER ,¹³ BRIAN J. BAUMAN,¹⁴
7 ELLEN BECHTOL ,¹⁵ KEITH BECHTOL ,^{1,16} ANDREW C. BECKER ,¹⁷ VALERIE R. BECKER ,¹⁸
8 MARK G. BECKETT ,¹⁹ ERIC C. BELLM ,²⁰ PEDRO H. BERNARDINELLI ,²¹ FEDERICA BETTINA BIANCO ,^{2,22,23}
9 ROBERT D. BLUM ,¹⁸ JOANNE BOGART,²⁴ ADAM BOLTON ,³ MICHAEL T. BOOTH,¹ JAMES F. BOSCH ,⁶
10 ALEXANDRE BOUCAUD ,²⁵ DOMINIQUE BOUTIGNY ,⁷ ROBERT A. BOVILL,¹ ANDREW BRADSHAW,^{3,24}
11 JOHAN BREGEON ,²⁶ MASSIMO BRESCIA ,²⁷ BRIAN J. BRONDEL ,²⁸ ALEXANDER BROUGHTON ,²⁴
12 AUDREY BUDLONG ,²⁹ DIMITRI BUFFAT,²⁶ RODOLFO CANESTRARI ,³⁰ NEVEN CAPLAR ,²⁰ JEFFREY L. CARLIN ,¹
13 ROSS CEBALLO ,¹⁸ COLIN ORION CHANDLER ,^{31,20,32} CHIHWAY CHANG ,³³ GLENAVER CHARLES-EMERSON,¹
14 Hsin-Fang CHIANG ,³ JAMES CHIANG ,²⁴ YUMI CHOI ,³⁴ ERIC J. CHRISTENSEN ,⁹ CHARLES F. CLAVER,¹
15 ANDY W. CLEMENTS,¹ JOSEPH J. COCKRUM,¹ JOHANN COHEN-TANUGI ,³⁵ FRANCO COLLEONI,⁹ CÉLINE COMBET ,²⁶
16 ANDREW J. CONNOLLY ,²¹ JULIO EDUARDO CONSTANZO CÓRDOVA ,⁹ HANS E CONTRERAS,⁹
17 JOHN FRANKLIN CRENSHAW ,²¹ SYLVIE DAGORET-CAMPAGNE ,³⁶ SCOTT F. DANIEL,²⁰ FELIPE DARUICH,⁹
18 GUILLAUME DAUBARD ,⁸ GREG DAUES,³⁷ ERIK DENNIHY ,¹ STEPHANIE J. H. DEPPE ,¹⁸ SETH W. DIGEL ,³
19 PETER E. DOHERTY,³⁸ CYRILLE DOUX ,²⁶ ALEX DRLICA-WAGNER ,⁵ GREGORY P. DUBOIS-FELSMANN ,³⁹
20 AMIR E. BAZKIAEI ,⁴⁰ FROSSIE ECONOMOU ,¹ ORION EIGER ,^{3,24} LUKAS EISERT ,³ ALAN M. EISNER ,⁴¹
21 ANTHONY ENGLERT ,⁴² BADEN ERB,⁹ JUAN A. FABREGA,⁹ PARKER FAGRELIUS,¹ KEVIN FANNING ,³
22 ANGELO FAUSTI NETO ,¹ PETER S. FERGUSON ,^{21,16} AGNÈS FERTÉ ,³ KRZYSZTOF FINDEISEN ,²⁰
23 MERLIN FISHER-LEVINE ,⁴³ GLORIA FONSECA ALVAREZ ,³⁴ MICHAEL D. FOSS,³ DOMINIQUE FOUCHÉZ ,⁴⁴
24 DAN C. FUCHS ,³ SHENMING FU ,²⁴ EMMANUEL GANGLER ,⁴⁵ IGOR GAPONENKO,³ JULÉN GARCÍA ,⁴⁶
25 JOHN H GATES,³ RANPAL K. GILL ,²⁸ ENRICO GIRO ,⁴⁷ THOMAS GLANZMAN ,³ ROBINSON GODOY,⁹ IAIN GOODENOW,¹
26 MIRANDA R. GORSUCH ,¹⁶ MICHELLE GOWER ,³⁷ MELISSA L. GRAHAM ,^{20,21} MIKAEL GRANVIK ,^{48,49}
27 SARAH GREENSTREET ,³⁴ WEN GUAN ,¹² THIBAUT GUILLEMIN ,⁷ LEANNE P. GUY ,⁹ DIANE HASCALL,³
28 PATRICK A. HASCALL,³ AREN NATHANIEL HEINZE ,²¹ FABIO HERNANDEZ ,⁵⁰ KENNETH HERNER ,⁵ ARDIS HERROLD,¹
29 CLARE R. HIGGS ,¹⁸ JOSHUA HOBLITT ,¹ ERIN LEIGH HOWARD ,²⁰ MINHEE HYUN ,⁹ AMANDA IBSEN,²⁸
30 PATRICK INGRAHAM ,¹¹ DAVID H. IRVING ,¹⁸ ŽELJKO IVEŽIĆ ,^{1,20} SUZANNE H. JACOBY,¹ BUELL T. JANNUZI ,⁵¹
31 SREEVANI JARUGULA ,⁵ M. JAMES JEE ,^{52,53} TIM JENNESS ,¹ TOBY C. JENNINGS ,³ ANDREA JEREMIE ,⁷
32 GARRETT JERNIGAN,^{54,*} DAVID JIMÉNEZ MEJÍAS,⁹ ANTHONY S. JOHNSON ,³ R. LYNNE JONES ,²⁰
33 ROGER WILLIAM LEWIS JONES ,⁵⁵ CLAIRE JURAMY-GILLES ,⁸ MARIO JURÍĆ ,²¹ STEVEN M. KAHN ,⁵⁶
34 J. BRYCE KALMBACH ,³ YIJUNG KANG ,^{24,9} ARUN KANAWADI ,^{57,6} JEFFREY P. KANTOR,¹ EDWARD KARAVAKIS ,¹²
35 KSHITIJA KELKAR ,⁹ LEE S. KELVIN ,⁶ SCOT J. KLEINMAN,⁵⁸ IVAN V. KOTOV,¹² GÁBOR KOVÁCS ,²¹
36 MIKOLAJ KOWALIK ,³⁷ VICTOR L. KRABBENDAM,¹ K. SIMON KRUGHOFF ,^{1,*} PETR KUBÁNEK ,⁹
37 JACOB A. KURLANDER ,²¹ MILE KUSULJA,²⁶ CRAIG S. LAGE ,⁵³ PAULO J. A. LAGO ,²⁸ KATHERINE LALLOTIS ,⁵⁹
38 TRAVIS LANGE ,³ DIDIER LAPORTE,⁸ RYAN M. LAU ,³⁴ JUAN CARLOS LAZARTE,³ QUENTIN LE BOULC'H ,⁵⁰
39 PIERRE-FRANÇOIS LÉGET ,⁶ LAURENT LE GUILLOU ,⁸ BENJAMIN LEVINE ,⁴ MING LIANG,¹ SHUANG LIANG,³
40 KIAN-TAT LIM ,³ ANJA VON DER LINDEN ,⁴ HUAN LIN ,⁵ MARGAUX LOPEZ ,³ JUAN J. LOPEZ TORO,⁹
41 PETER LOVE,⁵⁵ ROBERT H. LUPTON ,⁶ NATE B. LUST ,⁶ LAUREN A. MACARTHUR ,⁶ SEAN PATRICK MACBRIDE ,⁶⁰
42 GREG M. MADEJSKI,²⁴ GABRIELE MAINETTI ,⁵⁰ STEVEN J. MARGHEIM ,²⁸ THOMAS W. MARKIEWICZ ,³
43 PHIL MARSHALL ,³ STUART MARSHALL,²⁴ GUIDO MAULEN,⁹ SIDNEY MAU ,⁵⁷ MORGAN MAY,^{61,12}
44 JEREMY MCCORMICK ,³ DAVID MCKAY ,⁶² ROBERT MCKERCHER,¹ GUILLEM MEGIAS HOMAR ,⁶³
45 AARON M. MEISNER ,³⁴ FELIPE MENANTEAU,³⁷ HEATHER R. MENTZER ,⁴¹ KRISTEN METZGER,¹⁸
46 JOSHUA E. MEYERS ,²⁴ MICHELLE MILLER,³⁴ DAVID J. MILLS,¹ JOACHIM MOEYENS ,²¹ MARC MONIEZ,³⁶
47 FRED E. MOOLEKAMP ,⁶⁴ C. A. L. MORALES MARÍN ,⁹ FRITZ MUELLER ,³ JAMES R. MULLANEY ,⁶⁵
48 FREDDY MUÑOZ ARANCIBIA,¹ KATE NAPIER ,²⁴ HOMER NEAL,³ ERIC H. NELSEN, JR. ,⁵ JEREMY NEVEU ,³⁶
49 TIMOTHY NOBLE,⁶⁶ ERFAN NOURBAKHSH ,⁶ KNUT OLSEN ,³⁴ WILLIAM O'MULLANE ,⁹ DMITRY ONOPRIENKO,³

50 MARCO ORIUNNO ^{id},³ SHAWN OSIER,³ RUSSELL E. OWEN,²⁰ AASHAY PAI ^{id},³³ JOHN K. PAREJKO ^{id},²⁰ HYE YUN PARK ^{id},⁵⁷
 51 JAMES B. PARSONS,^{37,*} MARIA T. PATTERSON ^{id},²⁰ MARINA S. PAVLOVIC ^{id},⁹ KARLA PEÑA RAMÍREZ ^{id},⁹
 52 JOHN R. PETERSON ^{id},⁶⁷ STEPHEN R. PIETROWICZ ^{id},³⁷ ANDRÉS A. PLAZAS MALAGÓN ^{id},^{3,24} REBEKAH POLEN,⁵⁷
 53 HANNAH MARY MARGARET POLLEK,³ PAUL A. PRICE ^{id},⁶ BRUNO C. QUINT ^{id},¹ JOSÉ MIGUEL QUINTERO MARIN,⁹
 54 MARKUS RABUS ^{id},⁶⁸ BENJAMIN RACINE ^{id},⁴⁴ VELJKO RADEKA,¹² MANON RAMEL,²⁶ ARIANNA RANABHAT ^{id},⁴⁰
 55 ANDREW P. RASMUSSEN ^{id},²⁴ DAVID A. RATHFELDER,⁶⁹ MEREDITH L. RAWLS ^{id},^{20,21} SOPHIE L. REED ^{id},⁶
 56 KEVIN A. REIL ^{id},³ DAVID J. REISS,²⁰ MICHAEL A. REUTER ^{id},¹ TIAGO RIBEIRO ^{id},¹ MARINA RICCI ^{id},²⁵
 57 MICKAEL RIGAULT ^{id},⁷⁰ VINCENT J. RIOT ^{id},¹⁴ STEVEN M. RITZ ^{id},⁴¹ MARIO F. RIVERA RIVERA,⁹
 58 BRANT E. ROBERTSON ^{id},⁷¹ WILLIAM ROBY ^{id},³⁹ GABRIELE RODEGHIERO ^{id},⁷² AARON ROODMAN ^{id},²⁴
 59 LUCA ROSIGNOLI ^{id},^{73,72} CÉCILE ROUCELLE ^{id},²⁵ MATTHEW R. RUMORE ^{id},¹² STEFANO RUSSO,⁸ ELI S. RYKOFF ^{id},²⁴
 60 ANDREI SALNIKOV ^{id},³ BRUNO O. SÁNCHEZ ^{id},⁴⁴ DAVID SANMARTIN ^{id},⁹ CLARE SAUNDERS ^{id},⁶ RAFE H. SCHINDLER,²⁴
 61 SAMUEL J. SCHMIDT ^{id},⁵³ JACQUES SEBAG,⁹ NIMA SEDAGHAT ^{id},²⁰ BRIAN SELVY,¹
 62 EDGARD ESTEBAN SEPULVEDA VALENZUELA,⁹ GONZALO SERICHE ^{id},⁹ JACQUELINE C. SERON-NAVARRETE ^{id},⁹
 63 IGNACIO SEVILLA-NOARBE ^{id},⁷⁴ ALYSHA B. SHUGART ^{id},⁹ JONATHAN SICK ^{id},^{75,1} CRISTIÁN SILVA ^{id},⁹
 64 MATHEW C. SIMS ^{id},⁷⁶ JALADH SINGHAL ^{id},³⁹ KEVIN BENJAMIN SIRUNO,⁹ COLIN T. SLATER ^{id},²⁰ BRIANNA M. SMART ^{id},²⁰
 65 ADAM SNYDER ^{id},⁵³ CHRISTINE SOLDAHL,³ IOANA SOTUELA ELORRIAGA ^{id},⁹ BRIAN STALDER ^{id},¹
 66 HERNAN STOCKEBRAND ^{id},⁹ ALAN L. STRAUSS ^{id},¹⁸ MICHAEL A. STRAUSS ^{id},⁶ CHRISTOPHER W. STUBBS ^{id},^{77,78,79}
 67 KRZYSZTOF SUBERLAK ^{id},²⁰ IAN S. SULLIVAN ^{id},²⁰ JOHN D. SWINBANK ^{id},^{80,6} DIEGO TAPIA ^{id},⁹ ALESSIO TARANTO ^{id},^{72,73}
 68 DAN S. TARANU ^{id},⁶ JOHN GREGG THAYER ^{id},³ SANDRINE THOMAS ^{id},¹⁸ ADAM J. THORNTON ^{id},¹ ROBERTO TIGHE,⁹
 69 LAURA TORIBIO SAN CIPRIANO,⁷⁴ TE-WEI TSAI ^{id},¹ DOUGLAS L. TUCKER ^{id},⁵ MAX TURRI,³ J. ANTHONY TYSON ^{id},⁵³
 70 ELANA K. URBACH ^{id},⁷⁹ YOUSUKE UTSUMI ^{id},⁸¹ BRIAN VAN KLAVEREN,³ WOUTER VAN REEVEN ^{id},⁹
 71 PETER ANTHONY VAUCHER ^{id},³ PAULINA VENEGAS ^{id},²⁸ APRAJITA VERMA ^{id},⁸² ANTONIA SIERRA VILLARREAL ^{id},³
 72 STELIOS VOUTSINAS ^{id},¹ CHRISTOPHER W. WALTER ^{id},⁵⁷ YUANKUN (DAVID) WANG ^{id},²¹ CHRISTOPHER Z. WATERS ^{id},⁶
 73 CHRISTINA C. WILLIAMS ^{id},³⁴ BETH WILLMAN ^{id},⁸³ MATTHIAS WITTMEN ^{id},³ W. M. WOOD-VASEY ^{id},⁸⁴ WEI YANG ^{id},³
 74 ZHAOYU YANG ^{id},¹² BRIAN P. YANNY ^{id},⁵ PETER YOACHIM ^{id},²⁰ TIANQING ZHANG ^{id},⁸⁴ CONGHAO ZHOU ^{id},⁴¹ AND
 75 DANICA ŽILKOVÁ ^{id},²⁸

76 ¹Vera C. Rubin Observatory Project Office, 950 N. Cherry Ave., Tucson, AZ 85719, USA

77 ²Department of Physics and Astronomy, University of Delaware, Newark, DE 19716-2570, USA

78 ³SLAC National Accelerator Laboratory, 2575 Sand Hill Rd., Menlo Park, CA 94025, USA

79 ⁴Department of Physics and Astronomy, Stony Brook University, Stony Brook, NY 11794, USA

80 ⁵Fermi National Accelerator Laboratory, P. O. Box 500, Batavia, IL 60510, USA

81 ⁶Department of Astrophysical Sciences, Princeton University, Princeton, NJ 08544, USA

82 ⁷Université Savoie Mont-Blanc, CNRS/IN2P3, LAPP, 9 Chemin de Bellevue, F-74940 Annecy-le-Vieux, France

83 ⁸Sorbonne Université, Université Paris Cité, CNRS/IN2P3, LPNHE, 4 place Jussieu, F-75005 Paris, France

84 ⁹Vera C. Rubin Observatory, Avenida Juan Cisternas #1500, La Serena, Chile

85 ¹⁰Université Paris Cité, CNRS/IN2P3, CEA, APC, 4 rue Elsa Morante, F-75013 Paris, France

86 ¹¹Steward Observatory, The University of Arizona, 933 N. Cherry Ave., Tucson, AZ 85721, USA

87 ¹²Brookhaven National Laboratory, Upton, NY 11973, USA

88 ¹³Yerkes Observatory, 373 W. Geneva St., Williams Bay, WI 53191, USA

89 ¹⁴Lawrence Livermore National Laboratory, 7000 East Avenue, Livermore, CA 94550, USA

90 ¹⁵Wisconsin IceCube Particle Astrophysics Center, University of Wisconsin—Madison, Madison, WI 53706, USA

91 ¹⁶Department of Physics, University of Wisconsin-Madison, Madison, WI 53706, USA

92 ¹⁷Amazon Web Services, Seattle, WA 98121, USA

93 ¹⁸Vera C. Rubin Observatory/NSF NOIRLab, 950 N. Cherry Ave., Tucson, AZ 85719, USA

94 ¹⁹Institute for Astronomy, University of Edinburgh, Royal Observatory, Blackford Hill, Edinburgh EH9 3HJ, UK

95 ²⁰University of Washington, Dept. of Astronomy, Box 351580, Seattle, WA 98195, USA

96 ²¹Institute for Data-intensive Research in Astrophysics and Cosmology, University of Washington, 3910 15th Avenue NE, Seattle, WA
 97 98195, USA

98 ²²Data Science Institute, University of Delaware, Newark, DE 19717 USA

99 ²³Joseph R. Biden, Jr., School of Public Policy and Administration, University of Delaware, Newark, DE 19717 USA

100 ²⁴Kavli Institute for Particle Astrophysics and Cosmology, SLAC National Accelerator Laboratory, 2575 Sand Hill Rd., Menlo Park, CA
 101 94025, USA

102 ²⁵Université Paris Cité, CNRS/IN2P3, APC, 4 rue Elsa Morante, F-75013 Paris, France

103 ²⁶Université Grenoble Alpes, CNRS/IN2P3, LPSC, 53 avenue des Martyrs, F-38026 Grenoble, France

104 ²⁷Department of Physics "E. Pancini", University Federico II of Napoli, Via Cintia, 80126 Napoli, Italy

105 ²⁸Vera C. Rubin Observatory/NSF NOIRLab, Avenida Juan Cisternas #1500, La Serena, Chile

- 106 ²⁹ *University of Washington, Dept. of Physics, Box 351580, Seattle, WA 98195, USA*
- 107 ³⁰ *INAF Istituto di Astrofisica Spaziale e Fisica Cosmica di Palermo, Via Ugo la Malfa 153, 90146, Palermo, Italy*
- 108 ³¹ *LSST Interdisciplinary Network for Collaboration and Computing, Tucson, USA*
- 109 ³² *Department of Astronomy and Planetary Science, Northern Arizona University, P.O. Box 6010, Flagstaff, AZ 86011, USA*
- 110 ³³ *Department of Astronomy and Astrophysics, University of Chicago, 5640 South Ellis Avenue, Chicago, IL 60637, USA*
- 111 ³⁴ *NSF NOIRLab, 950 N. Cherry Ave., Tucson, AZ 85719, USA*
- 112 ³⁵ *LPCA, Université Clermont-Auvergne, CNRS/IN2P3, Clermont-Ferrand, France*
- 113 ³⁶ *Université Paris-Saclay, CNRS/IN2P3, IJCLab, 15 Rue Georges Clemenceau, F-91405 Orsay, France*
- 114 ³⁷ *NCSA, University of Illinois at Urbana-Champaign, 1205 W. Clark St., Urbana, IL 61801, USA*
- 115 ³⁸ *Smithsonian Astrophysical Observatory, 60 Garden St., Cambridge MA 02138, USA*
- 116 ³⁹ *Caltech/IPAC, California Institute of Technology, MS 100-22, Pasadena, CA 91125-2200, USA*
- 117 ⁴⁰ *Australian Astronomical Optics, Macquarie University, North Ryde, NSW, Australia*
- 118 ⁴¹ *Santa Cruz Institute for Particle Physics and Physics Department, University of California–Santa Cruz, 1156 High St., Santa Cruz, CA 95064, USA*
- 119
- 120 ⁴² *Department of Physics, Brown University, 182 Hope Street, Providence, RI 02912, USA*
- 121 ⁴³ *D4D CONSULTING LTD., Suite 1 Second Floor, Everdene House, Deansleigh Road, Bournemouth, UK BH7 7DU*
- 122 ⁴⁴ *Aix Marseille Université, CNRS/IN2P3, CPPM, 163 avenue de Luminy, F-13288 Marseille, France*
- 123 ⁴⁵ *Université Clermont Auvergne, CNRS/IN2P3, LPCA, 4 Avenue Blaise Pascal, F-63000 Clermont-Ferrand, France*
- 124 ⁴⁶ *C. Iñaki Goenaga, 5, 20600, Guipúzcoa, Spain*
- 125 ⁴⁷ *INAF Osservatorio Astronomico di Trieste, Via Giovan Battista Tiepolo 11, 34143, Trieste, Italy*
- 126 ⁴⁸ *Department of Physics, P.O. Box 64, 00014 University of Helsinki, Finland*
- 127 ⁴⁹ *Asteroid Engineering Laboratory, Luleå University of Technology, Box 848, SE-981 28 Kiruna, Sweden*
- 128 ⁵⁰ *CNRS/IN2P3, CC-IN2P3, 21 avenue Pierre de Coubertin, F-69627 Villeurbanne, France*
- 129 ⁵¹ *University of Arizona, Department of Astronomy and Steward Observatory, 933 N. Cherry Ave, Tucson, AZ 85721, USA*
- 130 ⁵² *Department of Astronomy, Yonsei University, 50 Yonsei-ro, Seoul 03722, Republic of Korea*
- 131 ⁵³ *Physics Department, University of California, One Shields Avenue, Davis, CA 95616, USA*
- 132 ⁵⁴ *Space Sciences Lab, University of California, 7 Gauss Way, Berkeley, CA 94720-7450, USA*
- 133 ⁵⁵ *Lancaster University, Lancaster, UK*
- 134 ⁵⁶ *Physics Department, University of California, 366 Physics North, MC 7300 Berkeley, CA 94720, USA*
- 135 ⁵⁷ *Department of Physics, Duke University, Durham, NC 27708, USA*
- 136 ⁵⁸ *Astromanager LLC, 63 Halaí St, Hilo, 96720 Hawaii, USA*
- 137 ⁵⁹ *Center for Cosmology and Astro-Particle Physics, The Ohio State University, Columbus, OH 43210, USA*
- 138 ⁶⁰ *Physik-Institut, University of Zurich, Winterthurerstrasse 190, 8057 Zurich, Switzerland*
- 139 ⁶¹ *Department of Physics Columbia University, New York, NY 10027, USA*
- 140 ⁶² *EPCC, University of Edinburgh, 47 Potterrow, Edinburgh, EH8 9BT, UK*
- 141 ⁶³ *Division of Physics, Mathematics and Astronomy, California Institute of Technology, Pasadena, CA 91125, USA*
- 142 ⁶⁴ *soZen Inc., 105 Clearview Dr, Penfield, NY 14526*
- 143 ⁶⁵ *Astrophysics Research Cluster, School of Mathematical and Physical Sciences, University of Sheffield, Sheffield, S3 7RH, United Kingdom*
- 144
- 145 ⁶⁶ *Science and Technology Facilities Council, Rutherford Appleton Laboratory, Harwell, UK*
- 146 ⁶⁷ *Department of Physics and Astronomy, Purdue University, 525 Northwestern Ave., West Lafayette, IN 47907, USA*
- 147 ⁶⁸ *Departamento de Matemática y Física Aplicadas, Facultad de Ingeniería, Universidad Católica de la Santísima Concepción, Alonso de Rivera 2850, Concepción, Chile*
- 148
- 149 ⁶⁹ *AURA, 950 N. Cherry Ave., Tucson, AZ 85719, USA*
- 150 ⁷⁰ *Université Claude Bernard Lyon 1, CNRS/IN2P3, IP2I, 4 Rue Enrico Fermi, F-69622 Villeurbanne, France*
- 151 ⁷¹ *Department of Astronomy and Astrophysics, University of California–Santa Cruz, 1156 High St., Santa Cruz, CA 95064, USA*
- 152 ⁷² *INAF Osservatorio di Astrofisica e Scienza dello Spazio Bologna, Via P. Gobetti 93/3, 40129, Bologna, Italy*
- 153 ⁷³ *Department of Physics and Astronomy (DIFA), University of Bologna, Via P. Gobetti 93/2, 40129, Bologna, Italy*
- 154 ⁷⁴ *Centro de Investigaciones Energéticas, Medioambientales y Tecnológicas, Av. Complutense 40, 28040 Madrid, Spain*
- 155 ⁷⁵ *J.Sick Codes Inc., Penetanguishene, Ontario, Canada*
- 156 ⁷⁶ *Science and Technology Facilities Council, UK Research and Innovation, Polaris House, North Star Avenue, Swindon, SN2 1SZ, UK*
- 157 ⁷⁷ *Department of Astronomy, Center for Astrophysics, Harvard University, 60 Garden St., Cambridge, MA 02138, USA*
- 158 ⁷⁸ *Center for Astrophysics, Harvard & Smithsonian, 60 Garden Street, Cambridge, MA 02138*
- 159 ⁷⁹ *Department of Physics, Harvard University, 17 Oxford St., Cambridge MA 02138, USA*
- 160 ⁸⁰ *ASTRON, Oude Hoogeveensedijk 4, 7991 PD, Dwingeloo, The Netherlands*
- 161 ⁸¹ *National Astronomical Observatory of Japan, Chile Observatory, Los Abedules 3085, Vitacura, Santiago, Chile*
- 162 ⁸² *Department of Physics, University of Oxford, Denys Wilkinson Building, Keble Road, Oxford, OX1 3RH, UK*

⁸³*LSST Discovery Alliance, 933 N. Cherry Ave., Tucson, AZ 85719, USA*

⁸⁴*Department of Physics and Astronomy, University of Pittsburgh, 3941 O'Hara Street, Pittsburgh, PA 15260, USA*

(Dated: May 11, 2026)

ABSTRACT

We present Rubin Data Preview 1 (DP1), the first data from the National Science Foundation–Department of Energy Vera C. Rubin Observatory, comprising raw and calibrated single-epoch images, coadds, difference images, detection catalogs, and ancillary data products. DP1 is based on 1792 optical-near-infrared exposures acquired over 48 distinct nights by the Rubin Commissioning Camera (LSSTComCam), on the Simonyi Survey Telescope at the Summit Facility on Cerro Pachón, Chile in late 2024. DP1 covers $\sim 15 \text{ deg}^2$ distributed across seven roughly equal-sized noncontiguous fields, each independently observed in six broad photometric bands, *ugrizy*. The median FWHM of the point-spread function across all bands is approximately $1''.14$, with the sharpest images reaching about $0''.58$. The 5σ point-source depths for coadded images in the deepest field, the Extended Chandra Deep Field South, are $u = 24.55$, $g = 26.18$, $r = 25.96$, $i = 25.71$, $z = 25.07$, $y = 23.1$. Other fields are no more than 2.2 mag shallower in any band, where they have nonzero coverage. DP1 contains approximately 2.3 million distinct astrophysical objects, of which 1.6 million are extended in at least one band in coadds, and 431 solar system objects, of which 93 are new discoveries. DP1 is approximately 3.5 TB in size and is available to Vera C. Rubin Observatory data rights holders via the Rubin Science Platform, a cloud-based environment for the analysis of petascale astronomical data. While small compared to future LSST releases, its high quality and diversity of data support a broad range of early science investigations ahead of full operations in 2026.

Keywords: Rubin Observatory – LSST

1. INTRODUCTION

The National Science Foundation (NSF)–Department of Energy (DOE) Vera C. Rubin Observatory is a ground-based, wide-field optical-near-infrared facility located on Cerro Pachón in northern Chile. Named in honor of Vera C. Rubin, a pioneering astronomer whose groundbreaking work in the 20th century provided the first convincing evidence for the existence of dark matter (V. C. Rubin & W. K. Ford 1970; V. C. Rubin et al. 1980), the observatory’s prime mission is to carry out the Legacy Survey of Space and Time (LSST) (Ž. Ivezić et al. 2019a). This 10-yr survey is designed to obtain rapid-cadence, multiband imaging of the entire visible southern sky approximately every 3–4 nights. Over its main $18,000 \text{ deg}^2$ footprint, the LSST is expected to reach a depth of ~ 27 mag in the *r*-band, with ~ 800 visits per pointing in all filters (F. B. Bianco et al. 2022).

The Rubin Observatory system consists of four main components: the Simonyi Survey Telescope, featuring an 8.4 m diameter (6.5 m effective aperture) primary mirror that delivers a wide field of view; the 3.2-gigapixel LSST Science Camera (LSSTCam), capable of imag-

ing 9.6 deg^2 per exposure⁸⁵ with seeing-limited quality in six broadband filters, *ugrizy* (320–1050 nm); an automated Data Management System that processes and archives tens of terabytes of data per night, generating science-ready data products within minutes for a global community of scientists; and an Education and Public Outreach (EPO) program that provides real-time data access, interactive tools, and educational content to engage the public. The integrated system’s étendue⁸⁶ of $319 \text{ m}^2 \text{ deg}^2$, is over an order of magnitude larger than that of any previous optical observatory, enabling a fast, large-scale survey with exceptional depth in a fraction of the time compared to other observatories.

The observatory’s design is driven by four key science themes: probing dark energy and dark matter; taking an inventory of the solar system; exploring the transient and variable optical sky; and mapping the Milky Way (Ž. Ivezić et al. 2019a). These themes inform the op-

⁸⁵ We define an “exposure” as the process of exposing all detectors in the focal plane. It is synonymous with the term “visit” in DP1. By contrast, an “image” is the output of a single detector following an exposure.

⁸⁶ The product of the primary mirror area and the angular area of its field of view for a given set of observing conditions.

* Author is deceased

224 timization of a range of system parameters, including
 225 image quality; photometric and astrometric accuracy;
 226 single-visit depth; coadded survey depth; the filter comple-
 227 ment; the total number of visits per pointing and
 228 their distribution on the sky; and total sky coverage.
 229 Additionally, they inform the design of the data pro-
 230 cessing and access systems. By optimizing the system
 231 parameters to support a wide range of scientific goals,
 232 we maximize the observatory’s scientific output across
 233 all areas, making Rubin a powerful discovery machine
 234 capable of addressing a broad range of astrophysical
 235 questions.

236 Throughout the duration of the LSST, Rubin Obser-
 237 vatory will issue a series of Data Releases, each repre-
 238 senting a complete reprocessing of all LSST data col-
 239 lected up to that point. Prior to the start of the LSST
 240 survey, commissioning activities generated a significant
 241 volume of science-grade data. To make this early data
 242 available to the community, the Rubin Early Science
 243 Program (L. P. Guy et al. 2026) was established. One
 244 key component of this program is a series of Data Pre-
 245 views; early versions of the LSST Data Releases. These
 246 previews include preliminary data products derived from
 247 both simulated and commissioning data, which, to-
 248 gether with early versions of the data-access services,
 249 are intended to support high-impact early science, facil-
 250 itate community readiness, and inform the development
 251 of Rubin’s operational capabilities ahead of the start of
 252 full survey operations. All data and services provided
 253 through the Rubin Early Science Program are offered
 254 on a shared-risk basis⁸⁷.

255 This paper describes Rubin’s second of three planned
 256 Data Previews: Data Preview 1 (DP1) (NSF-DOE Vera
 257 C. Rubin Observatory 2025a). The first, Data Preview
 258 0 (DP0), contained data products produced from the
 259 processing of simulated LSST-like datasets. These were
 260 released together with a very early version of the Rubin
 261 Science Platform (RSP) (M. Jurić et al. 2019), which
 262 provided the data-access services. DP0 was released in
 263 multiple phases; DP0.1, DP0.2, and DP0.3, each build-
 264 ing upon the previous and incorporating new data and
 265 functionalities. DP0.1 and DP0.2 use data from the cos-
 266 moDC2 simulations (LSST Dark Energy Science Collab-
 267 oration (LSST DESC) et al. 2021) prepared by the Dark
 268 Energy Science Collaboration (DESC), whereas DP0.3
 269 is based on simulated datasets from the Solar System

270 Science Collaboration. Online documentation for DP0
 271 is available at <https://dp0.lsst.io>.

272 DP1 contains data products derived from the repro-
 273 cessing of science-grade exposures acquired by the Rubin
 274 Commissioning Camera (LSSTComCam) in late 2024.
 275 The third and final Data Preview, Data Preview 2
 276 (DP2), is planned to be based on a reprocessing of all
 277 science-grade data taken with Rubin’s LSSTCam during
 278 commissioning.

279 All Rubin Data Releases and Previews are subject to a
 280 2 yr proprietary period, with immediate access granted
 281 exclusively to LSST data rights holders⁸⁸ (R. Blum &
 282 the Rubin Operations Team 2020). After the 2 yr pro-
 283 prietary period, DP1 will be made public. However,
 284 even once the data become public, access for individuals
 285 without data rights will not be provided through Rubin
 286 Data Access Centers in the US and Chile (R. Blum &
 287 the Rubin Operations Team 2020). Alternative access
 288 mechanisms are still under discussion and have not yet
 289 been finalized.

290 In this paper, we describe the contents and valida-
 291 tion of Rubin DP1, the first Data Preview to deliver
 292 data derived from observations conducted by the Vera
 293 C. Rubin Observatory, as well as the data-access mecha-
 294 nisms and community-support services that accompany
 295 it. DP1 is based on the reprocessing of 1792 science-
 296 grade exposures acquired during the first on-sky com-
 297 missioning campaign, conducted over 48 nights between
 298 2024-10-24 and 2024-12-11. It covers a total area of
 299 approximately ~ 15 deg² distributed across seven dis-
 300 tinct noncontiguous fields. The data products include
 301 raw and calibrated single-epoch images, coadded images,
 302 difference images, detection catalogs, and other derived
 303 data products. DP1 is about 3.5 TB in size and con-
 304 tains around 2.3 million distinct astronomical objects,
 305 detected in 2644 coadded images. Full DP1 release doc-
 306 umentation is available at <https://dp1.lsst.io>. Despite
 307 Rubin Observatory still being in commissioning and not
 308 yet complete at the time the observations were acquired,
 309 Rubin DP1 provides an important first look at the data,
 310 showcasing its characteristics and capabilities.

311 The structure of this paper is as follows. In section
 312 2 we describe the observatory system and overall con-
 313 struction and commissioning status at the time of data
 314 acquisition, the seven fields included in DP1, and the
 315 observing strategy used. Section 3 summarizes the con-
 316 tents of DP1 and the data products contained in the
 317 release. The data processing pipelines are described in

⁸⁷ Shared risk means early access with caveats: the community benefits from getting a head start on science, preparing analyses, and providing feedback, while also accepting that the system may not work as well as it will during full operations.

⁸⁸ Individuals or institutions with formal authorization to access proprietary data collected by the Vera C. Rubin Observatory. See <https://www.lsst.org/scientists/international-drh-list>

section 4, followed by a description of the data validation and performance assessment in section 5. Section 6 describes the *RSP*, a cloud-based data science infrastructure that provides tools and services to Rubin data rights holders to access, visualize and analyze peta-scale data generated by the *LSST*. Section 7 presents Rubin Observatory’s model for community support, which emphasizes self-help via documentation and tutorials, and employs an open platform for issue reporting that enables crowd-sourced solutions. Finally, a summary of the *DP1* release and information on expected future releases of data is given in section 8. The appendix contains a useful glossary of terms used throughout this paper.

All magnitudes quoted are in the AB system (J. B. Oke & J. E. Gunn 1983), unless otherwise specified.

2. ON-SKY COMMISSIONING CAMPAIGN

The primary objective of the first Rubin on-sky commissioning campaign was to optically align the Simonyi Survey Telescope and verify its ability to deliver acceptable image quality using *LSSTComCam*. Additionally, the campaign provided valuable operational experience to support commissioning *LSSTCam* (T. Lange et al. 2024; A. Roodman et al. 2024). We note that commissioning *LSSTComCam* was not an objective of the campaign; rather *LSSTComCam* was used as a tool to support broader observatory commissioning, including early testing of the *Active Optics System* (AOS) (§2.1) and the *LSST Science Pipelines* (§2.4). As a result, many artifacts present in the data are specific to *LSSTComCam* and will be addressed only if they persist with *LSSTCam*. Accordingly, the image quality achieved during this campaign, and in the *DP1* data, may not reflect the performance ultimately expected from *LSSTCam*.

Approximately 16,000 exposures were collected during this campaign, the majority in support of AOS commissioning, system-level verification, and end-to-end testing of the telescope’s hardware and software. This included over 10,000 exposures for AOS commissioning, more than 2000 bias and dark calibration frames, and over 2000 exposures dedicated to commissioning the *LSST Science Pipelines*. For *DP1*, we have selected a subset of 1792 science-grade exposures from this campaign that are most useful for the community to begin preparing for early science.

At the time of the campaign, the observatory was still under construction, with several key components, such as dome thermal control, full mirror control, and the final AOS configuration either incomplete or still undergoing commissioning. As a result, image quality varied widely throughout the campaign and exhib-

ited a broader distribution than is expected with *LSSTCam*. Despite these limitations, the campaign successfully demonstrated system integration and established a functional observatory.

2.1. Simonyi Survey Telescope

The Simonyi Survey Telescope (B. Stalder et al. 2024) features a unique three-mirror design, including an 8.4-meter *Primary Mirror Tertiary Mirror* (M1M3) fabricated from a single substrate and a 3.5 m *Secondary Mirror* (M2). This compact configuration supports a wide 3.°5 field of view while enabling exceptional stability, allowing the telescope to slew and settle in under 5 s. To achieve the scientific goals of the 10-yr *LSST*, the Observatory must maintain high image quality across its wide field of view (Ž. Ivezić et al. 2019b). This is accomplished through the AOS (B. Xin et al. 2015; G. Megias Homar et al. 2024a), which corrects, between successive exposures, wave front distortions caused by optical misalignments and mirror surface deformations, primarily due to the effect of gravitational and thermal loads.

The AOS, which comprises an open-loop component and a closed-loop component, optimizes image quality by aligning the camera and M2 relative to M1M3, as well as adjusting the shapes of all three mirrors to nanometer precision. The AOS open-loop component corrects for predictable distortions and misalignments, while the closed-loop component addresses unpredictable or slowly varying aberrations using feedback from the corner wave front sensors. The closed-loop wave front sensing technique is curvature wave front sensing, which infers wave front errors in the optical system by analyzing extra- and intrafocal star images (S. Thomas et al. 2023). Since *LSSTComCam* lacks dedicated wave front sensors, wave front errors were instead estimated by defocusing the telescope ± 1.5 mm on either side of focus and applying the curvature wave front sensing pipeline to the resulting images. Each night began with an initial alignment correction using a laser tracker to position the system within the capture range of the closed-loop algorithm (G. Megias Homar et al. 2024b). Once this coarse alignment was complete, the AOS refined the optical alignment and applied mirror surfaces corrections to optimize the image quality across the *LSSTComCam* field of view.

During *LSST Science Pipelines* commissioning (§2.4), observations were conducted using the AOS in open-loop mode only, without closed-loop corrections between exposures. Closed-loop operation, which requires additional intra- and extrafocal images with *LSSTComCam*, was not compatible with the continuous data ac-

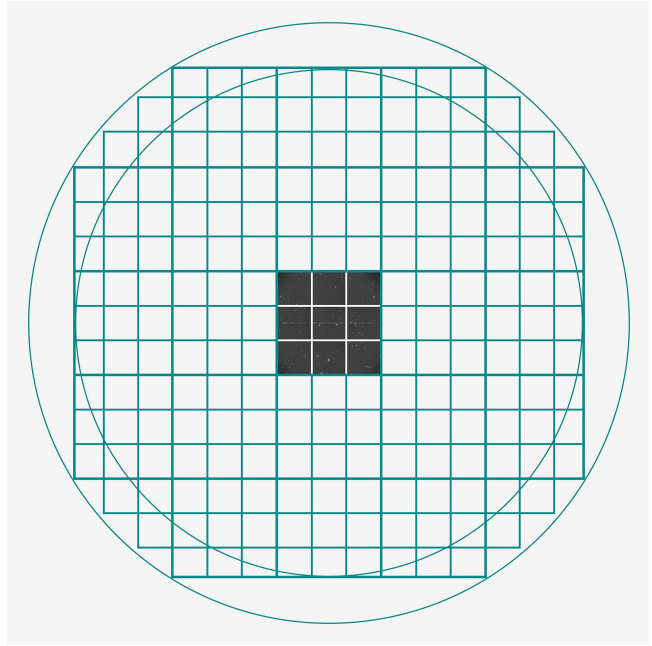
420 quisation needed by the pipelines. The image quality
 421 for these data was monitored by measuring the [Point](#)
 422 [Spread Function \(PSF\)](#) at [Full Width at Half-Maximum](#)
 423 [\(FWHM\)](#), and closed-loop sequences were periodically
 424 run when image quality degradation was observed.

425 2.2. *LSSTComCam*

426 [LSSTComCam](#) ([B. Stalder et al. 2022, 2020](#); [J.](#)
 427 [Howard et al. 2018](#); [SLAC National Accelerator Laboratory & NSF-DOE Vera C. Rubin Observatory 2024](#)) is
 428 a 144-megapixel version of the 3.2-gigapixel [LSSTCam](#).
 429 It covers approximately 5% of the [LSSTCam](#) focal plane
 430 area, with a field of view of $\sim 0.5 \text{ deg}^2$ ($40' \times 40'$), com-
 431 pared to [LSSTCam](#)'s 9.6 deg^2 . It was developed to val-
 432 idate camera interfaces with other observatory compo-
 433 nents and evaluate overall system performance prior to
 434 the start of [LSSTCam](#) commissioning. Although [LSST-](#)
 435 [ComCam](#) has a smaller imaging area, it shares the same
 436 plate scale of $0''.2 \text{ pixel}^{-1}$ and is housed in a support
 437 structure that replicates the mass, center of gravity, and
 438 physical dimensions of [LSSTCam](#). All mechanical and
 439 utility interfaces to the telescope are implemented iden-
 440 tically, enabling full end-to-end testing of observatory
 441 systems, including readout electronics, image acquisition,
 442 and data pipelines. Although the [LSSTComCam](#)
 443 cryostat employs a different cooling system (Cryotels) to
 444 that of [LSSTCam](#), it included a refrigeration pathfinder
 445 to validate the cryogenic system intended for [LSSTCam](#).

446 The [LSSTCam](#) focal plane comprises 25 modular rafts
 447 arranged in a 5×5 grid, of which 21 are science rafts ded-
 448 icated to imaging and four are corner rafts used for guid-
 449 ing and wave front sensing. [LSSTCam](#) employs CCD
 450 sensors from two vendors: [Imaging Technology Laboratory, University of Arizona \(UA\)](#) (ITL) and [Teledyne](#)
 451 [\(E2V\)](#). In contrast, [LSSTComCam](#) contains only a single
 452 science raft equipped exclusively with ITL sensors.
 453 [Figure 1](#) presents a schematic of the [LSSTCam](#) focal
 454 plane, with the [LSSTComCam](#) raft positioned at the
 455 center, corresponding to the [LSSTCam](#) central science
 456 raft location. The perspective is from above, looking
 457 down through the [LSSTComCam](#) lenses onto the focal
 458 plane.
 459

460 Each science raft is a self-contained unit compris-
 461 ing nine $4\text{K} \times 4\text{K}$ [Charge-Coupled Device \(CCD\)](#) ([G. E.](#)
 462 [Smith 2010](#)) sensors arranged in a 3×3 mosaic, complete
 463 with integrated readout electronics and cooling systems.
 464 Each sensor is subdivided into 16 segments arranged in
 465 a 2×8 layout, with each segment consisting of 512×2048
 466 pixels and read out in parallel using individual ampli-
 467 fiers. This design is identical across all science rafts.
 468 To maintain uniform performance and [calibration](#), each
 469
 470



471 **Figure 1.** [LSSTComCam](#) focal plane layout illustrating the
 472 placement of its nine sensors, shown in gray, which form a
 473 raft. The view is looking down from above the focal plane
 474 through the [LSSTComCam](#) lenses. [LSSTComCam](#) is Raft
 475 22 (R22). We also indicate the location of the [LSSTCam](#)
 476 sensors (open squares) to highlight the field of view of [LSST-](#)
 477 [ComCam](#) in relation to that of [LSSTCam](#).

478 raft is populated exclusively with sensors from a single
 479 vendor.

480 [LSSTComCam](#) consists of a single science raft, desig-
 481 nated Raft 22 (R22), equipped solely with ITL sensors.
 482 These sensors were selected from the best-performing re-
 483 maining ITL devices after the [LSSTCam](#) rafts were fully
 484 populated. Some exhibit known issues such as high read-
 485 out noise (e.g., Detector 8) and elevated [Charge Transfer](#)
 486 [Inefficiency \(CTI\)](#) (e.g., Detector 5). Consequently, cer-
 487 tain image artifacts present in the DP1 dataset may be
 488 specific to [LSSTComCam](#). [Figure 2](#) shows the [LSST-](#)
 489 [ComCam](#) R22 focal plane layout and the placement and
 490 numbering scheme of sensors (“S”) and amplifiers (“C”).
 491 This configuration is identical across all science rafts
 492 in [LSSTCam](#). The [LSSTCam](#) and [LSSTComCam](#) focal
 493 planes are described in detail in ([A. A. Plazas Malagón](#)
 494 [et al. 2026](#)).

495 2.2.1. *Filter Complement*

496 [LSSTComCam](#) supports imaging with six broadband
 497 filters *ugrizy* spanning 320–1050 nm, identical in design
 498 to [LSSTCam](#). However, its filter exchanger can hold
 499 only three filters at a time, compared to five with [LSST-](#)
 500 [Cam](#). The full-system throughput of the six [LSSTCom-](#)
 501 [Cam](#) filters, which encompasses contributions from a

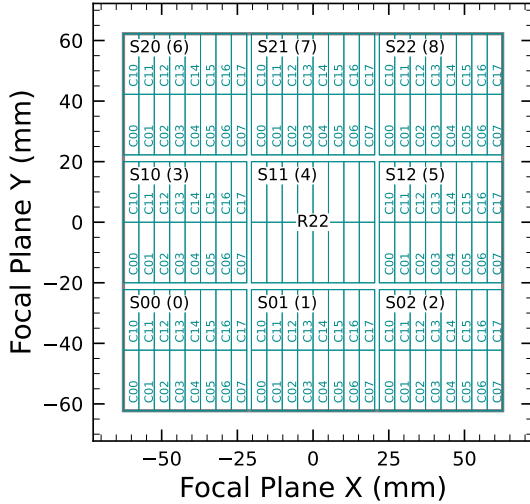


Figure 2. LSSTComCam focal plane layout, showing R22 and the placement and numbering scheme of sensors (“S”) and amplifiers (“C”). The view is from above, looking through the LSSTComCam lenses onto the focal plane. Each sensor contains 16 amplifiers, and the raft is composed of a 3×3 array of sensors. The detector number for each sensor is indicated in parentheses.

496 standard atmosphere at an airmass of 1.2, telescope opt-
 497 ics, camera surfaces, and the mean ITL detector quan-
 498 tum efficiency is shown in Figure 3. The corresponding
 499 transmission curves are provided as a DP1 data product
 500 (§3.6.1).

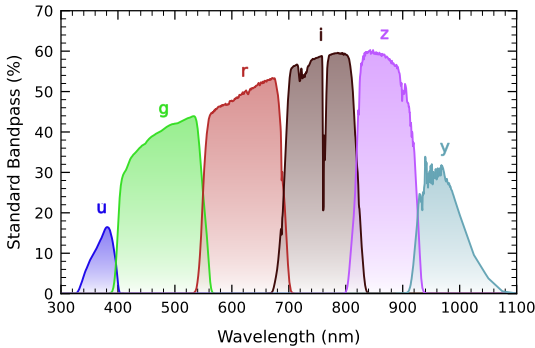


Figure 3. LSSTComCam standard bandpasses, illustrating full-system throughput. The bandpasses include a standard atmosphere at an airmass of 1.2, telescope optics, camera surfaces, and mean ITL detector quantum efficiency. The corresponding transmission curves are provided as a DP1 data product.

2.2.2. Timing Calibration

504 The absolute time accuracy of data taken with LSST-
 505 ComCam relies on the Network Time Protocol (NTP)
 506 for clock synchronization, which should be accurate to

507 approximately 1 ms. In order to evaluate the absolute
 508 timing accuracy of the entire system we observed the
 509 geosynchronous satellite EUTELSAT 117 West B with a
 510 set of 10 usable 10 s exposures over two nights. EUTEL-
 511 SAT 117 West B is part the Global Positioning System
 512 (GPS) and serves as one of the Wide Area Augmentation
 513 System (WAAS) satellites operated for the U.S. Federal
 514 Aviation Administration (FAA) and used to broadcast
 515 GPS corrections to air traffic.

516 As these satellites are part of the GPS, their positions
 517 are tracked very precisely and a record of their loca-
 518 tions is published after the fact and can be downloaded.
 519 Following a technique previously employed by other sur-
 520 veys, (J. L. Tonry et al. 2018), we observed the satellite
 521 while tracking the sky and then downloaded the data
 522 files with its precise locations from the National Satel-
 523 lite Test Bed website⁸⁹. By comparing the measured
 524 and predicted locations of the start of the satellite track
 525 on the sky, we determined that (relative to the start of
 526 integration time recorded in the Flexible Image Trans-
 527 port System (FITS) headers) our time was accurate to
 528 53.6 ± 11.0 ms.

529 This work continues to be an area of ongoing study,
 530 with the exact timing of when the shutter open com-
 531 mand is issued, and the complete profile of the shutter
 532 movement not yet determined. However the open com-
 533 mand is on average near 29 ms later. Incorporating the
 534 delays into the fit reduces the offset to 24.8 ± 11.0 mil-
 535 liseconds.

536 The full shutter takes approximately 396 ms to com-
 537 pletely open. As the LSSTComCam sensors are centered
 538 in the aperture, the center of the focal plane should be
 539 exposed about half-way through the shutter open proce-
 540 dure, 198 ms after the open command. There are uncer-
 541 tainties on the full motion profile, and the blade direc-
 542 tion motions are currently not known, but the fraction
 543 of the shutter aperture subtended by the focal plane is
 544 52%. This implies that that the shutter will pass any
 545 pixel between 198 ± 103 ms. Subtracting this from the
 546 fitted delay of 24.8 ms and adding the fitted error of 11.0
 547 ms in quadrature, results in a current conservative es-
 548 timate of the delay of -173.2 ± 104.1 ms, consistent with
 549 and smaller than the constraints on the timing offset
 550 determined using astrometric residuals from known as-
 551 teroid associations presented in §5.9.2.

2.3. Flat-field System

552
 553 During the on-sky campaign, key components of the
 554 Rubin calibration system (P. Ingraham et al. 2022),
 555 including the flat-field screen, had not yet been in-

⁸⁹ <https://www.nstb.tc.faa.gov/nstbarchive.html>

556 stalled. As a result, flat-fielding for DP1 relied entirely
 557 on twilight flats. While twilight flats pose challenges
 558 such as nonuniform illumination and star print through,
 559 they were the only available option during LSSTCom-
 560 Cam commissioning and for DP1 processing. To miti-
 561 gate these limitations, dithered, tracked exposures were
 562 taken over a broad range of azimuth and rotator angles
 563 to construct combined flat calibration frames. Exposure
 564 times were dynamically adjusted to reach target signal
 565 levels of between 10,000 and 20,000 electrons. Future
 566 campaigns with LSSTCam will benefit from more stable
 567 and uniform flat-fielding using the Rubin flat-field
 568 system, described in P. Fagrellius & E. S. Rykoff (2025).

569 2.4. LSST Science Pipelines Commissioning

570 Commissioning of the LSST Science Pipelines, (Rubin
 571 Observatory Science Pipelines Developers 2025), began
 572 once the telescope was able to routinely deliver subarc-
 573 second image quality. The goals included testing the
 574 internal astrometric and photometric calibration across
 575 a range of observing conditions, validating the difference
 576 image analysis and prompt processing (K.-T. Lim 2023)
 577 framework, and accumulating over 200 visits per band
 578 to evaluate deep coadded images with integrated expo-
 579 sure times roughly equivalent to those of the planned
 580 LSST Wide-Fast-Deep (WFD) 10-yr depth. To support
 581 these goals, seven target fields were selected that span
 582 a range of stellar densities, overlap with external refer-
 583 ence datasets, and collectively span the full breadth
 584 of the four primary LSST science themes. These seven
 585 fields form the basis of the DP1 dataset. Figure 4 shows
 586 the locations of these seven fields on the sky, overlaid
 587 on the LSST baseline survey footprint (R. L. Jones et al.
 588 2021; P. Yoachim 2022; Rubin’s Survey Cadence Opti-
 589 mization Committee et al. 2022, 2023, 2025), along with
 590 the sky coverage of both the LSSTCam and LSSTCom-
 592 Cam focal planes. Each of the seven target fields was
 593 observed repeatedly in multiple bands over many nights.
 594 A typical observing epoch on a given target field con-
 595 sisted of 5-20 visits in each of the three loaded filters.
 596 Only images taken as 1×30 second exposures have been
 597 included in DP1. All images were acquired using the
 598 Rubin Feature-Based Scheduler (FBS), version 3.0 (E.
 599 Naghib et al. 2019; P. Yoachim et al. 2024). Table 1 lists
 600 the seven DP1 fields and their pointing centers, and pro-
 601 vides a summary of the band coverage in each.

602 Figure 5 shows the temporal sampling of observations
 603 by filter and by night. The figure indicates the dates
 604 on which each field was observed in a given band but
 605 does not convey the total number of observations ob-
 606 tained per filter on any individual night. Gaps in cov-
 608 erage across some bands arise from the fact that LSST-

609 ComCam can only accommodate three filters at a time
 610 (see §2.2). As the campaign progressed, the temporal
 611 sampling became denser across all fields, reflecting im-
 612 proved efficiency and increased time allocated for science
 613 observations. The Extended Chandra Deep Field-South
 614 Survey (ECDFS) field received the most consistent and
 615 densest temporal sampling. It is important to note that
 616 the time sampling in the DP1 dataset differs signifi-
 617 cantly from what will be seen in the final LSST data. All
 618 fields except for the low ecliptic latitude field, Rubin_
 619 SV_38_7, used a small random dithering pattern. The
 620 random translational dithers of the telescope boresight
 621 were applied for each visit, with offsets of up to $0^\circ 2$
 622 around the pointing center. The rotational dithers of
 623 the camera rotator were typically approximately 1° per
 624 visit, with larger random offsets at each filter change,
 625 which worked to keep operational efficiency high. The
 626 Rubin_SV_38_7 field used a different dither pattern to
 627 optimize coverage of solar system objects and test solar
 628 system object linking across multiple nights. These ob-
 629 servations used a 2×2 grid of LSSTComCam pointings
 630 to cover an area of about $1^\circ 3 \times 1^\circ 3$. The visits cycled
 631 between the grid’s four pointing centers, each separated
 632 by $0^\circ 65$ degrees, and used small random translational
 633 dithers to fill chip gaps with the goal of acquiring 3-
 634 4 visits per pointing center per band in each observing
 635 epoch. The R.A. and Decl values provided in Table 1
 636 for this field represent approximately the centers of the
 637 four fields.

638 Figure 6 shows sky coverage maps showing the distri-
 639 bution of visits in each of the seven DP1 fields, color
 640 coded by band. The images clearly show the focal plane
 641 chip gaps and dithering pattern. Only the detectors for
 642 which single-frame processing succeeded are included in
 643 the plots, which explains why the central region of 47_
 644 Tuc looks thinner than the other fields (see §5.10). Ta-
 646 ble 2 reports the 5σ point-source depths for coadded im-
 647 ages per field and per band, where coverage in a band is
 648 nonzero, together with the expected 10 yr LSST depths
 649 derived from the baseline simulated survey (F. B. Bianco
 650 et al. 2022).

651 2.5. Delivered Image Quality

652 The delivered image quality is influenced by contribu-
 653 tions from both the observing system (i.e., dome, tele-
 654 scope and camera) and the atmosphere. During the
 655 campaign, the Rubin Differential Image Motion Moni-
 656 tor (DIMM) was not operational, so atmospheric seeing
 657 was estimated using live data from the Southern Astro-
 658 physical Research Telescope (SOAR) Ring-Image Next
 659 Generation Scintillation Sensor (RINGSS) seeing moni-
 660 tor, also located on Cerro Pachón. Although accelerom-

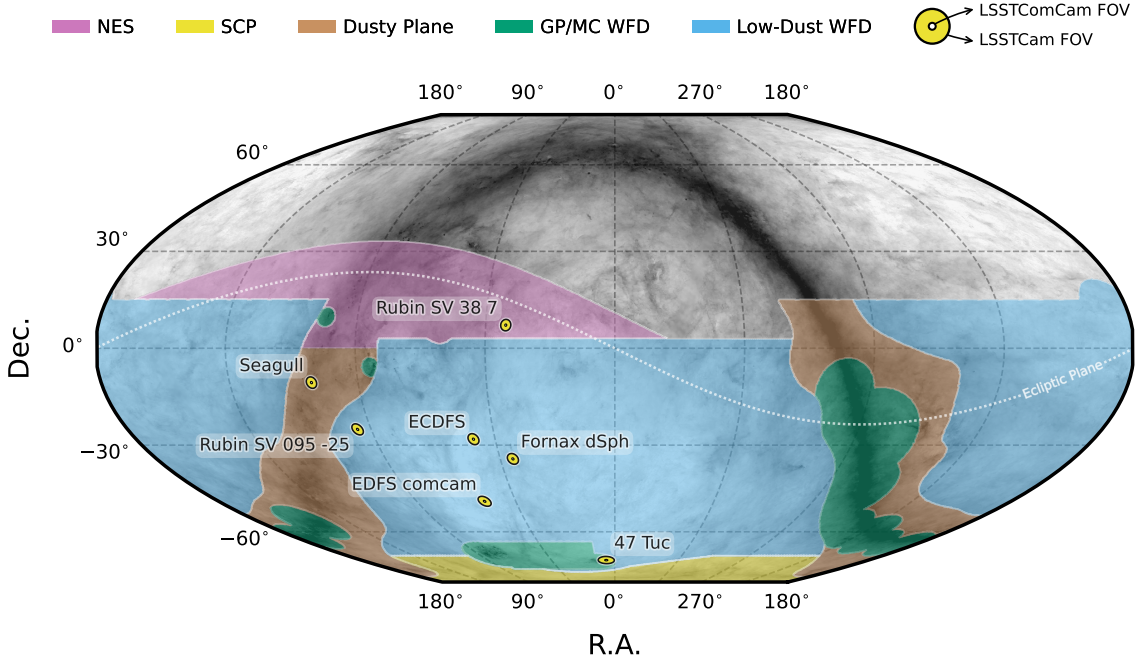


Figure 4. Locations of the seven DP1 fields overlaid on the LSST baseline survey footprint. Shown are the north ecliptic spur (NES); south celestial pole (SCP); low-dust WFD: regions away from the Galactic plane (GP) observed with a WFD cadence; and GP and Magellanic Clouds (MCs) regions observed with a WFD cadence. The fields of view of the LSSTCam and LSSTComCam focal planes are shown as concentric yellow circles about the pointing center of each field. The background Milky Way dust map is based on the model of Finkbeiner, Davis, and Schlegel (hereafter FDS model)(D. P. Finkbeiner et al. 1999).

Table 1. DP1 fields and pointing centers with the number of exposures in each band per field. International Celestial Reference System coordinates are in units of decimal degrees, and are specified as J2000.

Field Code	Field Name	R.A. (deg)	Decl (deg)	Band						Total
				<i>u</i>	<i>g</i>	<i>r</i>	<i>i</i>	<i>z</i>	<i>y</i>	
47_Tuc	47 Tucanae Globular Cluster	6.128	-72.090	6	10	32	19	0	5	72
ECDFS	Extended Chandra Deep Field South	53.160	-28.100	43	230	237	162	153	30	855
EDFS_comcam	Rubin SV Euclid Deep Field South	59.150	-48.730	20	61	87	42	42	20	272
Fornax_dSph	Fornax Dwarf Spheroidal Galaxy	40.080	-34.450	0	5	25	12	0	0	42
Rubin_SV_095_-25	Rubin SV Low Galactic Latitude Field	95.040	-25.000	33	82	84	23	60	10	292
Rubin_SV_38_7	Rubin SV Low Ecliptic Latitude Field	37.980	7.015	0	44	40	55	20	0	159
Seagull	Seagull Nebula	106.300	-10.510	10	37	43	0	10	0	100
Total				112	469	548	313	285	65	1792

661 eters mounted on the mirror cell and top-end assembly
 662 were available to track dynamic optics effects, such as
 663 mirror oscillations that can degrade optical alignment,
 664 these data were not used during the campaign. Mount
 665 encoder data were used to measure the mount jitter in
 666 every image, with a measured median contribution of
 667 0^h.004 to image degradation. As the pointing model
 668 was not fine-tuned, tracking errors could range from 0^h.2

669 to 0^h.4 per image, depending on R.A. and decl.. Dome
 670 and mirror-induced seeing were not measured during the
 671 campaign.

672 The DP1 median delivered image quality, quantified
 673 as the PSF at FWHM across all filters and target fields,
 674 is 1^h.14. The best images achieve a PSF FWHM of ap-
 675 proximately 0^h.58. Both the per-sensor PSF FWHM and
 676 the overall median vary depending on the filter and the

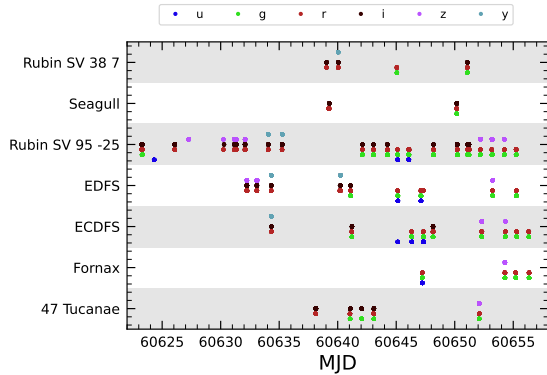


Figure 5. Temporal distribution of DP1 observations, grouped by field as a function of Modified Julian Date (MJD) and color coded by filter. Each point indicates that a given field was observed at least once in the corresponding filter on that date.

Table 2. DP1 median 5σ coadded point-source detection limits per field and band, expressed in magnitudes, compared with the expected 10 yr LSST values derived from the baseline simulated survey (F. B. Bianco et al. 2022).

Field Code	Band					
	<i>u</i>	<i>g</i>	<i>r</i>	<i>i</i>	<i>z</i>	<i>y</i>
47_Tuc	-	24.03	24.24	23.90	-	21.79
ECDFS	24.55	26.18	25.96	25.71	25.07	23.10
EDFS_comcam	23.42	25.77	25.72	25.17	24.47	23.14
Fornax_dSph	-	24.53	25.07	24.64	-	-
Rubin_SV_095_-25	24.29	25.46	24.95	24.86	24.32	22.68
Rubin_SV_38_7	-	25.46	25.15	24.86	23.52	-
Seagull	23.51	24.72	24.19	-	23.30	-
LSST 10 yr	25.73	26.86	26.88	26.34	25.63	24.87

Table 3. DP1 Median image quality per field and per band quantified as the Point-spread Function at FWHM.

Field Code	Band						All
	<i>u</i>	<i>g</i>	<i>r</i>	<i>i</i>	<i>z</i>	<i>y</i>	
47_Tuc	-	1.27	1.25	1.11	-	1.33	1.22
ECDFS	1.40	1.14	1.08	1.00	1.00	1.07	1.08
EDFS_comcam	1.88	1.25	1.20	1.10	1.18	0.99	1.19
Fornax_dSph	-	1.16	0.82	0.93	-	-	0.85
Rubin_SV_095_-25	1.40	1.25	1.14	0.97	1.17	0.82	1.19
Rubin_SV_38_7	-	1.13	1.13	1.10	1.22	-	1.13
Seagull	1.50	1.34	1.19	-	1.19	-	1.25
All	1.48	1.17	1.12	1.03	1.11	1.01	1.13

677 specific target field. The median delivered image quality
 678 per band and target field is provided in Table 3.
 679 Figure 7 shows the distribution of PSF FWHM (in arc-
 680 seconds) over all 16,071 individual sensors images. On-
 682 going efforts aim to quantify all sources of image degra-
 683 dation, including contributions from the camera system;
 684 static and dynamic optical components; telescope mount
 685 motion; observatory-induced seeing from the dome and
 686 primary mirror; and atmospheric conditions. For the
 687 LSST, the design specification for the median delivered
 688 image quality, referenced to the zenith and 550nm, is
 689 $0''.7$. This value corresponds to the measured median at-
 690 mospheric seeing at the Cerro Pachón site and a system
 691 contribution to delivered image quality of $0''.35$ added in
 692 quadrature.

693 3. OVERVIEW OF THE CONTENTS OF RUBIN 694 DP1

695 In this section we describe the Rubin DP1 data prod-
 696 ucts and provide summary statistics for each. For
 697 more detailed information, we refer the reader to the
 698 DOI-registered DP1 release documentation available at
 699 <https://dp1.lsst.io> and the catalog schema available at
 700 <https://sdm-schemas.lsst.io>.⁹⁰

701 The DP1 science data products are derived from the
 702 15,972 individual CCD images taken across 1792 expo-
 703 sures in the seven LSSTComCam commissioning fields
 704 (§2.4). To aid legibility, we have separated the descrip-
 705 tions of the data products from the description of the
 706 Data Release Processing pipeline (§4). Similarly, as the
 707 DP1 data products can be accessed via one or both of
 708 International Virtual Observatory Alliance (IVOA) Ser-
 709 vices (§6.2.1) or the Data Butler (§6.2.2), we describe
 710 them here in a manner that is agnostic to the means of
 711 access.

712 The data products that comprise DP1 provide an
 713 early preview of future LSST Data Releases and are
 714 strongly dependent on the type and quality of the data
 715 that was collected during the LSSTComCam on-sky
 716 campaign (§2.4). Consequently not all anticipated LSST
 717 data products, as described in the Data Product Defi-
 718 nition Document (DPDD) (M. Jurić et al. 2023), were
 719 produced for the DP1 dataset.

720 Rubin Observatory has adopted the convention
 721 by which single-epoch detections are referred to as
 722 “sources”, and the astrophysical object associated with

⁹⁰ Searchable catalog schema are also available to Data Rights Holders via the Rubin Science Platform at <https://data.lsst.cloud>.

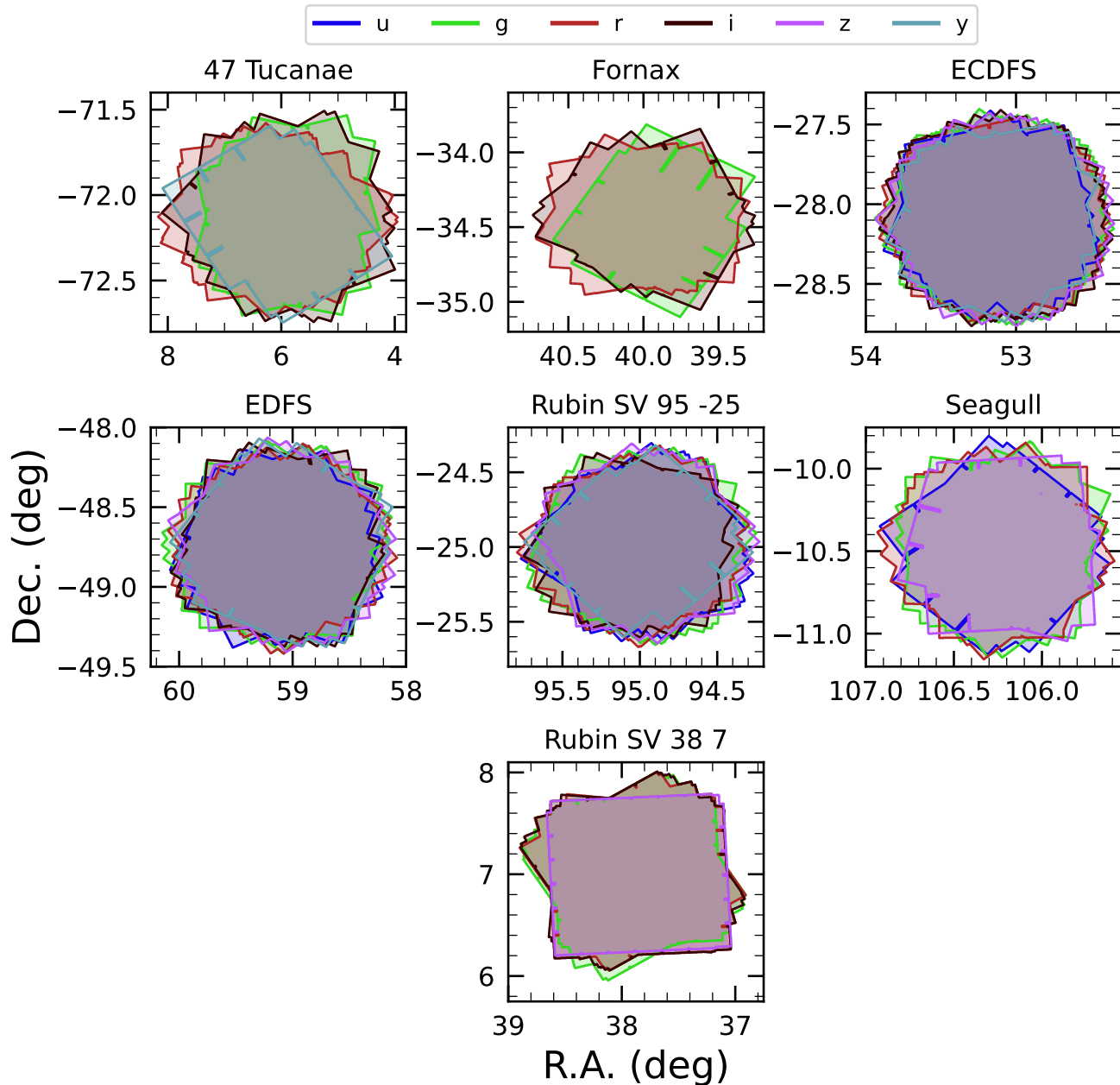


Figure 6. Sky coverage maps showing the distribution of visits in each field, color coded by band. The images clearly show the focal plane chip gaps and dithering pattern. Only the detectors for which single-frame processing succeeded are included in the plots, which explains why the central region of 47_Tuc looks thinner than the other fields.

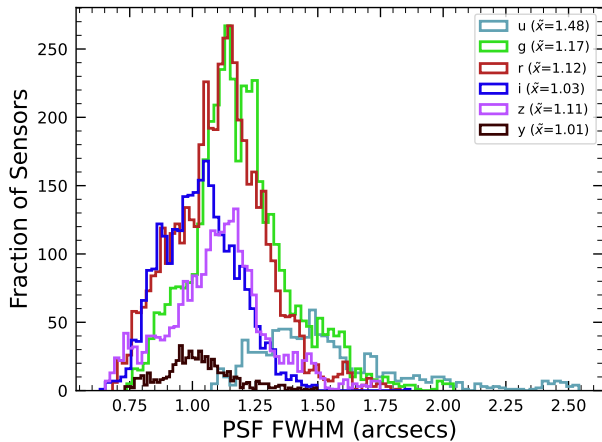
723 a given detection is referred to as an “object”⁹¹. As 728
 724 such, a given object will likely have multiple associated 729
 725 sources, since it will be observed in multiple epochs. 730

726 At the highest level, the DP1 data products fall into
 727 one of five types:

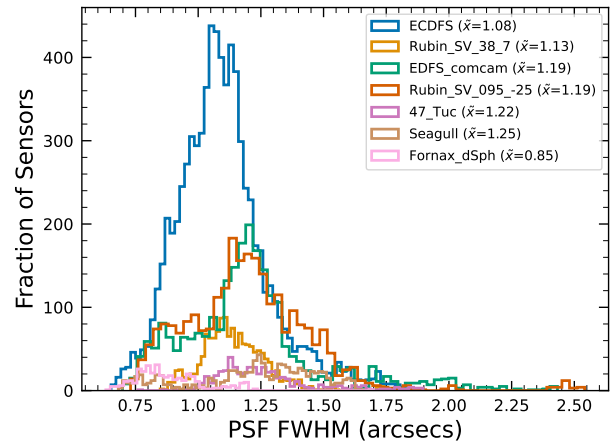
- **Science Images.** Including single-epoch images, deep and template coadded images, and difference images (§3.1).

- **Catalogs.** Catalogs of astrophysical sources and objects detected and measured in the aforementioned images. We also provide the astrometric and photometric reference catalog generated from

⁹¹ We caution that this nomenclature is not universal; for example, some surveys use “detections” for what we call “sources”, and “sources” for what we call “objects”.



(a) PSF FWHM (arcsecs) per passband across all DP1 target fields.



(b) PSF FWHM (arcsecs) per DP1 target field across all passbands

Figure 7. Histograms showing the distribution of delivered image quality for all 16,071 single-epoch individual sensors in the DP1 dataset per passband (a) and per field (b). The median values are given in the legend.

external sources that was used during processing to generate the DP1 data products (§3.2).

- **Maps.** Maps provide non-science-level visualizations of the data within the release. They include, for example, zoomable multiband images and coverage maps (§3.4.1).
- **Ancillary data products.** Including for example, the parameters used to configure the data processing pipelines, log and processing performance files, and calibration data products (§3.6).
- **Metadata.** Given in the form of tables containing information about each visit and processed image, such as pointing, exposure time, and a range of image quality summary statistics (§3.5).

While images and catalogs are expected to be the primary data products for scientific research, we also recognize the value of providing access to other data types to support investigations and ensure transparency.

To facilitate processing, Rubin DP1 uses a single sky map⁹² that covers the entire sky area encompassing the seven DP1 fields. The DP1 sky map divides the entire celestial sphere into 18938 tracts, each covering approximately 2.8 deg². The tracts are arranged in rings of decl., ordered from south to north, then with increasing R.A. within a ring. Each tract is further subdivided into 10 × 10 equally-sized patches. Both tracts and patches

overlap with their neighboring regions. The amount of overlap between tracts changes with declination, with tracts nearest the poles having the greatest degree of overlap; the minimum overlap between tracts is 1′0. By contrast, the amount of overlap between patches is constant, with each patch overlapping each of its neighboring patches by 80′0. Each patch covers 0036 deg² which, due to the patch overlap, is slightly larger than the tract area divided by the number of patches in a tract. The aerial coverage of a patch is comparable to, but somewhat smaller than, the 0.058 deg² field of view of a single LSSTComCam or LSSTCam detector, meaning each detector image spans multiple patches. The size of a tract is larger than the LSSTComCam field of view. However, since each observed field extends across more than one tract, each field covers multiple tracts.

The sky map is integral to the production of coadded images. To create a coadded image, the processing pipeline selects all calibrated science images in a given field that meet specific quality thresholds (§3.1 and §4.5.1) for a given patch, warps them onto a single consistent pixel grid for that patch, as defined by the sky map, then coadds them. Each individual coadd image therefore covers a single patch.

Throughout this section, the data product names are indicated using monospace font. Data products are accessed via either the IVOA Services (§6.2.1) or the Data Butler (§6.2.2).

3.1. Science Images

Science images are exposures of the night sky, as distinct from calibration images (§3.6.3). Although the release includes calibration images, thereby allowing users to reprocess the raw images if needed, this is expected

⁹² A sky map is a tiling of the celestial sphere, organizing large-scale sky coverage into manageable sections for processing and analysis. While the sky map described here is specific to DP1, we do not anticipate major changes to the sky map in future Data Releases.

Table 4. Number of Raw images per field and band. Each raw image corresponds to a single 30 s LSSTComCam exposure on one CCD. Most exposures produce nine raw images, one per sensor in the focal plane, however some yield fewer due to occasional hardware or readout issues.

Field Code	Band						Total
	<i>u</i>	<i>g</i>	<i>r</i>	<i>i</i>	<i>z</i>	<i>y</i>	
47_Tuc	54	90	288	171	0	45	648
ECDFS	387	2070	2133	1455	1377	270	7692
EDFS_comcam	180	549	783	378	378	180	2448
Fornax_dSph	0	45	225	108	0	0	378
Rubin_SV_095_-25	297	738	756	207	540	90	2628
Rubin_SV_38_7	0	396	360	495	180	0	1431
Seagull	90	333	387	0	90	0	900
Total	1008	4221	4932	2814	2565	585	16125

to be necessary only in rare cases. Users are strongly encouraged to start from the `visit_image` provided. The data product names shown here are those used by the Data Butler, but the names used in the IVOA Services differ only slightly in that they are prepended by “lsst”.

3.1.1. Raw Image

Raw images (NSF-DOE Vera C. Rubin Observatory 2025b) are unprocessed data received directly from the camera. Each `raw` corresponds to a single CCD from a single LSSTComCam exposure of 30 s duration. Each LSSTComCam exposure typically produces up to nine raw images, one per sensor in the focal plane. However, a small number of exposures resulted in fewer than nine raw images due to temporary hardware issues or readout faults.

In total, DP1 includes 16,125 raw images. Table 4 provides a summary by target and band. A `raw` contains 4608×4096 pixels, including prescan and overscan, and occupies around 18 MB of disk space.⁹³ The field of view of a single `raw` image, excluding prescan and overscan regions, is roughly $0^\circ.23 \times 0^\circ.22 \approx 0.051 \text{ deg}^2$, corresponding to a plate scale of $0''.2 \text{ pixel}^{-1}$.

3.1.2. Visit_images

`Visit_images` (NSF-DOE Vera C. Rubin Observatory 2025c) are fully calibrated processed images. They have undergone instrument signature removal (§4.2.1)

⁹³ Each amplifier image contains 3 and 64 columns of serial prescan and overscan pixels, respectively, and 48 rows of parallel overscan pixels, meaning a `raw` contains 4072×4000 exposed pixels.

and all the single-frame processing steps described in §4.2 which are, in summary, PSF modeling, background subtraction, and astrometric and photometric calibration. As with `raw` images, a `visit_image` contains processed data from a single CCD resulting from a single 30 s LSSTComCam exposure. As a consequence, a single LSSTComCam exposure typically results in nine `visit_images`. The handful of exposures with fewer than nine `raw` images also have fewer than nine `visit_images`, but there are an additional 153 `raw` images that failed processing and for which there is thus no corresponding `visit_image`. The majority of failures – 131 in total – were due to challenges with astrometric fits or PSF models in the 47_Tuc crowded field. The other failures were in the Rubin_SV_095_-25 (nine failures), ECDFS (eight), Fornax_dSph (three), and EDFS_comcam (two) fields.

In total, there are 15,972 `visit_images` in DP1. Each `visit_image` comprises three images: a calibrated science image, a variance image, and a pixel-level bit mask that flags issues such as saturation, cosmic rays, or other artifacts. Each `visit_image` also contains a position-dependent PSF model, World Coordinate System (WCS) information, and various metadata providing information about the observation and processing. The science and variance images and the pixel mask each contain 4072×4000 pixels. In total, a single `visit_image`, including all extensions and metadata, occupies around 110 MB of disk space. A plot showing the normalized cumulative histogram of the 5σ depths of all the `visit_images` in DP1 is shown in Figure 8.

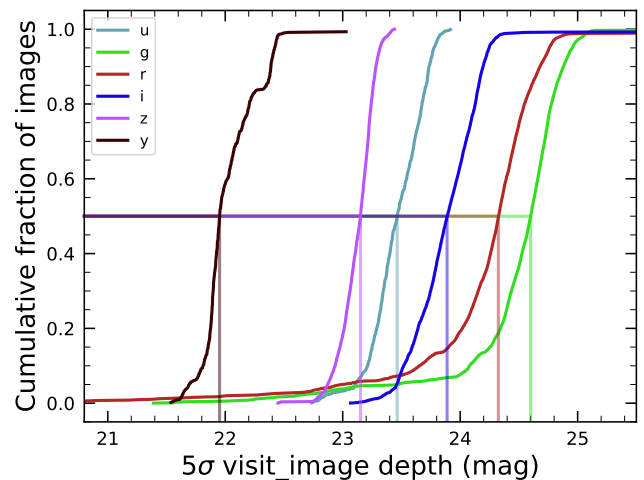


Figure 8. Normalized cumulative histograms of the 5σ depths of all `visit_images` in each band. The vertical lines indicate the 50th percentiles for each band (see legend).

3.1.3. *Deep_coadds*

Deep_coadd images (NSF-DOE Vera C. Rubin Observatory 2025d) are created on a per-band basis, meaning only data from exposures taken with a common filter are coadded. As such, there are up to six deep_coadds covering each patch – one for each of the six LSSTComCam bands. The process of producing deep_coadds is described in §4.5 but, to summarize, it involves the selection of suitable visit_images (both in terms of patch coverage, band, and image quality), the warping of those visit_images onto a common pixel grid, and the coadding of the warped visit_images. To be included in a DP1 deep_coadd, a visit_image needed to have a PSF FWHM smaller than 1"7. Of the 15,972 visit_images, 15,375 satisfied this criterion and were therefore used to create deep_coadd images.

There are a total of 2644 deep_coadd images in DP1. As mentioned above, a single deep_coadd covers one patch, and includes a small amount of overlap with its neighboring patch. The sky map used for DP1 defines a patch as having an on-sky area of 0.028 deg² excluding overlap, and 0.036 deg² including overlap. A single deep_coadd – including overlap – contains 3400 × 3400 equal-sized pixels, corresponding to a platescale of 0"2 pixel⁻¹. Each deep_coadd contains the science image (i.e., the coadd), a variance image, and a pixel mask; all three contain the same number of pixels. Each deep_coadd also contains a position-dependent PSF model (which is the weighted sum of the PSF models of the input visit_images), WCS information, plus various metadata.

The number of visit_images that contributed to a given deep_coadd varies across the patch; the Survey Property maps can be consulted to gain insights into the total exposure time at all locations covered by the survey. Similarly, since coadds always cover an entire patch, it is common for a deep_coadd to contain regions that were not covered by any of the selected visit_images, particularly if the patch is on the outskirts of a field and was thus not fully observed. By the nature of how coadds are produced, such regions may contain seemingly valid flux values (i.e., not necessarily zeros or NaNs), but will instead be flagged with the NO_DATA flag in the pixel mask. It is therefore crucial that the pixel mask be referred to when analyzing deep_coadds.

3.1.4. *Template_coadds*

template_coadd images (NSF-DOE Vera C. Rubin Observatory 2025e) are those created to use as templates for difference imaging, i.e., the process of subtracting a template image from a visit_image to identify either variable or transient objects. It should be

noted, however, that template_coadds are not themselves subtracted from visit_images but are, instead, warped to match the WCS of a visit_image. It is this warped template that is subtracted from the visit_image to create a difference image.⁹⁴ As with deep_coadds, template_coadds are produced by warping and coadding multiple visit_images covering a given sky map-defined patch. The process of building template_coadds is the same as that for deep_coadds, but the selection criteria differ between the two types of coadd. In the case of template_coadds, one-third of visit_images covering the patch in question with the narrowest PSF FWHM are selected. If one-third corresponds to fewer than 12 visit_images (i.e., there are fewer than 36 visit_images covering the patch), then the 12 visit_images with the narrowest PSF FWHM are selected. Finally, if there are fewer than 12 visit_images covering the patch, then all visit_images are selected. Of the 15,972 visit_images, 13,113 were used to create template_coadds. This selection strategy is designed to optimize for seeing when a patch is well covered by visit_images, yet still enable the production of template_coadds for poorly covered patches. As with deep_coadds, the number of visit_images that contributed to a template_coadd varies across the patch.

DP1 contains a total of 2730 template_coadds.⁹⁵ As with deep_coadds, a single template_coadd covers a single patch. Since the same sky map is used when creating both deep_coadd and template_coadds, the on-sky area and pixel count of template_coadds are the same as that of a deep_coadd (see above). Similarly, template_coadds contain the science image (i.e., the coadd), a variance image, and a pixel mask; all three contain the same number of pixels. Also included are the PSF model, WCS information, and metadata. As is the case for deep_coadds, those pixels within template_coadds that are not covered by any of the selected visit_images may still have seemingly valid values, but are indicated with the NO_DATA flag within the pixel mask.

3.1.5. *Difference_images*

Difference_images (NSF-DOE Vera C. Rubin Observatory 2025f) are generated by the subtraction of the warped, scaled, and PSF-matched template_coadd from the visit_image (see §4.6.1). In principle, only

⁹⁴ For storage space reasons, warped templates are not retained for DP1, as they can be readily and reliably recreated from the template_coadds.

⁹⁵ The difference in the number of deep_coadds and template_coadds is due to the difference in the visit_image selection criteria for each coadd.

those sources whose `flux` has changed relative to the `template_coadd` should be apparent (at a significant level) within a `difference_image`. In practice, however, there are numerous spurious sources present in `difference_images` due to unavoidably imperfect template matching.

In total, there are 15,972 `difference_images` in DP1, one for each `visit_image`.

Like `visit_images`, `difference_images` contain the science (i.e., difference) image, a variance image, and a pixel mask; all three contain the same number of pixels, which is the same as that of the input `visit_image`. Also included is the PSF model, WCS information, and `metadata`.

3.1.6. Background Images

Background images contain the model `background` that has been generated and removed from a science image. `Visit_images`, `deep_coadd` images and `template_coadd` images all have associated `background` images.⁹⁶ Background images contain the same number of pixels as their respective science image, and there is one `background` image for each `visit_image`, `deep_coadd`, and `template_coadd`. Difference-imaging analysis also measures and subtracts a `background` model, but the `difference_background` data product is not written out by default and is not part of DP1.

Background images are not available via the IVOA Service; they can only be accessed via the Butler Data Service.

3.2. Catalogs

In this section we describe science-ready tables produced by the science pipelines. All catalogs contain data for detections in the images described in §3.1, except the `Calibration` catalog, which contains reference data obtained from previous surveys. Observatory-produced `metadata` tables are described in §3.5.

The catalogs contains measurements for either sources detected in `visit_images` and `difference_images`, or objects detected in `deep_coadds`. All catalogs store fluxes rather than magnitudes, with fluxes measured in nanojanskies ($1 \text{ nJy} = 10^{-35} \text{ Wm}^{-2}\text{Hz}^{-1}$). Fluxes are preferred for multiepoch observations, as they can be averaged across epochs, unlike magnitudes. Additionally, flux measurements on difference images (§3.1) are computed against a template, representing a flux difference. As a result, flux measurements on difference images can

be negative, particularly for faint sources in the presence of noise.

The `Source`, `Object`, `ForcedSource`, `DiaSource`, `DiaObject`, and `ForcedSourceOnDiaObject` catalogs described below each vary in terms of their specific columns but generally contain: one or more unique identification numbers, positional information, multiple types of `flux` measurements (e.g., aperture fluxes, PSF fluxes, Gaussian fluxes, etc.), and a series of Boolean flags indicating characteristics such as saturation or cosmic-ray contamination for each source or object. The solar system catalogs `SSObject` and `SSSource` deviate from this general structure in that they instead contain orbital parameters for all known asteroids.

Where applicable, quantities are prefixed with the band in which they were measured, and all measured properties are reported with their associated 1σ uncertainties. For example, `g_ra` and `g_raErr` refer to R.A. and its uncertainty, measured in the *g* band.

Fluxes for various apertures are provided together with an uncertainty and a flag, and named in the format `[band]_ap[size]Flux`, where `[size]` is the aperture diameter in pixels. For example, `g_ap03Flux`, `g_ap03FluxErr`, `g_ap03Flux_flag` provide the flux, uncertainty and a flag measured within a 3.0 pixel aperture in the *g* band. Similarly for flux measurements using difference algorithms, e.g. `g_psfFlux` provides the flux derived using the PSF model as a weight function, forced on *g* band.

A complete list of columns with description and units for all tables in DP1 is available at <https://sdm-schemas.lsst.io/dp1.html> Since DP1 is a preview release, it does not include all the catalogs expected in a full LSST Data Release. Additionally, some catalogs may be missing columns, as not all quantities have been computed yet. These quantities will be included in future releases, and, where it is known to be the case, missing data are noted in the catalog descriptions that follow.

Catalog data are stored in the Qserv database (§6.5.1) and are accessible via Table Access Protocol (IVOA standard) (IVOA), and an online DP1 catalog schema is available at <https://sdm-schemas.lsst.io/dp1.html>. Catalog data are also accessible via the Data Butler (see §6.2.2).

3.2.1. Source Catalog

The `Source` catalog (NSF-DOE Vera C. Rubin Observatory 2025g) contains data on all sources which are, prior to deblending (§4.5.2), detected with a greater than 5σ significance in each individual visit. The detections reported in the `Source` catalog have undergone deblending; in the case of blended detections, only the

⁹⁶ In future Data Releases, `background` images may be included as part of their respective science image data product.

deblended sources are included in the `Source` catalog. It is important to note that while the criterion for inclusion in a `Source` catalog is a $> 5\sigma$ detection in a `visit_image` prior to deblending, the positions and fluxes are reported postdeblending. Hence, it is possible for the `Source` catalog to contain sources whose flux-to-error ratios, potentially of all types (i.e., aperture flux, PSF flux, etc.), are less than five.

In addition to the general information mentioned above (i.e., IDs, positions, fluxes, flags), the `Source` catalog also includes basic `shape` and extendedness information.

The `Source` catalog contains data for 46 million sources in DP1.

A cumulative histogram showing the PSF magnitudes of all sources contained within the `Source` catalogue is presented in the top panel of Figure 9

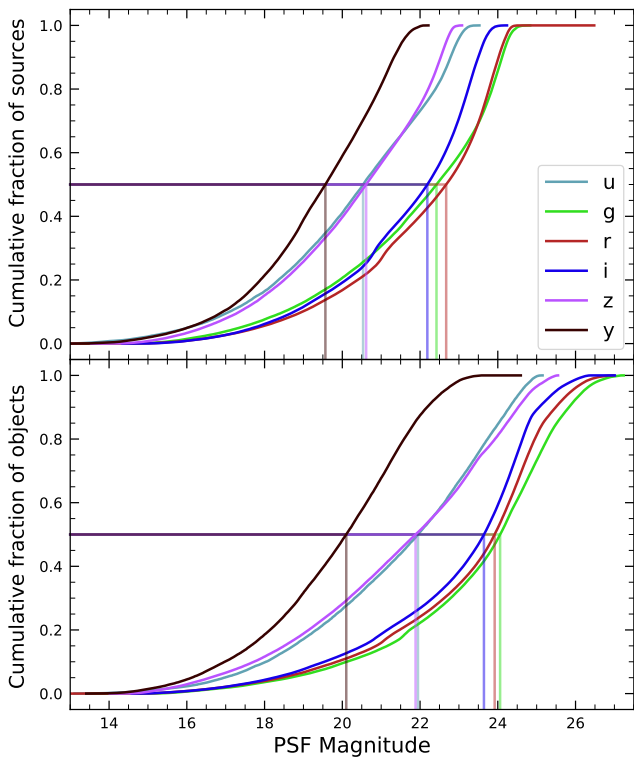


Figure 9. Normalized cumulative histograms of the PSF magnitudes of all $> 5\sigma$ -detected sources (top panel) and objects (bottom panel) contained in the `Source` and `Object` catalogs, respectively, separated according to band (see legend). The vertical lines indicate the 50th percentile for each band.

3.2.2. Object Catalog

The `Object` catalog (NSF-DOE Vera C. Rubin Observatory 2025h) contains data on all objects detected with a greater than 5σ significance in the `deep_coadds`.

With coadd images produced on a per-band basis, a $> 5\sigma$ detection in one or more of the bands will result in an object being included in the `Object` catalog. For cases where an object is detected at $> 5\sigma$ in more than one band, a crossmatching has been performed between bands to associate an object in one band with its counterpart(s) in the other bands. As such, the `Object` catalog contains data from multiple bands. The objects reported in the `Object` catalog have also undergone deblending; in the case of blended detections, only the deblended child objects are included in the catalog. As with the `Source` catalog, the criterion for inclusion in the `Object` catalog is a $> 5\sigma$ detection in one of the `deep_coadds` prior to deblending, yet the positions and fluxes of objects are reported postdeblending. Hence, it is possible for `Object` catalog to contain objects whose flux-to-error ratios — potentially of all types and in all bands — are less than five.

In addition to the general information mentioned above (i.e., IDs, positions, fluxes, and flags), the `Object` catalog also includes basic `shape` and extendedness information. While they may be included in future Data Releases, no photometric redshifts, Petrosian magnitudes (V. Petrosian 1976), proper motions or periodicity information are included in the DP1 object catalogs.

The `Object` catalog contains data for 2.3 million objects in DP1.

3.2.3. ForcedSource Catalog

The `ForcedSource` catalog (NSF-DOE Vera C. Rubin Observatory 2025i) contains forced PSF photometry measurements performed on both `difference_images` (i.e., the `psfDiffFlux` column) and `visit_images` (i.e., the `psfFlux` column) at the positions of all the objects in the `Object` catalog, to allow assessment of the time variability of the fluxes. We recommend using the `psfDiffFlux` column when generating light curves because this quantity is less sensitive to flux from neighboring sources than `psfFlux`. In addition to forced photometry PSF fluxes, a number of Boolean flags are also included in the `ForcedSource` catalog.

The `ForcedSource` catalog contains a total of 269 million entries across 2.3 million unique objects.

3.2.4. DiaSource Catalog

The `DiaSource` catalog (NSF-DOE Vera C. Rubin Observatory 2025j) contains data on all the sources detected at $> 5\sigma$ significance — including those associated with known solar system objects — in the `difference_images`. Unlike sources detected in `visit_images`, sources detected in difference images (hereafter, “DiaSources”) have gone through an association step in which an attempt has been made to associate them into

underlying objects called “DiaObjects”. The `DiaSource` catalog consolidates all this information across multiple visits and bands. The detections reported in the `DiaSource` catalog have not undergone deblending.

The `DiaSource` catalog contains data for 3.1 million `DiaSources` in [DP1](#).

3.2.5. *DiaObject Catalog*

The `DiaObject` catalog ([NSF-DOE Vera C. Rubin Observatory 2025k](#)) contains the astrophysical objects that `DiaSources` are associated with (i.e., the `DiaObjects`). The `DiaObject` catalog contains only non-solar-system objects; solar system objects are, instead, recorded in the `SSObject` catalog. When a `DiaSource` is identified, the `DiaObject` and `SSObject` catalogs are searched for objects to associate it with. If no association is found, a new `DiaObject` is created and the `DiaSource` is associated to it. Along similar lines, an attempt has been made to associate `DiaObjects` across multiple bands, meaning the `DiaObject` catalog, like the `Object` catalog, contains data from multiple bands. Since `DiaObjects` are typically [transient](#) or variable (by the nature of their means of detection), the `DiaObject` catalog contains summary statistics of their fluxes, such as the mean and standard deviation over multiple epochs; users must refer to the `ForcedSourceOnDiaObject` catalog (see below) or the `DiaSource` catalog for single-epoch [flux](#) measurements of `DiaObjects`.

The `DIAObject` catalog contains data for 1.1 million `DiaObjects` in [DP1](#).

3.2.6. *ForcedSourceOnDiaObject Catalog*

The `ForcedSourceOnDiaObject` catalog ([NSF-DOE Vera C. Rubin Observatory 2025l](#)) is equivalent to the `ForcedSource` catalog, but contains [forced photometry](#) measurements obtained at the positions of all the `DiaObjects` in the `DiaObject` catalog.

The `ForcedSourceOnDiaObject` catalog contains a total of 197 million entries across 1.1 million unique `DiaObjects`.

3.3. *SSObject Catalog*

The `SSObject` catalog ([NSF-DOE Vera C. Rubin Observatory 2025m](#)) and the [Minor Planet Center \(MPC\) Orbit Database \(MPCORB\)](#) carry information about solar system objects. The `MPCORB` table provides the `MPC`-computed orbital elements for all known asteroids, including those that Rubin discovered. For [DP1](#), the `SSObject` catalog serves primarily to provide the mapping between the [International Astronomical Union \(IAU\)](#) designation of an object (listed in the [Minor Planet Center Orbit database \(MPCORB\)](#)), and the internal `ssObjectId` identifier, which is used as a key to

find solar system object observations in the `DiaSource` and `SSSource` tables. The `SSObject` catalog contains data for 431 `SSObjects` in [DP1](#).

3.3.1. *SSSource Catalog*

The `SSSource` catalog ([NSF-DOE Vera C. Rubin Observatory 2025n](#)) contains data on all `DiaSources` that are either associated with previously known solar system objects, or have been confirmed as newly discovered solar system objects by confirmation of their orbital properties. As entries in the `SSSource` catalog stem from the `DiaSource` catalog, they have all been detected at $> 5\sigma$ significance in at least one band. The `SSSource` catalog contains data for 5988 solar system sources.

3.3.2. *CcdVisit Catalog*

The `CcdVisit` catalog ([NSF-DOE Vera C. Rubin Observatory 2025o](#)) contains data for all `CCD` images from a single visit. In principle, this means nine entries per visit, however due to a variety of technical reasons, not all `CCDs` have data for each visit, and so the catalog may contain fewer than nine entries per visit. In addition to technical information, such as the on-sky coordinates of the central pixel and measured pixel scale, the `CcdVisit` catalog contains a range of data quality measurements, such as whole-image summary statistics for the `PSF` size, zero-point, sky [background](#), sky noise, and quality of astrometric solution. It provides an efficient method to access `visit_image` properties without needing to access the image data. When combined with the data contained in the `Visit` table described in [§3.5](#), it provides a full picture of the telescope pointing and sky conditions at the time of observation.

The `CcdVisit` catalog contains 16,071 entries (nine entries for each of the 1786 visits, minus three entries for one incomplete visit). This differs from the number of `visit_images` due to the more stringent requirements imposed to generate a science-ready image.

3.3.3. *Calibration Catalog*

The `Calibration` catalog is the reference catalog that was used to perform astrometric and photometric [calibration](#). It is a whole-sky catalog built specifically for [LSST](#), as no single prior reference catalog had both the depth and coverage needed to calibrate [LSST](#) data. It combines data from multiple previous reference catalogs and contains only stellar sources. Full details on how the `Calibration` catalog was built are provided in [P. S.](#)

1212 Ferguson et al. (2025)⁹⁷. We provide a brief summary
1213 here.

1214 For the *grizy* bands, the input catalogs were (in order
1215 of decreasing priority): Dark Energy Survey (DES)
1216 Year 6 Calibration Stars (E. S. Rykoff et al. 2023); Gaia
1217 B or R Photometry (Gaia) (XP) synthetic magnitudes
1218 (Gaia Collaboration et al. 2023a); the Panoramic Survey
1219 Telescope and Rapid Response System (Pan-STARRS)
1220 3PI survey (K. C. Chambers et al. 2016); Data Release
1221 2 of the Skymapper survey (C. A. Onken et al. 2019);
1222 and Data Release 4 of the VLT Survey Telescope (VST)
1223 Asteroid Terrestrial-impact Last Alert System (ATLAS)
1224 survey (T. Shanks et al. 2015). For the *u* band, the input
1225 catalogs were (in order of decreasing priority): standard
1226 stars from Sloan Digital Sky Survey (SDSS) Data Re-
1227 lease 16 (R. Ahumada et al. 2020); Gaia XP Synthetic
1228 Magnitudes (Gaia Collaboration et al. 2023a); and syn-
1229 thetic magnitudes generated using Single Lens Reflex
1230 (SLR), which estimates the *u*-band flux from the *g*-band
1231 flux and *g - r* colors. These SLR estimates were used to
1232 boost the number of *u*-band reference sources, as other-
1233 wise the source density from the *u*-band input catalogs
1234 is too low to be useful for the LSST.

1235 Only stellar sources were selected from each input cat-
1236 alog. Throughout, the Calibration catalog uses the
1237 DES bandpasses for the *grizy* bands and the SDSS band-
1238 pass for the *u*-band; color transformations derived from
1239 high-quality sources were used to convert fluxes from
1240 the various input catalogs (some of which did not use
1241 the DES or SDSS bandpasses) to the respective band-
1242 passes. All sources from the input catalogs are matched
1243 to Gaia Data Release 3 (DR3) sources for robust astro-
1244 metric information, selecting only isolated sources (i.e.,
1245 no neighbors within 1").

1246 After collating the input catalogs and transforming
1247 the fluxes to the standard DES and SDSS bandpasses,
1248 the catalog was used to identify sources within a spe-
1249 cific region of the sky. This process generated a set of
1250 standard columns containing positional and flux infor-
1251 mation, along with their associated uncertainties.

1252 3.3.4. Source and Object Designations

1253 To refer to individual sources or objects from the DP1
1254 catalogs, one should follow the LSST-DP1 naming con-
1255 vention that has been registered with the IAU. Because
1256 the Source, Object, DiaSource, DiaObject, and SSOb-
1257 ject tables each have their own unique IDs, their des-
1258 ignations should differ. In general, source and object

1259 designations should begin with the string “LSST-DP1”
1260 (denoting the LSST, DP 1), followed by a string spec-
1261 ifying the table from which the source was obtained.
1262 These strings should be “O” (for the Object table),
1263 “S” (Source), “DO” (DiaObject), “DS” (DiaSource),
1264 or “SSO” (SSObject). Following the table identifier, the
1265 designation should contain the full unique numeric iden-
1266 tifier from the specified table (i.e., the objectId, sour-
1267 ceId, diaObjectId, diaSourceId, or ssObjectId). Each
1268 component of the identifier should be separated by
1269 dashes, resulting in a designation such as “LSST-DP1-
1270 TAB-123456789012345678”. In summary, source desig-
1271 nations should adhere to the formats listed below.

- 1272 • Object. LSST-DP1-O-609788942606161356 (for
1273 objectId 609788942606161356).
- 1274 • Source. LSST-DP1-S-600408134082103129 (for
1275 sourceId 600408134082103129).
- 1276 • DiaObject. LSST-DP1-DO-609788942606140532
1277 (for diaObjectId 609788942606140532).
- 1278 • DiaSource. LSST-DP1-DS-600359758253260853
1279 (for diaSourceId 600359758253260853).
- 1280 • SSObject. LSST-DP1-SSO-21163611375481943
1281 (for ssObjectId 21163611375481943).

1282 Tables that were not explicitly mentioned in the de-
1283 scription above do not have their own unique IDs, but
1284 are instead linked to one of the five tables listed above
1285 via a unique ID. For example, the ForcedSource table
1286 uses objectId, ForcedSourceOnDiaObject uses diaOb-
1287 jectIds, SSSource uses diaSourceIds and ssObjectIds,
1288 and MPCORB uses ssObjectIds.

1289 3.4. Maps

1290 Maps are two-dimensional visualizations of survey
1291 data. In DP1, these fall into two categories: Sur-
1292 vey Property maps and Hierarchical Progressive Survey
1293 (HiPS) maps (P. Fernique et al. 2015).

1294 3.4.1. Survey Property Maps

1295 Survey Property maps (NSF-DOE Vera C. Rubin Ob-
1296 servatory 2025p) summarize how properties such as ob-
1297 serving conditions or exposure time vary across the ob-
1298 served sky. Each map provides the spatial distribution
1299 of a specific quantity at a defined sky position for each
1300 band by aggregating information from the images used
1301 to make the deep_coadd. Maps are initially created per
1302 tract and then combined to produce a final consolidated
1303 map. At each sky location, represented by a spatial pixel
1304 in the Hierarchical Equal-Area iso-Latitude Pixelisation

⁹⁷ In P. S. Ferguson et al. (2025), the calibration reference catalog is referred to as “The Monster”. This terminology is also carried over to the DP1 Butler.

(HEALPix)(K. M. Górski et al. 2005) grid, values are derived using statistical operations, such as minimum, maximum, mean, weighted mean, or sum, depending on the property.

DP1 contains 14 Survey Property maps. The available maps describe total exposure times, observation epochs (one each for the earliest, mean, and latest observation epoch), PSF size and shape (one for each of the e^1 and e^2 shape parameters; see §5.2), PSF magnitude limits, sky background and noise levels, as well as astrometric shifts (one each for R.A. and decl.) and PSF distortions (one for each of the e^1 and e^2 shape parameters) due to wavelength-dependent atmospheric Differential Chromatic Refraction (DCR) effects. They all use the dataset type format `deep_coadd_<PROPERTY>_consolidated_map_<STATISTIC>`. For example, `deep_coadd_exposure_time_consolidated_map_sum` provides a spatial map of the total exposure time accumulated per sky position in units of seconds. All maps are stored in HealSparse⁹⁸ format. Survey Property maps are only available via the Data Butler (§6.2.2).

Figure 10 presents three Survey Property maps for exposure time, PSF magnitude limit, and sky noise, computed for representative tracts and bands. Because full consolidated maps cover widely separated tracts, we use clipped per-tract views here to make the spatial patterns more discernible.

3.4.2. HiPS Maps

HiPS maps (P. Fernique et al. 2015), offer an interactive way to explore seamless, multiband tiles of the sky regions covered by DP1, allowing for smooth panning and zooming. DP1 provides multiband HiPS images created by combining data from individual bands of `deep_coadd` and `template_coadd` images, using an improved version (N. B. Lust et al. in preparation) of the algorithm presented in (R. Lupton et al. 2004). These images are false-color representations generated using various filter combinations for the red, green, and blue channels.

The available filter combinations include *gri*, *izy*, *riz*, and *ugr* for both `deep_coadds` and `template_coadds`. Additionally, for `deep_coadd` only, we provide color blends such as *uug* and *grz*. Post DP1, we plan to also provide single-band HiPS images for all *ugrizy* bands in both Portable Network Graphics (PNG) and FITS formats.

⁹⁸ A sparse HEALPix representation that efficiently encodes data values on the celestial sphere. <https://healsparse.readthedocs.io>

HiPS maps are only accessible through the HiPS viewer in the RSP Portal (§6.3) and cannot be accessed via the Data Butler (§6.2.2). All multiband HiPS images are provided in PNG format.

3.5. Metadata

DP1 also includes metadata about the observations, which are stored in the `Visit` table. We distinguish it from a catalog as the data it contains were produced by the observatory directly, rather than the science pipelines. The `Visit` table contains technical data for each visit, such as telescope pointing, camera rotation, airmass, exposure start and end time, and total exposure time. Some of the information contained within the `Visit` table is also contained in the `CCDVisit` catalog described in §3.2 (e.g., exposure time), although the latter also includes information produced by the processing pipelines at the per-detector level, such as the PSF size and limiting magnitudes of a given `visit_image`.

3.6. Ancillary Data Products

DP1 also includes several ancillary data products. While we do not expect most users to need these, we describe them here for completeness. All the data products described in this section can only be accessed via the Data Butler (§6.2.2).

3.6.1. Standard Bandpasses

Figure 3 shows the full-system throughput of the six LSSTComCam filters. The corresponding transmission curves are provided as a DP1 data product. These datasets tabulate the full-system transmission of the six LSSTComCam filters as a function of wavelength and were used as a reference for the LSSTComCam DP1 photometry. The `standard_passband` dataset is keyed by band and is stored in Astropy table format.

3.6.2. Task Configuration Files, Logs, and Metadata

DP1 includes provenance-related data products such as task logs, configuration files, and task metadata. Configuration files record the parameters used in each processing task, while logs and metadata contain information output during processing. These products help users understand the processing setup and investigate potential processing failures.

3.6.3. Calibration Data Products

Calibration data products include a variety of images and models that are used to characterize and correct the performance of the camera and other system components. These include bias, dark, and flat-field images, Photon Transfer Curve (PTC) gains, brighter-fatter kernels (P. Antilogus et al. 2014), charge transfer

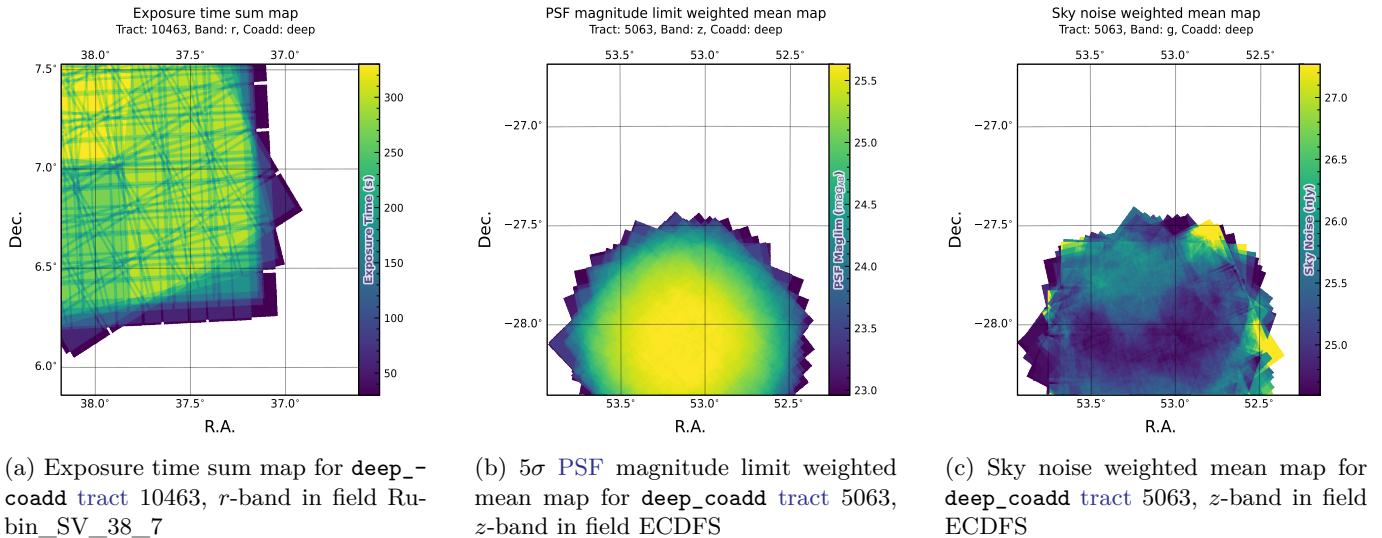


Figure 10. Examples of Survey Property maps from Rubin DP1 across different bands, clipped to the boundary of a single tract for visual clarity.

1400 inefficiency (CTI) models, linearizers, and illumination
 1401 corrections. For flat-field corrections, DP1 processing
 1402 used combined flats, which are averaged from multiple
 1403 individual flat-field exposures to provide a stable cali-
 1404 bration. These calibration products are essential inputs
 1405 to Instrument Signal Removal (ISR) (§4.2.1). While
 1406 these products are included in DP1 for transparency and
 1407 completeness, users should not need to rerun ISR for
 1408 their science and are advised to start with the processed
 1409 `visit_image`.

1410 4. DATA RELEASE PROCESSING

1411 **Data Release Processing (DRP)** is the systematic pro-
 1412 cessing of all Rubin Observatory data collected up to
 1413 a certain date to produce the calibrated images, cata-
 1414 logs of detections, and derived data products described
 1415 in Section 3. DP1 was processed entirely at the United
 1416 States Data Facility (USDF) at SLAC using 17,024 CPU
 1417 hours.⁹⁹

1418 This section describes the pipeline algorithms used to
 1419 produce DP1 and how they differ from those planned
 1420 for full-scale LSST Data Releases. DRP consists of four
 1421 major stages: (1) single-frame processing, (2) calibra-
 1422 tion, (3) coaddition, and (4) difference image analysis
 1423 (DIA).

1424 4.1. LSST Science Pipelines Software

1425 The LSST Science Pipelines software (Rubin Observa-
 1426 tory Science Pipelines Developers 2025; J. D. Swinbank

⁹⁹ For future Data Releases, data processing will be distributed across the USDF, the French Data Facility and the UK Data Facility.

1427 *et al.* 2020) will be used to generate all Rubin Observa-
 1428 tory and LSST data products. They provide both
 1429 the algorithm and middleware frameworks necessary to
 1430 process raw data into science-ready data products, en-
 1431 abling analysis by the Rubin scientific community. Ver-
 1432 sion v29.1 of the pipelines was used to produce DP1¹⁰⁰.

1433 4.2. Single-frame Processing

1434 4.2.1. Instrument Signature Removal

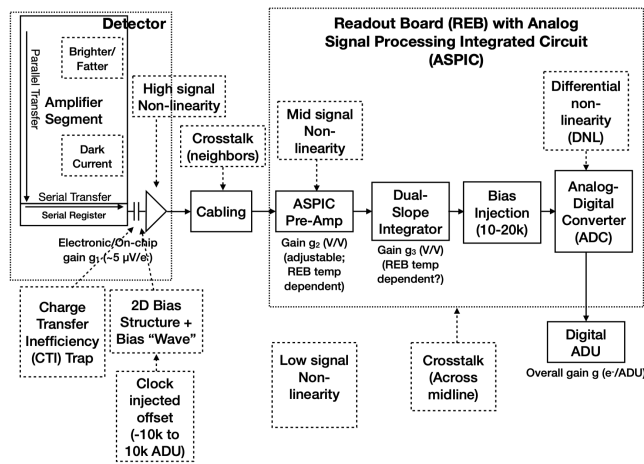
1435 The first step in processing LSSTComCam images is
 1436 to correct for the effects introduced by the telescope and
 1437 detector. Each sensor and its readout amplifiers can
 1438 vary slightly in performance, causing images of even a
 1439 uniformly illuminated focal plane to exhibit discontinu-
 1440 ities and shifts due to detector effects. The ISR pipeline
 1441 aims to recover the original astrophysical signal as best
 1442 as possible and produce science-ready single-epoch im-
 1443 ages for source detection and measurement. A detailed
 1444 description of the ISR procedures can be found in P. Fa-
 1445 greglius & E. S. Rykoff (2025) and A. A. Plazas Malagón
 1446 *et al.* (2025). Figure 11 illustrates the model of detector
 1447 components and readout electronics and their impact
 1448 on the signal, tracing the process from photons incident
 1449 on the detector surface to the final quantized values¹⁰¹
 1450 recorded in the image files. The ISR pipeline essentially
 1451 “works backward” through the signal chain, correcting
 1452 the integer analog-to-digital units (ADUs) raw camera

¹⁰⁰ Documentation for this version is available at https://pipelines.lsst.io/v29_1_1

¹⁰¹ The images written to disk by the camera have values that are integers that come from the analog-to-digital converter converting an analog voltage.

1453 output back to a floating-point number of photoelectrons created in the silicon. The physical detector, represented on the left in Figure 11, is the source of effects that arise from the silicon itself, such as the dark current and the brighter-fatter effect (A. A. Plazas et al. 2018; A. Broughton et al. 2024). After the integration time has elapsed, the charge is shifted to the serial register and read out, which can introduce CTIs and a clock-injected offset level. The signals for all amplifiers are transferred via cables to the Readout Electronics Board (REB), during which cross talk between the amplifiers may occur. The Analog Signal Processing Integrated Circuit (ASPIC) on the REB converts the analog signal from the detector into a digital signal, adding both quantization and a bias level to the image. Although the signal chain is designed to be stable and linear, the presence of numerous sources of nonlinearity indicates otherwise.

1471 Flat-fielding for DP1 was performed using combined flats produced from twilight flats acquired with sufficient rotational dithering to mitigate artifacts from print-through stars, as described in §2.3. The ISR pro-



1475 **Figure 11.** The model of the detector and REB components, labeled with the effects that they impart on signal.

1476
1477 cessing pipeline for DP1 performs, in the following order: Analogue-to-Digital Unit (ADU) dithering to reduce quantization effects, serial overscan subtraction, saturation masking, gain normalization, cross-talk correction, parallel overscan subtraction, linearity correction, serial CTI correction, image assembly, bias subtraction, dark subtraction, brighter-fatter correction, defect masking and interpolation, variance plane con-

1485 struction, flat-fielding, and amplifier offset (amp-offset) correction¹⁰².

1487 4.2.2. Background Subtraction

1488 The background subtraction algorithms in the LSST Science Pipelines estimate and remove large-scale background signals from science imaging. Such signals may include sky brightness from airglow, moonlight, scattered light instrumental effects, zodiacal light, and diffuse astrophysical emission. In so doing, true astrophysical sources are isolated to allow for accurate detection and measurement.

1496 To generate a background model, each post-ISR image is divided into superpixels of 128×128 pixels. Pixels with a mask flag set that indicates that they contain no useful science data or that they contain flux from a preliminary source detection are masked. The iterative 3σ clipped mean of the remaining pixels is calculated for each superpixel, constructing a background statistics image. A sixth-order Chebyshev polynomial is fit to these values on the scale of a single detector to allow for an extrapolation back to the native pixel resolution of the post-ISR image.

1507 4.3. Calibration

1508 Stars are detected in each post-ISR image using a 5σ threshold. Detections of the same star across multiple images are then associated to identify a consistent set of isolated stars with repeated observations suitable for use in PSF modeling, photometric calibration, and astrometric calibration.

1514 Initial astrometric and photometric solutions are derived using only the calibration reference catalogs (see §3.2), and an initial PSF model is fit using PSFEx (E. Bertin 2011). These preliminary solutions provide approximate source positions, fluxes, and PSF shapes that serve as essential inputs to the calibration process, enabling reliable source matching, selection of high-quality stars, and iterative refinement of the final astrometric, photometric, and PSF models. These preliminary solutions are subsequently replaced by more accurate fits, as described in the following sections.

1525 4.3.1. Point-spread Function Modeling

1526 PSF modeling in DP1 uses the Piff (M. Jarvis et al. 2021b) package. Our configuration of Piff utilizes its

1527 ¹⁰² Amp-offset corrections are designed to address systematic discontinuities in background sky levels across amplifier boundaries. The implementation in the LSST Science Pipelines is based on the Pan-STARRS pattern continuity algorithm (C. Z. Waters et al. 2020).

PixelGrid model with a fourth-order polynomial interpolation per CCD, except in the u band, where star counts are insufficient to support a fourth-order fit. In this case, a second-order polynomial is used instead. Details on the choice of polynomial order, overall PSF modeling performance, and known issues are discussed in §5.2.

4.3.2. Astrometric Calibration

Starting from the astrometric solution calculated in single-frame processing (§4.2), the final astrometric solution is computed using the ensemble of visits in a given band that overlap a given tract. This allows the astrometric solution to be further refined by using all of the isolated point sources of sufficient signal-to-noise ratio in an image, rather than only those that appear in the reference catalog, as is done in single-frame processing. Using multiple whole visits rather than a single detector also allows us to account for effects that impact the full focal plane, and for the proper motion and parallax of the sources.

In order to perform the fit of the astrometric solution, isolated point sources are associated between overlapping visits and with the Gaia DR3 (Gaia Collaboration et al. 2023b) reference catalog where possible. The model used for DP1 consists of a static map from pixel space to an intermediate frame (the per-detector model), followed by a per-visit map from the intermediate frame to the plane tangent to the telescope boresight (the per-visit model), then finally a deterministic mapping from the tangent plane to the sky. The fit is done using the `gbdes` package (G. M. Bernstein et al. 2017), and a full description is given in C. Saunders (2024).

The per-detector model is intended to capture quasi-static characteristics of the telescope and camera. During Rubin Operations, the astrometric solution will allow for separate epochs with different per-detector models, to account for changes in the camera due to warming and cooling and other discrete events. However, for DP1, LSSTComCam was assumed to be stable enough that all visits use the same per-detector model. The model itself is a separate two-dimensional polynomial for each detector. For DP1, a fourth-degree polynomial was used; the degree of the polynomial mapping is tuned for each instrument and may be different for LSSTCam. Further improvements may be made by including a pixel-based astrometric offset mapping, which would be fit from the ensemble of astrometric residuals, but this is not included in the DP1 processing.

The per-visit model attempts to account for the path of a photon from both atmospheric sources and those dependent on the telescope orientation. This model is

also a polynomial mapping, in this case a sixth-degree two-dimensional polynomial. Correction for DCR (§5.4) was not done for DP1, but will be included in LSSTCam processing during Rubin Operations. Future processing will also likely include a Gaussian process fit to better account for atmospheric turbulence, as was demonstrated by W. F. Fortino et al. (2021) and P. F. Léget et al. (2021).

The final component of the astrometric calibration involves the positions of the isolated point sources included in the fit, which are described by five parameters: sky coordinates, proper motion, and parallax. While proper motions and parallaxes are not released for DP1, they are fitted for these sources in the astrometric solution to improve the astrometric calibration.

4.3.3. Photometric Calibration

Photometric calibration of the DP1 dataset is based on the Forward Global Calibration Method (FGCM) (D. L. Burke et al. 2018), adapted for the LSST Science Pipelines (H. Aihara et al. 2022; P. Fagrelus & E. S. Rykoff 2025). We used the FGCM to calibrate the full DP1 dataset with a forward model that uses a parameterized model of the atmosphere as a function of airmass along with a model of the instrument throughput as a function of wavelength. The FGCM process typically begins with measurements of the instrumental throughput, including the mirrors, filters, and detectors. However, because full scans of the LSSTComCam as-built filters and individual detectors were not available, we instead used the nominal reference throughputs for the Simonyi Survey Telescope and LSSTCam.¹⁰³ These nominal throughputs were sufficient for the DP1 calibration, given the small and homogeneous focal plane consisting of only nine ITL detectors. The FGCM atmosphere model, provided by MODTRAN (A. Berk et al. 1999), was used to generate a look-up table for atmospheric throughput as a function of zenith distance at Cerro Pachón. This model accounts for absorption and scattering by molecular constituents of the atmosphere, including O_2 and O_3 ; absorption by water vapor; and Mie scattering by airborne aerosol particulates. Nightly variations in the atmosphere are modeled by minimizing the variance in repeated observations of stars with a Signal to Noise Ratio (SNR) greater than 10, measured using “compensated aperture fluxes”. These fluxes include a local background subtraction (see §4.2.2) to mitigate the impact of background offsets. The model fitting process incorporates all six bands (*ugrizy*) but does not include any gray (achromatic) terms, except

¹⁰³ Available at: <https://github.com/lst/throughputs/tree/1.9>

for a linear assumption of mirror reflectance degradation, which is minimal over the short duration of the DP1 observation campaign. As an additional constraint on the fit, we use a subset of stars from the reference catalog (P. S. Ferguson et al. 2025), primarily to constrain the system’s overall throughput and establish the “absolute” calibration.

Photometric transformation relations between LSST-Cam and LSSTComCam systems and other photometric systems are under development and are provided in (M. N. Porter et al. 2026)

4.4. *Visit_images and Source Catalogs*

With the final PSF models, WCS solutions, and photometric calibrations in place, we reprocess each single-epoch image to produce a final set of calibrated `visit_images` and `Source` catalogs. Source detection is performed down to a 5σ threshold using the updated PSF models, followed by measurement of PSF and aperture fluxes. These catalogs represent the best single-epoch source characterization, but they are not intended for constructing light curves. For time-domain analysis, we recommend using the `forced photometry` tables described in §4.6.2.

4.5. *Coaddition Processing*

4.5.1. *Coaddition*

Only exposures with a `seeing` better than $1''.7$ FWHM are included in the `deep_coadd` images. For the `template_coadds`, typically only the top third of visits with the best `seeing` are used (although see §3.1 for more details), resulting in an even tighter image quality cutoff for the `template_coadds`. Exposures with poor PSF model quality, identified using internal diagnostics, are excluded to prevent contamination of the coadds with unreliable PSF estimates. The remaining exposures are combined using an inverse-variance weighted mean stacking algorithm.

To mitigate transient artifacts before coaddition, we apply the artifact rejection procedure described in Y. AlSayyad (2018), which identifies and masks features such as satellite trails, optical ghosts, and cosmic rays. It operates on a time series of PSF-matched images resampled onto a common pixel grid (“warps”) and leverages their temporal behavior to distinguish persistent astrophysical sources from transient artifacts.

Artifact rejection uses both direct (where no PSF matching is performed) and PSF-matched warps, homogenized to a standard PSF of $1''.8$ FWHM, broadly consistent with the $1''.7$ FWHM `seeing` threshold used in data screening. A sigma-clipped mean of the PSF-matched warps serves as a static sky model, against

which individual warps are differenced to identify significant positive and negative residuals. Candidate artifact regions are classified as `transient` if they appear in fewer than a small percentage of the total number of exposures, with the threshold based on the number of visits, N , as follows:

- $N = 1$ or 2 and threshold = 0 (no clipping),
- $N = 3$ or 4 and threshold = 1,
- $N = 5$ and threshold = 2,
- $N > 5$ and threshold = $2 + 0.03N$,

Identified `transient` regions are masked before coaddition, improving image quality and reducing contamination in derived catalogs.

4.5.2. *Detection, Deblending and Measurement*

After constructing coadded images, sources are detected in each band, merged across bands, deblended, and measured to generate the final object catalogs (§3.2). For each coadd in all six bands, we perform source detection at a 5σ detection threshold and then adjust the background with a per-patch constant (coadds are built from background-subtracted images, but the deeper detection on coadds redefines what is considered source versus background). Detections across bands are merged in a fixed priority order, *irzygu*, to form a union detection catalog, which serves as input to deblending.

Deblending is performed using the Scarlet Lite algorithm, which implements the same model as Scarlet (P. Melchior et al. 2018), but operates on a single pixel grid. This allows the use of analytic gradients, resulting in greater computational speed and memory efficiency.

Object measurement is then performed on the deblended detection footprints in each band. Measurements are conducted in three modes: independent per-band measurements, forced measurements in each band, and multiband measurements.

Most measurement algorithms operate through a single-band plugin system, largely as originally described in J. Bosch et al. (2018). The same plugins are run separately for each object on a deblended image, which uses the Scarlet model as a template to reweight the original noisy coadded pixel values. This effectively preserves the original image in regions where objects are not blended, while dampening the noise elsewhere.

A reference band is chosen for each object based on detection significance and measurement quality using the same priority order as detection merging (*irzygu*) and a second round of measurements is performed in forced

mode using the shape and position from the reference band to ensure consistent colors (J. Bosch et al. 2018).

Measurement algorithm outputs include object fluxes, centroids, and higher-order moments thereof like sizes and shapes. A variety of flux measurements are provided, from aperture fluxes and forward modeling algorithms.

Composite model (CModel) magnitudes (K. Abazajian et al. 2004; J. Bosch et al. 2018) are used to calculate the extendedness parameter, which functions as a star-galaxy classifier. Extendedness is a binary classifier that is set to one if the PSF model flux is less than 98.5% of the (free, not forced) CModel flux in a given band. Additionally, the extendedness in the reference band is provided as a separate column for convenience as a multiband star-galaxy classification, and is recommended generally but also specifically for objects with low SNR ratio in some bands.

Gaussian aperture and PSF (Gaussian Aperture and PSF (GAaP) K. Kuijken 2008; A. Kannawadi 2025) fluxes are provided to ensure consistent galaxy colors across bands. Sérsic model (J. L. Sérsic 1963; J. L. Sérsic 1968) fits are run on all available bands simultaneously using (MultiProFit; D. S. Taranu 2025). The resulting Sérsic model fluxes are provided as an alternative to CModel and are intended to represent total galaxy fluxes. Like CModel, the Sérsic model is a Gaussian mixture approximation to a true Sérsic profile, convolved with a Gaussian mixture approximation to the PSF. Sérsic model fits also include a free centroid, with all other structural parameters shared across all bands. That is, the intrinsic model has no color gradients, but the convolved model may have color gradients if the PSF parameters vary significantly between bands.

CModel measurements use a double “shapelet” (A. Refregier 2003) PSF model with a single shared shape. The Sérsic fits are intended to use a double Gaussian with independent shape parameters for each component. Due to a pipeline misconfiguration, the Sérsic fits actually used the shapelet PSF parameters, with the higher-order terms ignored (since MultiProFit does not support shapelet PSFs). This bug is not expected to impact the galaxy fluxes significantly, since the higher-order shapelet PSF parameters tend to be small, and the fix will be applied in future campaigns. Either way, the double-Gaussian PSF parameters are included for each object.

Further details on the performance of these algorithms are found in §5.7.

4.6. Variability Measurement

4.6.1. Difference-imaging Analysis

Difference Image Analysis (DIA) uses the decorrelated Alard and Lupton image differencing algorithm (D. J. Reiss & R. H. Lupton 2016). We detected both positive and negative DIASources at 5σ in the difference image. Sources with footprints containing both positive and negative peaks due to offsets from the template position or blending were fit with a dipole centroid code, which simultaneously fits offset positive and negative PSFs. We filter the resulting DIASource catalog to remove detections with pixel flags indicative of artifacts, nonastrophysical trail lengths, or unphysically negative direct fluxes. Finally, we perform a simple spatial association of DIASources into DIAObjects using a $1''$ matching radius.

The machine learning reliability model applied to DP1 was developed with the aim to meet the latency requirements for Rubin Alert Production when executed on CPUs. Accordingly we developed a relatively simple model: a convolutional neural network with three convolutional layers, and two fully connected layers. The convolutional layers have a 5×5 kernel size, with 16, 32, and 64 filters, respectively. A max-pooling layer of size two is applied at the end of each convolutional layer, followed by a dropout layer of 0.4 to reduce overfitting. The last fully connected layers have sizes of 32 and 1. The ReLU activation function is used for the convolutional layers and the first fully connected layer, while a sigmoid function is used for the output layer to provide a probabilistic interpretation. The cutouts are generated by extracting postage stamps of 51×51 pixels centered on the detected sources. The input data of the model consist of the template, science, and difference image stacked to have an array of `shape` (3, 51, 51). The model is implemented using PyTorch (J. Ansel et al. 2024). The binary cross entropy loss function was used, along with the Adaptive Moment Estimation (Adam) optimizer with a fixed learning rate of 1×10^{-4} , weight decay of 3.6×10^{-2} , and a batch size of 128. The final model uses the weights that achieved the best precision and purity for the test set. Training was done on the SLAC Shared Scientific Data Facility (S3DF) with an NVIDIA model L40S GPU.

The model was initially trained using simulated data from the second DESC Data Challenge (DC2; (LSST Dark Energy Science Collaboration (LSST DESC) et al. 2021)) plus randomly located injections of PSFs to increase the number of real sources, for a total of 89,066 real sources. The same number of bogus sources were selected at random from noninjected DIASources. Once the LSSTComCam data were available, the model was

1827 fine-tuned on a subset of the data containing 183,046
 1828 sources with PSF injections. On the `LSSTComCam` test
 1829 set, the model achieved an accuracy of 98.06%, a purity
 1830 of 97.87%, and a completeness of 98.27%. As discussed
 1831 in §5.8, the injections used to train this model version
 1832 do not capture all types of astrophysical variability, so
 1833 performance on the test set will not be representative for
 1834 variable stars, comets, and other types of variable ob-
 1835 jects. The machine learning reliability score, reported in
 1836 the `reliability` column of the `DIASource` catalog, is
 1837 a scalar value between zero and one that quantifies the
 1838 model’s confidence that a given detection is astrophys-
 1839 cal.

1840 4.6.2. Light Curves

1841 To produce light curves, we perform multiepoch
 1842 `forced photometry` on both the direct visit images and
 1843 the difference images. For light curves we recom-
 1844 mend the `forced photometry` on the difference images
 1845 (`psfDiffFlux` on the `ForcedSource` Table), as it isolates
 1846 the variable component of the flux and avoids contam-
 1847 ination from static sources. In contrast, `forced pho-`
 1848 `tometry` on direct images includes flux from nearby or
 1849 blended static objects, and this contamination can vary
 1850 with seeing. Centroids used in the multi-epoch `forced`
 1851 `photometry` stage are taken either from object positions
 1852 measured on the coadds or from the `DIAObjects` (the
 1853 associated `DIASources` detected on difference images).

1854 4.6.3. Solar System Processing

1855 Solar system processing in `DP1` consists of two key
 1856 components: the association of observations (sources)
 1857 with known solar system objects, and the discovery of
 1858 previously unknown objects by linking sets of *track-*
 1859 *lets*¹⁰⁴.

1860 The association component begins by generating ex-
 1861 pected positions for all objects in the `MPC` orbit cata-
 1862 log, using ephemerides computed with the `Sorcha` sur-
 1863 vey simulation toolkit (S. R. Merritt et al. 2025)¹⁰⁵.
 1864 To enable fast lookup of objects potentially present in
 1865 an observed visit, we use the `mpsky` package (M. Ju-
 1866 ric 2025). In each image, the closest `DiaSource` within
 1867 1” of a known solar system object’s predicted position
 1868 is associated to that object. In `DP1` we used a simple
 1869 positional association to tag `DiaSources` that are likely
 1870 observations of known asteroids. The 1” radius is inten-
 1871 tionally generous; we did not see evidence of mismatches

1872 at `DP1` depth and volume. This radius will be tuned for
 1873 future processing campaigns.

1874 The discovery component of solar system processing
 1875 uses the `heliolinx` package¹⁰⁶, which provides tools
 1876 for asteroid identification and linking (A. Heinze et al.
 1877 2023). The repository contains code for the following
 1878 tasks:

- 1879 • tracklet creation with `make_tracklets`
- 1880 • multi-night `tracklet` linking with an algorithm
- 1881 • linkage post processing (orbit fitting, outlier rejec-
 1882 tion, and deduplication) with `link_purify`

1883 The inputs to the discovery processing comprised
 1884 all sources detected in difference images, regardless of
 1885 whether they were tagged in the association step. These
 1886 inputs were produced by an early processing of `LSST-`
 1887 `ComCam` commissioning data, some of which were later
 1888 rejected during `DP1` processing and therefore do not ap-
 1889 pear in the final `DP1` data products.

1890 About 10% of all commissioning visits targeted the
 1891 near-ecliptic field `Rubin_SV_38_7`, chosen to facilitate
 1892 asteroid discovery. `Rubin_SV_38_7` produced the vast
 1893 majority of asteroid discoveries in `DP1`, as expected, but
 1894 a few were found in off-ecliptic fields as well.

1895 Tracklet creation with `make_tracklets` used an up-
 1896 per limit angular velocity of $1^{\circ}5 \text{ day}^{-1}$, faster than any
 1897 main belt asteroid and in the range of many `Near-Earth`
 1898 `Object (NEO)` discoveries. While no formal minimum
 1899 angular velocity was imposed, in practice it would be
 1900 unlikely to detect objects moving slower than about $0^{\circ}01$
 1901 day^{-1} . To minimize false `tracklets` from fields observed
 1902 multiple times per night, the minimum `tracklet` length
 1903 was set to three detections, and a minimum on-sky mo-
 1904 tion of 5” was required for a valid `tracklet`. To claim a
 1905 discovery candidate, we required tracklets to be linked
 1906 across at least three nights.

1907 Multinight `tracklet` linking is the heart of solar system
 1908 discovery, which connects (“links”) tracklets belonging
 1909 to the same object over a series of nights. It employs the
 1910 `HelioLinC3D` algorithm (S. Ettl et al. 2020; A. Heinze
 1911 et al. 2022), a refinement of the original `HelioLinC`
 1912 algorithm of M. J. Holman et al. (2018). Each processing
 1913 run tested each `tracklet` with 324 different hypotheses
 1914 spanning heliocentric distances from 1.5 to 9.8 `astro-`
 1915 `nomical unit (au)` and radial velocities spanning the full
 1916 range of possible bound orbits (an eccentricity of 0.0
 1917 to nearly 1.0). The upper limit of 10 `au` was chosen
 1918 because searches targeting more distant populations re-
 1919 quire different parameter choices. This range of distance

¹⁰⁴ A tracklet is defined as two or more detections of a moving
 object candidate taken in close succession in a single night.

¹⁰⁵ Available at <https://github.com/dirac-institute/sorcha>

¹⁰⁶ <https://github.com/heliolinx/heliolinx>

encompasses all main belt asteroids and Jupiter Trojans, as well as many comets, Mars-crossers and some NEOs. A dedicated search for objects at heliocentric distances out to 50 au was also conducted; no distant objects were detected, consistent with expectations for the size of the DP1 dataset. Smaller heliocentric distances were not attempted here because nearby objects move rapidly across the sky and hence were not likely to remain long enough in an LSSTComCam field to be discovered.

Candidate linkages, defined as groups of tracklets whose propagated orbits cluster within a radius of 1.33×10^3 au at 1 au, are identified, then postprocessed via `link_purify` to yield a final, nonoverlapping set of high-confidence asteroid candidates, ranked by orbit-fit residuals and related metrics. While heliolinx can produce false-positive or redundant raw linkages by design, these are filtered during post-processing by `link_purify`, which applies a Rubin-specific, more stringent version of the MPC validation rules¹⁰⁷. This step both rejects spurious linkages and deduplicates multiple hypotheses for the same object, ensuring that only the highest-quality, nonredundant linkages are carried forward for orbit determination and for distinguishing new discoveries from rediscoveries of known objects.

5. PERFORMANCE CHARACTERIZATION AND KNOWN ISSUES

In this section, we provide an assessment of the DP1 data quality and describe known issues.

5.1. Sensor Anomalies and Instrument Signature Removal

In addition to the known detector features identified before LSSTComCam commissioning, most of which are handled by the ISR processing (see §4.2.1), we discovered a number of new types of anomalies in the DP1 data. Since no corrections are currently available for these anomalies, they are masked and excluded from downstream data products.

5.1.1. Vampire Pixels

“Vampire” pixels are visible on the images as a bright defect surrounded by a region of depressed flux, as though the defect is stealing charge from its neighboring pixels. Figure 12 shows an example of a vampire pixel near the center of R22_S11 in an *r*-band flat.

From studies on evenly illuminated images, vampires appear to conserve charge. Unfortunately, no unique

optimum way exists to redistribute this stolen flux so, following visual inspection, a defect mask was created to exclude them from processing. We have found some similar features on the ITL detectors on LSSTCam, and will use the same approach to exclude them.

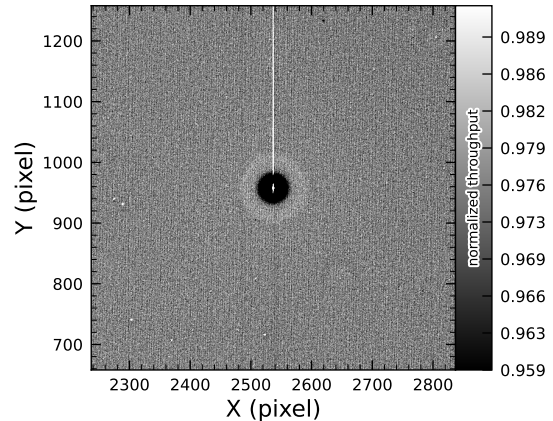


Figure 12. A large vampire pixel near the center of R22_S11, as seen in the *r*-band flat. This clearly shows the central hot vampire pixels, surrounded by a region of depressed signal, with a brighter ring surrounding that caused by local electric field effects. The charge contained in the central pixels is incompletely shifted as the image is read, and that charge leaks out into subsequent rows as it is shifted through the remnant charge. The columns that contain the hot pixels are masked as defects in all processing, as this feature cannot be otherwise corrected.

5.1.2. Phosphorescence

Some regions of the LSSTComCam CCD raft were seen to contain large numbers of bright defects. An example is shown in Figure 13 in a *g*-band flat. On further investigation, it appears that on some detectors a layer of photoresist wax was incompletely removed from the detector surface during production. As this wax is now trapped below the surface coatings, there is no way to physically clean these surfaces. If this wax responded to all wavelengths equally, then it would likely result in quantum efficiency dips, which might be removable during flat correction. However, it appears that this wax is slightly phosphorescent, with a decay time on the order of minutes, resulting in the brightness of these defects being dependent on the illumination of prior exposures. The worst of these regions was excluded with manual masks.

5.1.3. Cross Talk

Cross talk refers to unwanted signal interference between adjacent pixels or amplifiers. We use an aver-

¹⁰⁷ <https://minorplanetcenter.net/mpcops/documentation/identifications/additional/>

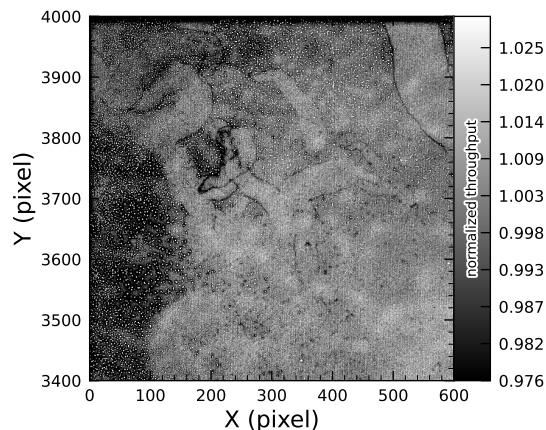


Figure 13. The top left corner of R22_S01 in the g band flat, showing the many small defect features that are caused by the remnant photoresist wax. A single large defect box masks this region from further analysis to prevent these features from contaminating measurements.

age interamp cross-talk correction based on laboratory measurements with LSSTCam. These average corrections proved satisfactory, and so have been used as is for DP1 processing. There are, however, some residual cross-talk features present postcorrection, with a tendency towards oversubtraction. Figure 14 shows an example of a bright star with oversubtracted cross-talk residuals visible on neighboring amplifiers to both sides on exposure 2024120600239, detector R22_S02.

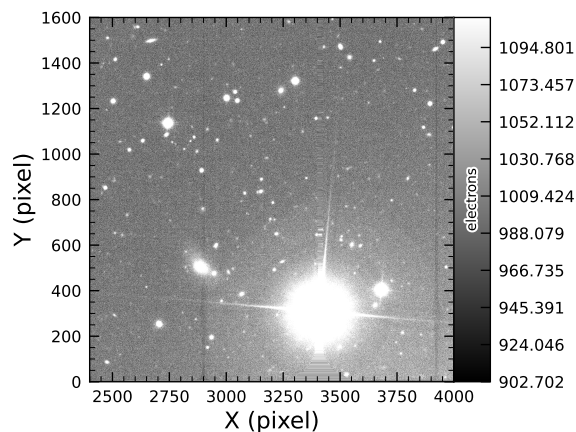


Figure 14. An example of a bright star with oversubtracted cross-talk residuals visible on neighboring amplifiers to both sides (exposure 2024120600239, detector R22_S02). The horizontal banding stretching from the center of the star shows the interpolation pattern covering the saturated core and the ITL edge bleed near the serial register.

5.1.4. Bleed Trails

Bleed trails are produced when charge from saturated pixels spills into adjacent pixels. Bleed trails were anticipated on LSSTComCam sensors, but they appear in more dramatic forms than had been expected. As a bleed trail nears the serial register, it fans out into a trumpet-shaped feature. Although bright, these features do not have consistently saturated pixels. In DP1 these “edge bleeds” were identified and masked.

Saturated sources can create a second type of bleed, where the central bleed drops below the background level. The depressed columns along these trails extend across the entire readout column of the detector, crossing the detector midline. We developed a model for these to identify which sources are sufficiently saturated to result in such a trail, which are then masked. As this kind of trail appears only on the ITL detectors, we have named these features “ITL dips”. Figure 15 shows an example of a bright star exhibiting the ITL dip phenomenon on exposure 2024121000503, detector R22_S21.

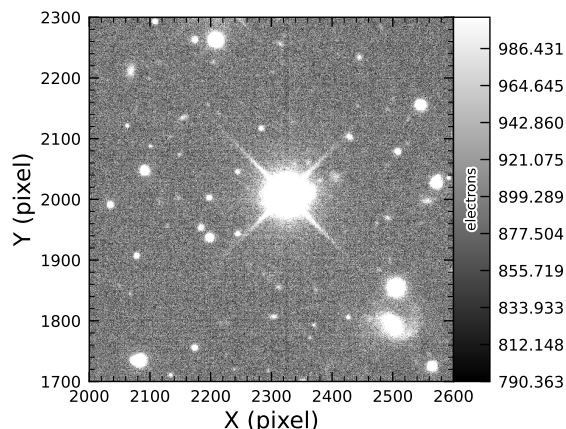


Figure 15. A bright star showing the ITL dip phenomenon, in which a dark trail extends out from the star to the top and bottom edges of the detector (exposure 2024121000503, detector R22_S21).

5.2. Point-spread Function Models

To characterize PSF performance, we use adaptive second moments (G. M. Bernstein & M. Jarvis 2002) measured on PSF stars and on the PSF model using the HSM implementation (C. Hirata & U. Seljak 2003; R. Mandelbaum et al. 2005). All measurements are expressed in the pixel coordinate frame of each detector. We characterize the performance of the PSF using the classical trace of the second moment matrix T , along

with the ellipticity parameters e^1 and e^2 . Measurements on the observed PSF stars are denoted as T_{PSF} , e_{PSF}^1 , e_{PSF}^2 , while those from PSF models are denoted as T_{model} , e_{model}^1 , e_{model}^2 . We compare two PSF modeling approaches:

- Piff with second-order polynomial interpolation (Piff O2), the pipeline’s default, and
- Piff with fourth-order polynomial interpolation (Piff O4), which serves as the final DP1 PSF model.

Table 5 summarizes each model’s ability to reconstruct the mean T , e^1 , and e^2 on LSSTComCam. Both models exhibit a negative residual bias in the reconstructed PSF size, with Piff O4 providing improved performance over Piff O2.

An alternative approach to evaluating the performance of the PSF model is to examine the average $\delta T/T$, where δT is $T_{\text{PSF}} - T_{\text{model}}$, across visits, projected onto focalplane coordinates, as shown in Figure 16. Piff reveals strong spatial correlations in the residuals, including a systematic offset consistent with the results presented in Table 5. The presence of these spatial structures motivated the adoption of fourth-order polynomial interpolation in all bands except u band. Although not shown in Figure 16, residual patterns persist even with third-order interpolation, indicating that it is insufficient to capture the complexity of the PSF variation. Increasing the interpolation order to five would nominally reduce the residuals further, but the limited number of stars available on some CCDs would not provide adequate constraints for such a model, while the resulting improvement would likely be minimal. Preliminary analysis of LSSTCam data in the laboratory at SLAC National Accelerator Laboratory (SLAC) shows that the ITL sensors exhibit the same pattern as ITL sensors on LSSTComCam.

Another way to look at the PSF modeling quality is via whisker plots of the PSF second and fourth moments and their modeling residuals projected on a part of the sky. In addition to the second moment, the spin-two fourth moments, $e^{(4)}$, are defined as

$$e_1^{(4)} = M_{40} - M_{04}$$

$$e_2^{(4)} = 2(M_{31} - M_{13}),$$

where M_{pq} are the standardized higher moments as defined in (T. Zhang et al. 2023) measured on stars and PSF models. Figure 17 shows the whisker plots of e , $e^{(4)}$ (top rows), and δe , $\delta e^{(4)}$ in the ECDFS field. The direction of a whisker represents the orientation of the shape, while the length represents the amplitude $|e|$ or

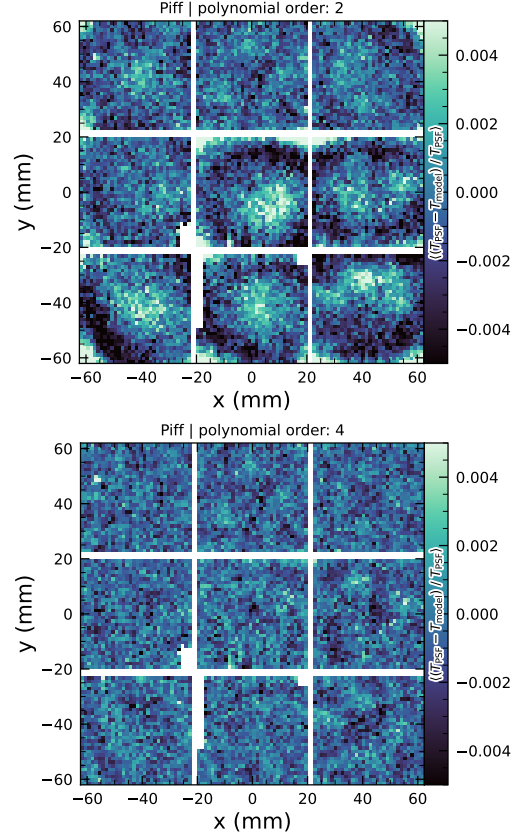


Figure 16. Average across all visits of $\delta T/T$ for Piff O2 and Piff O4 modeling on LSSTComCam. Averages are computed using a 120×120 binning.

$|e^{(4)}|$. We observe coherent patterns in both the PSF moments and the residuals, the latter of which warrant further investigation if they persist in future Data Releases.

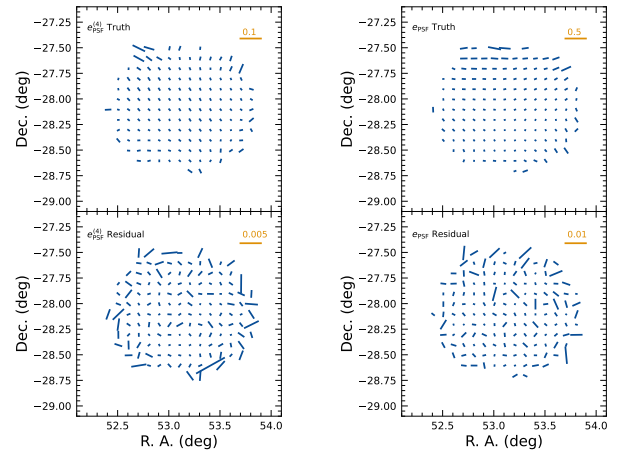
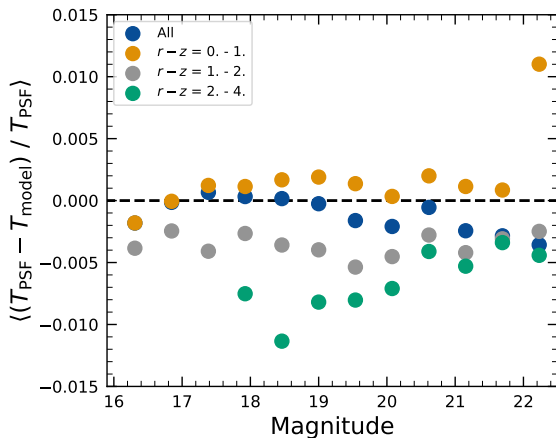


Figure 17. Whisker plots for the ECDFS field for e , $e^{(4)}$, δe , and $\delta e^{(4)}$.

Table 5. Observed mean values and comparison of model residuals, across all visits and filters

Quantity	Observed	Piff O2	Piff O4
		($\times 10^{-4}$)	($\times 10^{-4}$)
$\langle T \rangle$ (pixel ²)	11.366 ± 0.003		
$\langle e^1 \rangle$	$(-6.07 \pm 0.05) \times 10^{-3}$		
$\langle e^2 \rangle$	$(-4.57 \pm 0.05) \times 10^{-3}$		
$\langle e \rangle$	$(8.794 \pm 0.004) \times 10^{-2}$		
$\langle \delta T/T \rangle$		-4.0 ± 0.2	-5.0 ± 0.2
$\langle \delta e^1 \rangle$		0.6 ± 0.1	0.5 ± 0.1
$\langle \delta e^2 \rangle$		0.0 ± 0.1	0.0 ± 0.1

Figure 18 shows a plot of $\delta T/T$ vs. stellar magnitude, which can reveal any dependencies between PSF size and flux. We also repeat this analysis in color bins to probe chromatic effects. Binning by color uncovers a clear color dependence, as was also seen in DES (M. Jarvis et al. 2021b). The residuals are consistent with Table 5 and its cause is unknown. DP1 does not include the color correction implemented in the DES Year 6 analysis, (T. Schutt et al. 2025). This will be included in processing of future data releases.

**Figure 18.** Binned $\delta T/T$ as a function of magnitude across all visits and filters and in bins of stellar colors.

As noted in (Rubin Observatory Science Pipelines Developers 2025), two key Piff features were not used in the DP1 processing. PSF color dependence was not implemented, and, while Rubin software allows Piff to work with sky coordinates (including WCS transformations), it does not yet correct for sensor-induced astrometric distortions such as tree rings (H. Y. Park et al. 2017). Both features are planned for upcoming releases.

5.3. Astrometry

To characterize astrometric performance, we evaluate both internal consistency and agreement with an external reference. The primary measure of internal consistency is the repeatability of position measurements for the same object, defined as the RMS of the astrometric distance distribution for stellar pairs having a specified separation in arcminutes. We associate isolated point sources across visits and compute the rms of their fitted positions, rejecting any stars with another star within $2'$. Figure 19 shows the mean per-tract rms astrometric error in R.A. for all isolated point sources, both after the initial calibration and after the final calibration, which includes proper motion corrections. The results indicate that the astrometric solution is already very good after the initial calibration. Global calibration yields only modest improvement, likely due to the short time span of DP1 and the minimal distortions in LSSTComCam. In the main survey, the longer time baseline and greater distortions near the LSSTCam field edges will make global calibration more impactful. An additional measure of internal consistency is the repeatability of separations between objects at a given distance. To compute this, we identify pairs of objects that are separated by a specified distance and measure their precise separation during each visit in which both objects are observed. The scatter in these separation measurements provides an indication of the internal consistency of the astrometric model. Figure 20 shows the median separation for pairs of objects separated by approximately 5 (referred to as “AM1”), computed per tract after the final calibration. These values are already approaching the design requirement of 10 mas.

To assess external consistency, we consider the median separation between sources not included in the astrometric fit and associated objects from a reference catalog (§3.3.3). For this, we use the Gaia DR3 catalog, with the

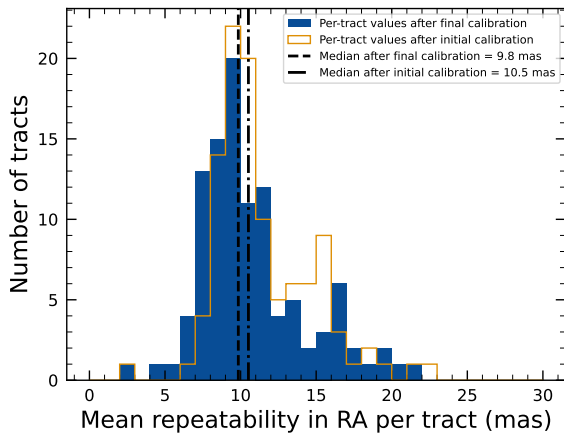


Figure 19. Mean per-tract astrometric repeatability of measurements of isolated point sources in R.A. in visits across all bands.

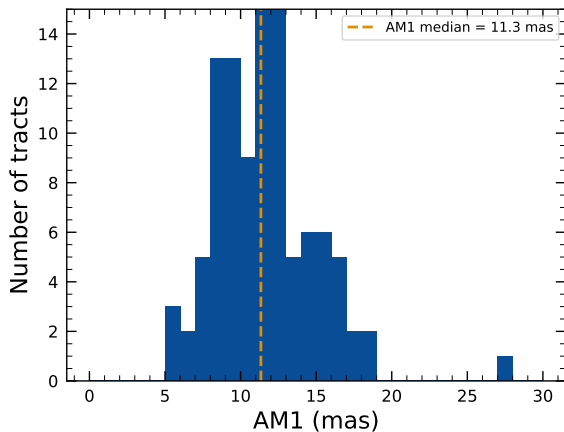


Figure 20. Median per-tract repeatability in separations between isolated point sources 5' apart (AM1) in visits across all bands.

object positions shifted to the observation epoch using the Gaia proper motion parameters. Figure 21 shows the median separation for each visit in the r band in tract 4849 in the ECDFS fields. The calculated values are almost all within 5 mas, well below the design requirement of 50 mas for the main survey. By examining the astrometric residuals, we can assess whether there are distortions not accounted for by the astrometric model. In some cases, residuals from a single visit exhibit behavior consistent with atmospheric turbulence, as shown in Figure 22, which is characterized by a curl-free gradient field in the two-point correlation function of the residuals (E mode; P. F. Léget et al. 2021); (W. F. Fortino et al. 2021). However, as seen in Figure 23, the residuals in many visits also have correlation functions with

a nonnegligible divergence-free B mode, indicating that some of the remaining residuals are due to unmodeled instrumental effects, such as rotations between visits.

We can see unmodeled camera distortions by stacking the astrometric residuals over many visits as a function of the focal plane position. Figure 24 shows the median residuals in x - and y - directions for 1792 visits. Spatial structures are evident at the CCD level, as well as at the midline break, the discontinuity between the two rows of amplifiers, in the y direction residuals. Further stacking all the detectors makes certain effects particularly clear. Figure 25 shows distortions very similar to those measured for an LSSTCam ITL sensor in a laboratory setting in (J. H. Esteves et al. 2023).

5.4. Differential Chromatic Refraction

DCR occurs when light passes through Earth's atmosphere, refracting more for shorter wavelengths, which causes blue light to appear shifted closer to the zenith. This wavelength-dependent effect results in the smearing of point sources along the zenith direction, specifically parallel to the parallactic angle. The DCR effect is observable in LSSTComCam data, particularly in the angular offset versus $g - i$ band magnitude difference plots, as shown in Figure 26. These plots include 228 visits selected to maximize the range of observed airmasses, which span 1.01–1.30 with a mean value of 1.13. When looking at data perpendicular to the parallactic angle, sources exhibit no discernible DCR effect, which is expected, and form a clear vertical distribution on the two-dimensional density plots in Figure 26.

In contrast, sources aligned with the parallactic angle exhibit a tilted, linear distribution, clearly demonstrating a relationship between angular offset and the $g - i$ magnitude difference, thereby providing a visual indication of the DCR effect. The DCR effect will be addressed in future releases.

5.5. Stellar Photometry

The photometric repeatability for isolated bright unresolved sources following the FGCM fits was excellent. For the 10% of unresolved sources withheld from the fit and having SNRs greater than 100, the photometric repeatability after applying chromatic correction was 7.1, 5.4, 5.4, 5.1, 5.9, and 6.5 mmag in the $ugrizy$ bands respectively, across all fields. After accounting for photometric noise, the intrinsic photometric repeatability was approximately 4.8, 2.7, 1.7, 1.0, 2.0, and 1.1 mmag in $ugrizy$. The DP1 processing does not yet include chromatic corrections in the final photometry. In this case the delivered photometric repeatability was 3–8 mmag for $grizy$.

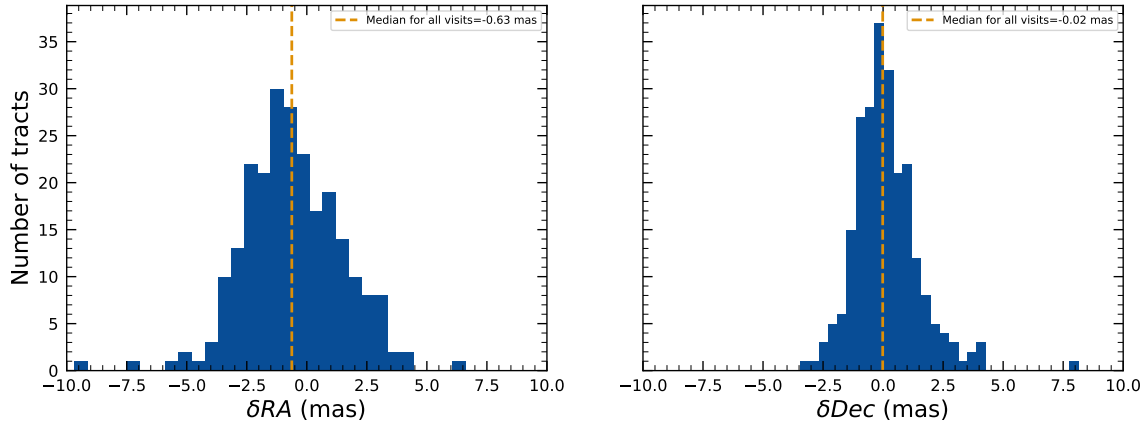


Figure 21. Median absolute offset for all visits in r band in [tract 4849](#) in the ECDFS field. The offset is the difference between the positions of isolated point sources that were reserved from the astrometric fit and matched objects from the Gaia DR3 catalog.

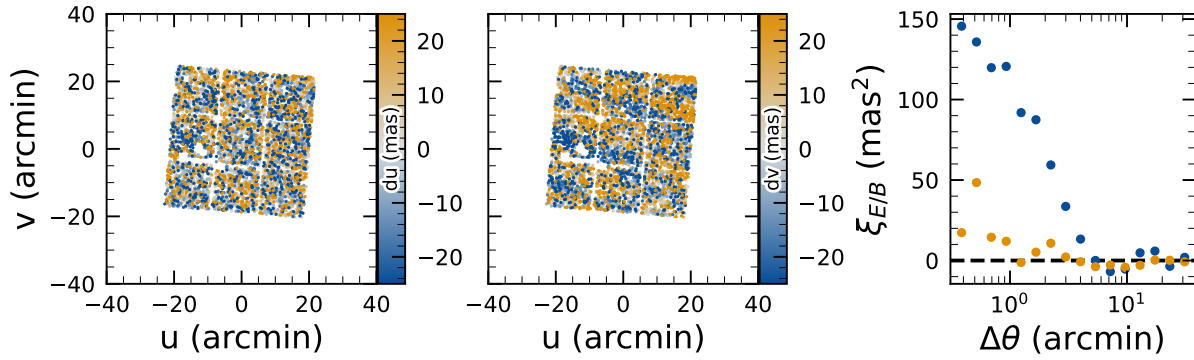


Figure 22. Astrometric residuals in u (left panel) and v (center panel) directions with the E (blue) and B (orange) modes of the two-point correlation function (right panel) seen in visit 2024120200359 in u band. The residuals show a wavelike pattern characteristic of atmospheric turbulence, and there is significant E mode and negligible B mode in the correlation function.

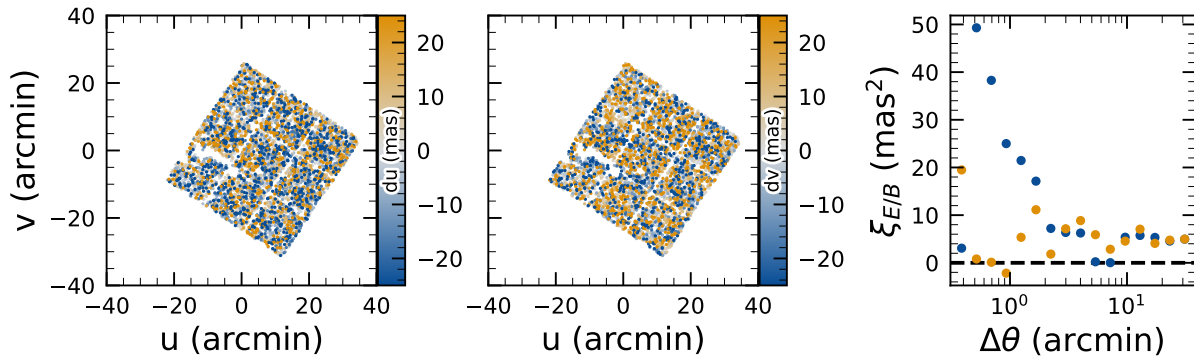


Figure 23. Astrometric residuals in u (left panel) and v (center panel) directions, with the E (blue) and B (orange) modes of the two-point correlation function (right panel) seen in visit 2024120700527 in u band. There are coherent residuals, but without the wave-like pattern seen in [Figure 22](#), and the correlation function has significant values for both E and B modes.

2221 In [Figure 27](#), we show the stellar loci in $ugriz$ for un- 2223 unresolved sources were selected using the extendedness
2222 resolved sources in the `DP1 Object` table (§3.2). These

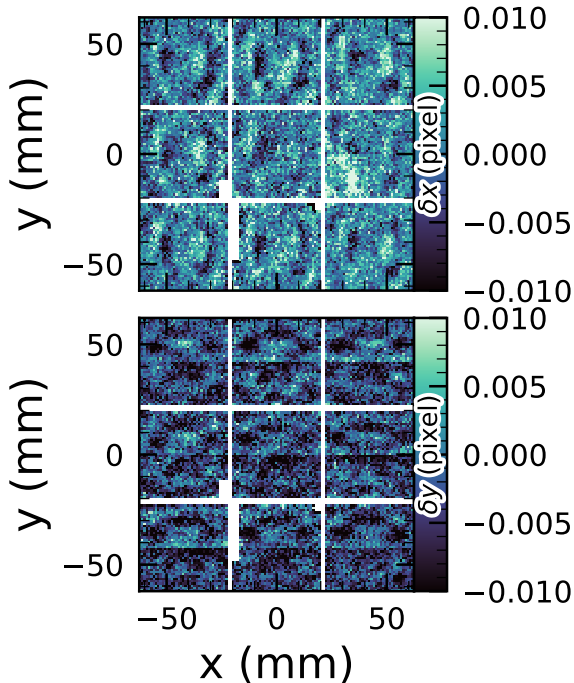


Figure 24. Median astrometric residuals as a function of focal plane position, shown in the left panel for the x -direction and in the right panel for the y -direction, for all nine *LSST-ComCam* CCDs independently. The range of the color scale is ± 0.01 pixels, corresponding to 2 mas, showing that the effect is small.

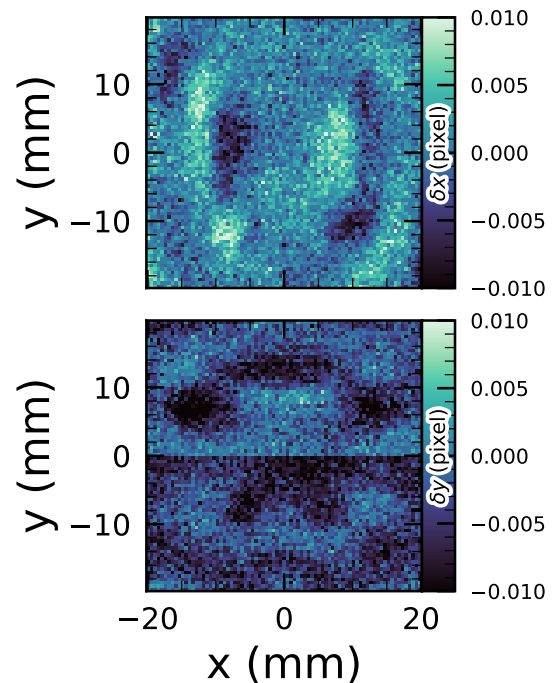


Figure 25. Median residuals as a function of pixel position, shown in the left panel for the x -direction and in the right panel for the y -direction. These residuals are aggregated across all nine CCDs that comprise the central *LSST-ComCam* raft. The range of the color scale is ± 0.01 pixels, corresponding to 2 mas, showing that the effect is small.

parameter (§3.2) in the `Object` catalog. This parameter is assigned a value of zero (unresolved) or one (resolved) in each band based on the difference between the PSF and CModel magnitudes. The extendedness is set to one when this magnitude difference exceeds 0.016 mag, as the PSF flux for extended sources is biased low relative to the CModel flux. This method has been previously employed by the SDSS pipelines, and its statistical properties, including the optimal combination of information from different bands and repeated measurements, are discussed in (C. T. Slater et al. 2020).

Figure 28 illustrates the behavior of the extendedness parameter. Its behavior in the g and r bands is similar, with unresolved sources scattered around the vertical line centered on zero. The width of the distribution increases toward fainter magnitudes. Resolved sources are found to the right and the dashed lines in the top panels show the adopted star–galaxy separation boundary. The morphology of the two color–magnitude diagrams in the bottom panels suggest that the unresolved sample suffers from increasing contamination by galaxies for $r > 24$. This behavior is consistent with simulation-based predictions from (C. T. Slater et al. 2020).

5.6. Detection Completeness on Coadds

We characterize completeness by injecting synthetic sources into coadded images, and by comparing source detections to external catalogs. In both cases, we use a greedy, probabilistic matching algorithm that matches reference objects, in order of descending brightness, to the most likely target within a $0''.5$ radius.

We inject sources in 12 of the patches of the ECDFS region with the deepest coverage. The input catalog contains stars and galaxies from part of the Data Challenge 2 (DC2) simulations (LSST Dark Energy Science Collaboration (LSST DESC) et al. 2021), where the galaxies consist of an exponential disk and a de Vaucouleurs bulge (G. de Vaucouleurs 1948, 1953). To avoid deblender failures from excessive increases in object density, stars with a total magnitude brighter than 17.5 mag (i.e., derived from flux summed across all six bands) are excluded, as are galaxies whose magnitude is brighter than 15 mag or fainter than 26.5 mag. One-half of the remaining objects are selected for injection. Afterward, individual bulge and disk components fainter than 29 mag are also excluded, both for computational expediency

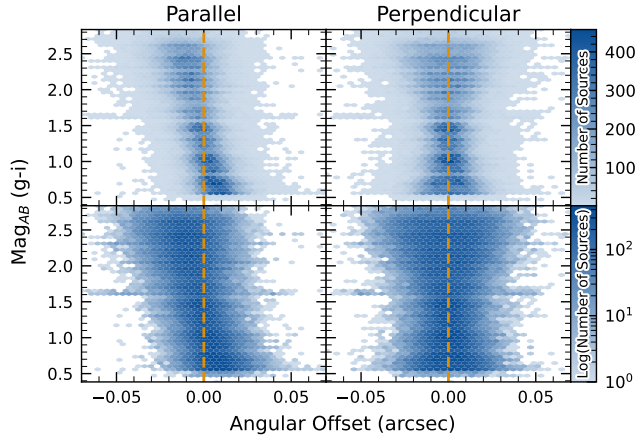


Figure 26. Visualization of DCR observed in the LSST-ComCam commissioning campaign. The $g - i$ color is computed for every source in the reference catalog (§3.3.3) that is matched to a direct source in the science image, and the binned density for the full survey is plotted against the angular offset between the reference and detected positions. The angular offset is projected along coordinates parallel and perpendicular to the parallactic angle of the observation, and shows a characteristic correlation along the parallel axis with no correlation along the perpendicular axis. The orange vertical dashed line indicates the expected $g - i$ distribution at zero angular offset.

and because their structural properties are less likely to be representative of real galaxies.

Figure 29 shows completeness as a function of magnitude for these injected objects in the ECDFS field. These completeness estimates are comparable to results from matching external catalogs. Matching to the Hubble Legacy Field catalog (G. Illingworth et al. 2016; K. E. Whitaker et al. 2019) reaches 50% completeness at $F775W = 26.13$, or about $i = 25.83$ from differences in matched object magnitudes. Similarly, completeness drops below 90% at $VIS = 23.80$ from matching to Euclid Q1 (Euclid Collaboration et al. 2025) objects, equivalent to roughly $i = 23.5$. The Euclid imaging is of comparable or shallower depth, so magnitude limits at lower completeness percentages than 90% are unreliable, whereas the Hubble Space Telescope (HST) images cover too small and irregular of an area to accurately characterize 80–90% completeness limits.

At the 80% completeness limit, nearly 20% of objects, primarily injected galaxies, are incorrectly classified as stars based on their reference band extendedness. Similarly, the fraction of correctly classified injected stars drops to about 50% at $i = 23.8$ (corresponding to 90% completeness).

This analysis has several caveats. The selection of objects for matching in any catalog is not trivial. Some fraction of the detections is spurious, particularly close to bright stars and their diffraction spikes. Additionally, some objects lie in masked regions of one survey but not another, which has not been accounted for. For injected source matching, the reference catalog (§3.3.3) does not include real on-sky objects. Based on prior analyses of the DC2 simulations, purity is generally greater than completeness at any given magnitude. Similarly, for bright ($i < 23$) objects classified as stars by reference-band extendedness, $< 5\%$ are either unmatched to a Euclid or HST object, or misclassified – that is, selecting on extendedness alone yields a fairly pure but incomplete sample of stars. We expect to remedy some of these shortcomings in future releases.

5.7. Model Flux and Shape Measurement

Figure 30 shows i -band magnitude residuals for CModel and Sérsic measurements using the matched injected galaxies described in §5.6. Similar behavior is seen in other bands. Sérsic fluxes show reduced scatter for galaxies with $i < 22.5$, though CModel fluxes are less biased, with median residuals closer to zero and less magnitude dependent. For fainter objects, the Sérsic fluxes are more biased and less accurate. The magnitude of this bias is considerably larger than previously seen in simulated data. Subsequent testing indicates that this bias can be (roughly) halved by fitting an exponential model first, and then using those parameters to initialize a free Sérsic fit. This approach will be adopted in future releases. Aperture fluxes, including Kron and GAaP, are not shown as they are not corrected to yield total fluxes. The correction for Kron fluxes can be derived from the Sérsic index (A. W. Graham & S. P. Driver 2005), but this correction is not provided in Object tables.

Figure 31 shows $g - i$ color residuals versus r -band magnitude for the same sample of galaxies as Figure 30. For this and most other colors, GAaP (with a $1''$ aperture) and Sérsic colors both yield lower scatter; however, the CModel colors have the smallest bias. Curiously, the GAaP bias appears to be magnitude dependent, whereas the Sérsic bias remains stable from $19 < r < 26$. Any of these color measurements is suitable for use for deriving quantities like photometric redshifts, stellar population parameters, etc.

In addition to photometry, some algorithms include measurements of structural parameters like size, ellipticity, and Sérsic index. One particular known issue is that many (truly) faint objects have significantly overestimated sizes and fluxes. This was also seen in the DES (K. Bechtol et al. 2026), who dubbed such

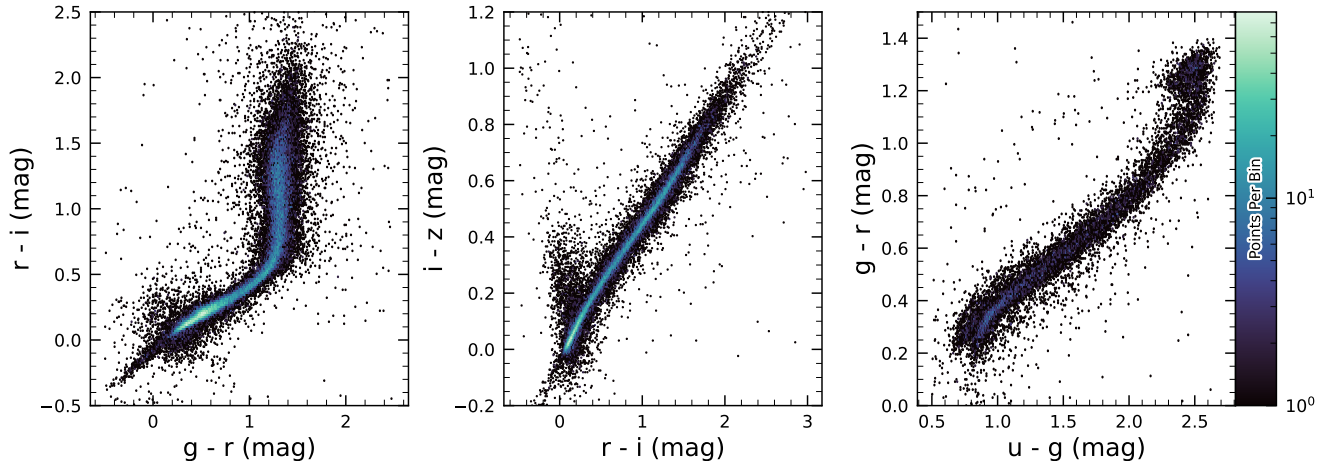


Figure 27. Examples of stellar loci for unresolved sources from the DP1 dataset. From left to right: *gri* stellar locus containing 63,236 stars with SNR > 200 in the *i* band; *riz* stellar locus containing 46,760 stars with SNR > 200 in the *i* band; and *ugr* stellar locus containing 12,779 stars with SNR > 50 in the *u* band.

2346 objects “super-spreaders”. These super-spreaders contribute significantly to overestimated fluxes at the faint end (see e.g. Figure 30), and are particularly problematic for the Kron algorithm (R. G. Kron 1980), which should only be used with caution.

2351 As mentioned in §4.5, the Sérsic fits include a free centroid, which is initialized from the fiducial centroid of the object. Preliminary analyses of matched injected objects suggest that the Sérsic model galaxy astrometry residuals are somewhat smaller than for the standard centroids used in other measurements, and so users of the Sérsic photometry should also use these centroid values. One caveat is that for faint objects and/or in crowded regions with unreliable deblending, free centroids can drift significantly and potentially toward other objects, so objects with large differences between the fiducial and Sérsic astrometry should be discarded or used with caution.

2364 Sérsic model parameter uncertainties are estimated by computing and inverting the Hessian matrix with the best-fit parameter values, after replacing the pixel data (but not uncertainties) by the best-fit model values. Currently, only the on-diagonal dispersion term (square root of the variance) is provided as an error estimate for each parameter. Future releases may provide more off-diagonal terms of the covariance matrix, particularly for the structural parameters, which are known to be correlated.

2374 A major outstanding issue is that many parameter uncertainties, including but not limited to those for fluxes, are underestimated. This is at least partly (but not wholly) due to the fact that coaddition introduces co-

2378 variance between pixels, which is not captured in per-pixel variances.

2381 The degree to which uncertainties are underestimated can depend on the parameter in question and on the brightness of the object. In plots of uncertainty-scaled residuals, the ideal behavior is for the median (i.e. the bias) to lie close to zero, and for the $\pm 1\sigma$ lines to lie at ± 1 , without any dependence on magnitude. Figure 32 shows that flux and color uncertainties for PSF model magnitudes of injected stars are both underestimated, but by a factor of approximately 1.7 – 2 that is not very sensitive to SNR. This holds for the astrometric and centroid parameters as well.

2391 In turn, Figure 33 shows that CModel color uncertainties of galaxies are underestimated by a similar factor at the faint end, but with appreciable scaling with magnitude (and thereby SNR). Flux error underestimation is both larger than for colors and scales more strongly with SNR. This indicates that systematic effects dominate the errors in fluxes, particularly for bright galaxies. This is also at least partly but not wholly due to so-called model inadequacy, that is, the fact that galaxy models, parameteric or otherwise, are insufficiently complex to capture the structure of real galaxies.

2403 Figure 34 shows that the Sérsic model fluxes and colors have similar behavior as for CModel, but with a greater degree of overestimation. This may be partly due to the fact that the Sérsic parameter uncertainties are estimated along with the free centroid and structural (shape and Sérsic index) parameters, whereas the forced CModel fluxes and errors are derived from linear flux fits with a fixed shape and centroid.

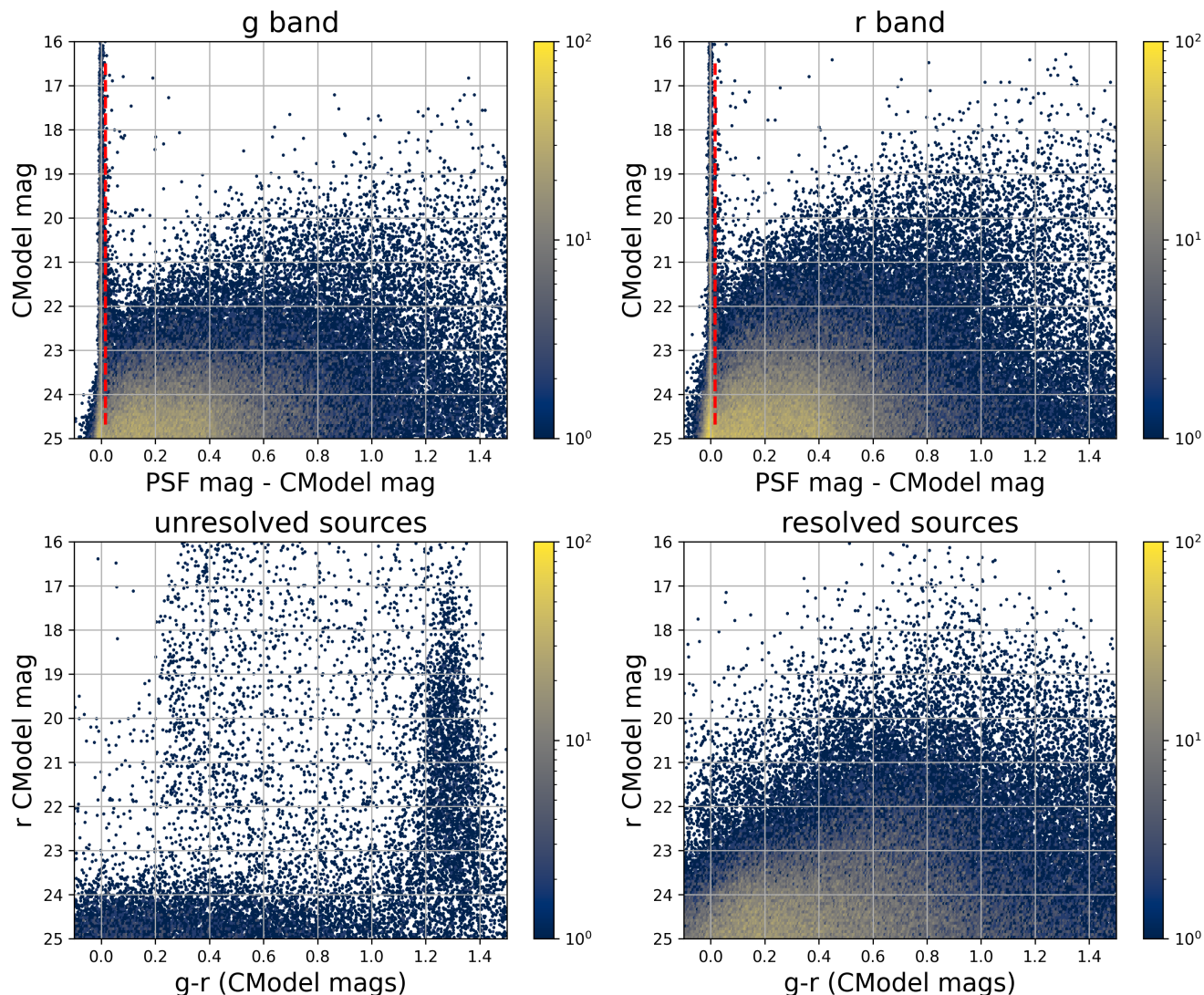


Figure 28. The top two panels shows the difference between the PSF and CModel magnitudes as a function of CModel magnitude in the g and r bands for 178,547 sources with $CModel_r < 25$ from the ECDFS field. The vertical dashed line in each panel marks the minimum value (0.016 mag) for setting the extendedness parameter to one. The bottom two panels show r vs. $g - r$ color-magnitude diagrams for 14,701 unresolved (left) and 163,666 resolved (right) sources. Note the unresolved sample suffers from increasing contamination by galaxies for $r > 24$.

2410 Efforts are underway to investigate and quantify the
 2411 origin of the uncertainty underestimates and future re-
 2412 leases will, at the least, provide recommendations for
 2413 mitigations.

2414 5.8. Difference Imaging

2415 We assessed the performance of image differencing us-
 2416 ing both human vetting (§5.8.1) and source injection
 2417 (§5.8.2).

2418 5.8.1. Difference-imaging Purity

2419 Members of the DP1 team labeled more than 11,000
 2420 DIASource image triplets, each consisting of cutouts
 2421 from the science, template, and difference images. An

2422 internal labeling service (*tasso*) was deployed within
 2423 the USDF environment. A random subset of approxi-
 2424 mately 16,000 DIASources was selected and uploaded to
 2425 the service, which remained active for roughly 3 months
 2426 and labeled by members of the DP1 team. Users la-
 2427 beled DIASource PNG images triplets, each consisting
 2428 of cutouts from the science, template, and difference
 2429 images. Each stamp had dimensions of 51×51 pixels,
 2430 matching the input size required by the machine learn-
 2431 ing model. Access to the labeling service was granted
 2432 to all individuals with commissioning data access. Each
 2433 DIASource was classified exactly once, with a total of
 2434 35 volunteers contributing labels. Figure 35 show an ex-

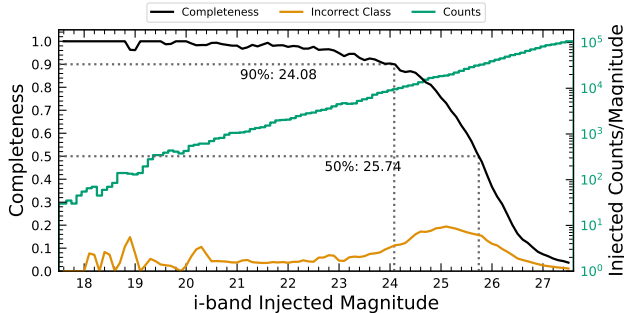


Figure 29. Completeness and incorrect classification fraction as a function of i -band CModel magnitude (reference magnitude) for DC2-based injected objects into a portion of the ECDFS field. The “Incorrect Class” line shows the proportion of objects that are matched but classified incorrectly by their reference-band extendedness, i.e. stars with an extendedness of one or galaxies with extendedness of zero in the reference band.

2435 ample of one of the image triplets consisting of cutouts
 2436 from the science, template, and difference images that
 2437 volunteers were asked to label.

2439 The labeled sources were classified into multiple cat-
 2440 egories representing real astrophysical events and arti-
 2441 facts. Prior to any filtering, the raw artifact-to-real ratio
 2442 was approximately 9:1. Bright stars were identified as
 2443 the dominant source of artifacts, while correlated noise,
 2444 particularly in the u and g bands, also produced spuri-
 2445 ous detections near the flux threshold. We expect to be
 2446 able to mitigate these effects in future LSSTCam data.

2447 Applying a reliability threshold based on the machine
 2448 learning reliability model described in §4.6.1 improved
 2449 the purity of transient detections but had limited im-
 2450 pact on variable stars. This limitation arises from tech-
 2451 nical constraints at the time of model training, which
 2452 prevented the injection of variable stars into the syn-
 2453 thetic training set. Future reliability models for LSST-
 2454 Cam data, described in §4.6.1, will be trained using a
 2455 broader and more representative range of input data.

2456 The performance of the reliability model on the test
 2457 data (§4.6.1) is shown in Figure 36. The rate of true
 2458 positives and false negatives obtained by thresholding
 2459 the reliability score at 0.5 is reported for transients (99
 2460 stamps), and variable stars (316 stamps) vetted in `tasso`
 2461 in Table 6. Additionally we crossmatched stamps
 2462 with solar system objects with known orbits retrieving
 2463 5,988 solar system objects stamps.

2466 5.8.2. Difference-imaging Detection Completeness

2467 We assess the performance of our difference-imaging
 2468 pipeline using synthetic source injection on the science
 2469 images prior to differencing. We construct a catalog of
 2470 injected sources by joining two different samples of point

Table 6. The rate of true positives (TP) and false negatives (FN) obtained by thresholding the reliability score at 0.5 for Solar system objects, transients and variable stars.

Object Type	Number	TP Rate	FN Rate
Solar System	5,988	93.5%	6.5%
Transients	99	73.7%	26.3%
Variables	316	3.5%	96.5%

2471 sources, a set of hosted sources to emulate transients in
 2472 galaxies and second set of hostless sources. The hosts
 2473 are selected from the pipeline source catalog that is pro-
 2474 duced upstream by imposing a cut on their extendedness
 2475 measurement and selecting $N_{\text{src}} = \min(100, N \times 0.05)$ of
 2476 the N available sources per detector. For each host we
 2477 pick a random position angle and radius using its light
 2478 profile shape to decide where to place the source, and
 2479 also a random value of brightness for the injected source,
 2480 with magnitudes higher than the host source.

2481 The hostless sources instead have random positions
 2482 in the CCD focal plane, and magnitudes chosen from a
 2483 random uniform distribution with $20 \geq m \geq m_{\text{lim}} + 1$,
 2484 where m_{lim} is the limiting magnitude of the image. We
 2485 used the LSST `source_injection` package¹⁰⁸ to include
 2486 these sources in our test images. We performed a coordi-
 2487 nate cross-match task, with a threshold of 0.5 to find
 2488 which of these sources were detected and which were
 2489 lost, enabling the calculation of a set of performance
 2490 metrics.

2491 In Figure 37 we show the detection completeness as a
 2492 function of SNR, for sources in the ECDFS field, for
 2493 filters $griz$. We observe a completeness $> 95\%$ for
 2494 sources with $\text{SNR} > 6$, with mean completeness $\simeq 99\%$
 2495 and standard deviation of $\simeq 0.7\%$. In Figure 38 we
 2496 show the distribution of the residuals of the recovered
 2497 sky coordinates for the detected synthetic sources. The
 2498 marginal distributions are both centered at zero, and
 2499 for sources of $\text{SNR} > 20$ the residuals are compatible
 2500 with a normal distribution $\mathcal{N}(\mu = 0, \sigma^2 = (0''.02)^2)$.
 2501 In Figure 39 we show photometry results for our de-
 2502 tected synthetic sources in the i filter, using PSF pho-
 2503 tometry on the difference images. We include both the
 2504 magnitude residuals as well as the flux pulls, defined as
 2505 $(f_{\text{PSF}} - f_{\text{True}})/\sigma_{f_{\text{PSF}}}$, where f_{True} is the true flux,
 2506 f_{PSF} is the PSF flux and $\sigma_{f_{\text{PSF}}}$ is its uncertainty, as a
 2507 function of the true magnitude of the synthetic sources, in-
 2508 cluding

¹⁰⁸ <https://pipelines.lsst.io/modules/lsst.source.injection/index.html>

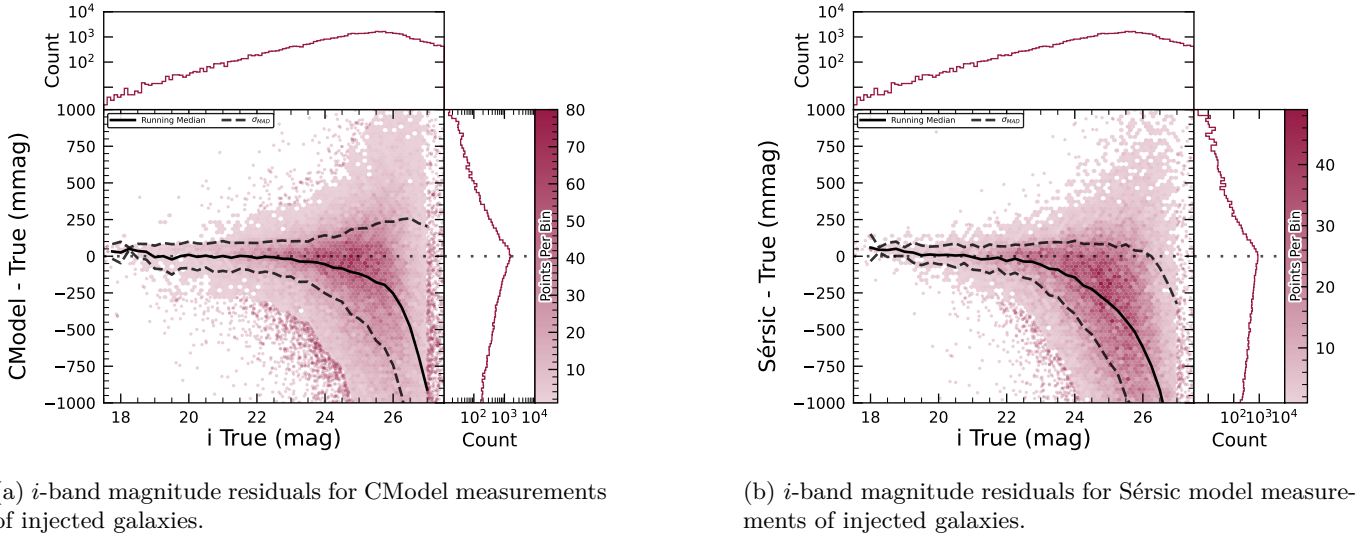


Figure 30. i -band magnitude residuals for matched injected DC2 galaxies with the CModel and Sérsic algorithms in a portion of the ECDFS region, including the median and scatter thereof. The black line is the median.

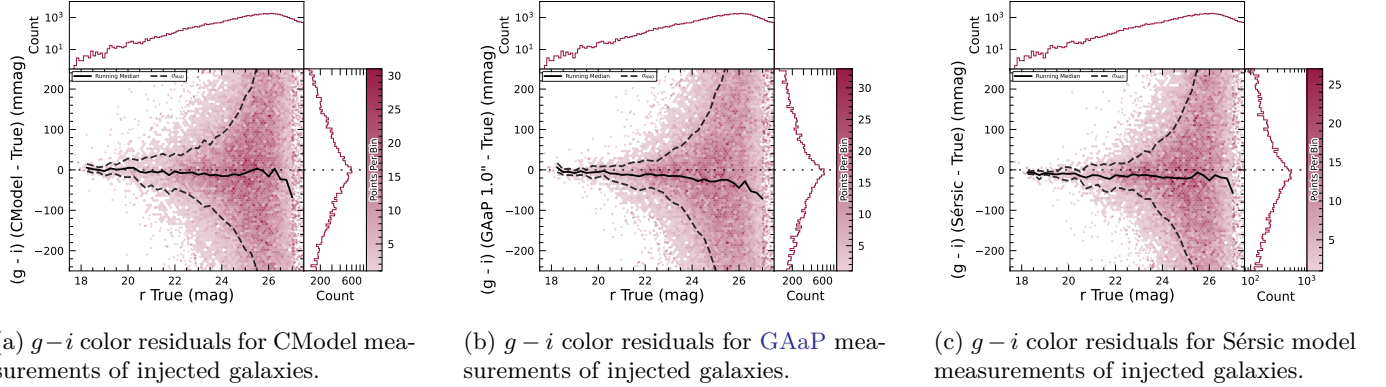


Figure 31. $g-i$ color residuals versus true r -band magnitude for matched injected DC2 galaxies with the CModel, GAaP and Sérsic algorithms in a portion of the ECDFS region.

2510 ing the running median and median absolute deviation
 2511 (MAD) for the whole brightness range. We also include
 2512 the true magnitude distribution as well as the detec-
 2513 tion completeness in the top panel, and for reference the
 2514 90% and 50% completeness magnitude values as vertical
 2515 lines. In the right panels we include the marginal
 2516 distribution for sources brighter than 22.5 mag, splitting
 2517 the data into hosted and hostless, as well as the robust
 2518 mean and standard deviation. From this figure we can
 2519 see that our flux measurements are accurate within a
 2520 wide range of magnitudes, for both hosted and hostless
 2521 synthetic sources. We find that the median offset is be-
 2522 low 0.002 mag for true magnitudes below 21, and with
 2523 a maximum σ_{MAD} scatter of about 0.02 mag in this
 2524 range. For true $m_i < 22.5$, the robust running median
 2525 PSF magnitude residuals are < 0.02 mag, and when
 2526 splitting into hosted and hostless both robust medians
 2527 are well below 0.01, and robust σ values, i.e. σ_{MAD} are

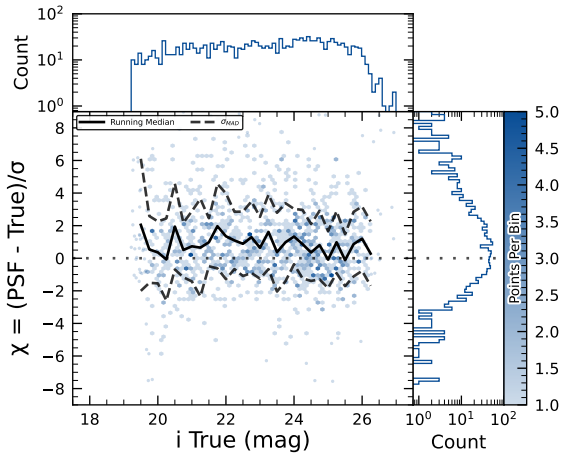
2528 also well below 0.05. For all sources with $m_i < 21.5$
 2529 the running median is always $|\langle \delta \rangle| < 0.1$, and MAD
 2530 $\sigma_\delta < 1$. Extending to sources with $m_i < 22.5$, hostless
 2531 sources have a robust mean pull below 0.02, with a ro-
 2532 bust standard deviation < 1.15 , while these parameters
 2533 increase to 0.2 and 1.2 for hosted sources, respectively,
 2534 suggesting that we might have contamination from host
 2536 background sources potentially biasing our fluxes.

5.9. Solar System

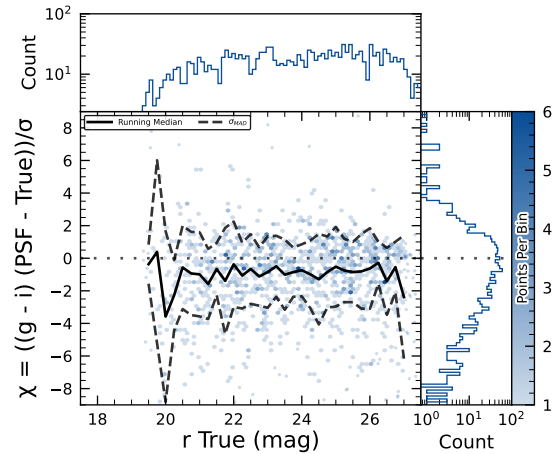
5.9.1. Asteroid Linking Performance

2539 The evaluation of asteroid linking performance in DP1
 2540 focused on demonstrating discovery capability. The solar
 2541 system discovery pipeline produced 269,581 track-
 2542 lets, 5,691 linkages, and 281 postprocessed candidates.

2543 As described in §4.6.3, postprocessing of the heli-
 2544 olinc output with `link_purify` produced a final set of
 2545 281 candidate linkages, ranked with the most promising

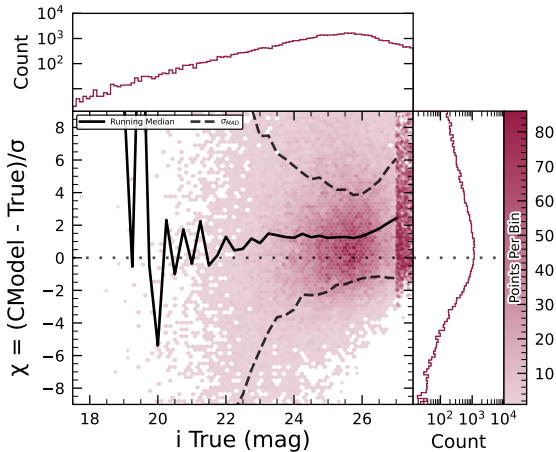


(a) i -band flux uncertainty-scaled residuals for PSF model measurements of injected stars.

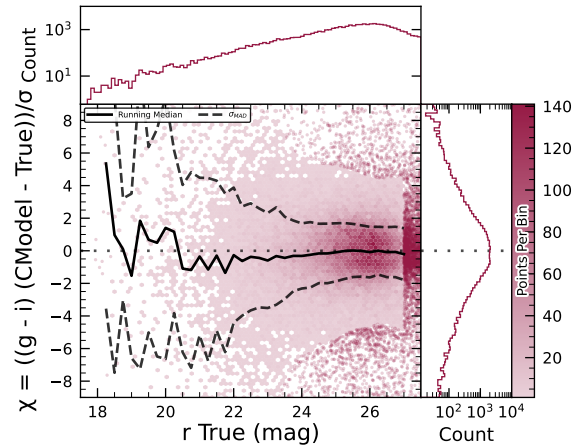


(b) $g - i$ color uncertainty-scaled residuals for PSF model measurements of injected stars.

Figure 32. Color and flux uncertainty-scaled residuals for matched injected DC2 star PSF model measurements in a portion of the ECDFS region.



(a) i -band flux uncertainty-scaled residuals for CModel measurements of injected galaxies.

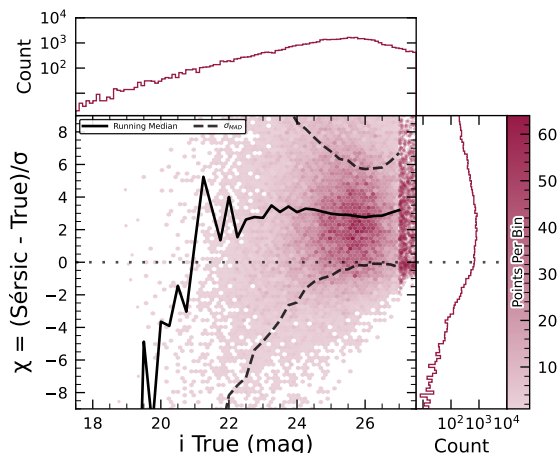


(b) $g - i$ color uncertainty-scaled residuals for CModel measurements of injected galaxies.

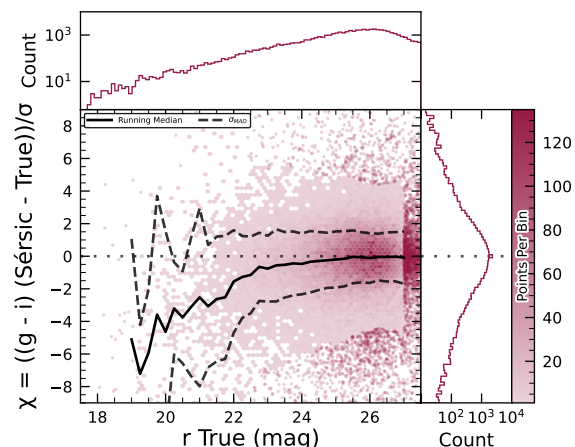
Figure 33. Color and flux uncertainty-scaled residuals for matched injected DC2 galaxy CModel measurements in a portion of the ECDFS region.

2546 first. We then used `find_orb` (B. Gray 2025) to derive
 2547 orbit fits for each candidate, sorting the resulting list by
 2548 χ_{dof}^2 , a measure of fit quality. A conservative manual
 2549 investigation of these candidates yielded a curated list
 2550 of 93 probable new asteroid discoveries. Manual inspec-
 2551 tion of the linkages indicated that those ranked 0–137
 2552 corresponded to unique real asteroids; ranks 138–200
 2553 contained additional real objects intermixed with some
 2554 spurious linkages; and ranks higher than 200 were essen-
 2555 tially all spurious. This analysis indicates that it will be
 2556 possible to identify cuts on quality metrics such as χ^2
 2557 to define discovery candidate samples with high purity;
 2558 determining the exact quantitative cut values requires
 2559 more data with LSSTCam. We next removed all obser-

2560 vations matched to known asteroids (using the MPC's
 2561 MPChecker service), reducing the number of candidates
 2562 to 97. Of these, four had strong astrometric and/or
 2563 photometric outliers, likely due to self-subtraction in
 2564 difference images due to the unavoidable limitations of
 2565 template generation from the limited quantity of data
 2566 available from LSSTComCam. We suspect these four
 2567 linkages do correspond to real objects, but have chosen
 2568 to discard them out of an abundance of caution. The re-
 2569 maining 93 were submitted to the MPC and accepted as
 2570 discoveries, demonstrating the LSST pipelines are able
 2571 to successfully discover new solar system objects.



(a) i -band flux uncertainty-scaled residuals for Sérsic model measurements of injected galaxies.



(b) $g-i$ color uncertainty-scaled residuals for Sérsic model measurements of injected galaxies.

Figure 34. Color and flux uncertainty-scaled residuals for matched injected DC2 galaxy Sérsic measurements in a portion of the ECDFS region.

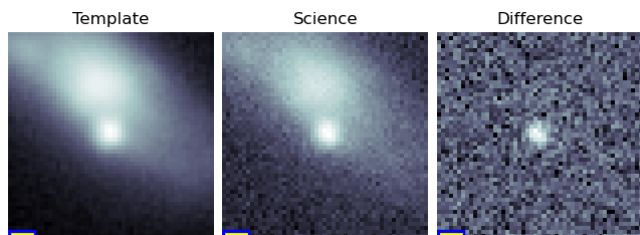


Figure 35. An example an image triplet consisting of cutouts showing, from left to right, the template, science, and difference images that volunteers were asked to label.

5.9.2. Asteroid Association Performance

2572

2573 During the solar system association step, 5988 Dia-
 2574 aSources were linked to 431 unique solar system ob-
 2575 jects, These include 3934 DiaSources with 338 pre-
 2576 viously known objects cataloged by the MPC, and 2054
 2577 DiaSources with the 93 newly discovered objects, all of
 2578 which are main belt asteroids. An additional 143 de-
 2579 tections of these newly discovered objects were also re-
 2580 covered. These detections were not initially identified
 2581 by the discovery pipelines, as they did not meet the
 2582 required criteria for tracklet formation, specifically the
 2583 minimum number of detections and/or the maximum
 2584 allowed time span between observations.

2585 The astrometric residuals of known asteroid associa-
 2586 tions are shown in Figure 40. The astrometric precision
 2587 for solar system sources is excellent, with the majority of
 2588 objects detected within $0''.1$ of their expected positions.

2589 By analyzing the signed median residuals to search for
 2590 biases, we find that previously-known objects have mean
 2591 residuals of $0''.001$ and $-0''.016$ in the RA and Dec di-
 2592 rections respectively, whereas newly-discovered objects
 2593 have mean residuals of $-0''.035$ and $-0''.010$ in the RA

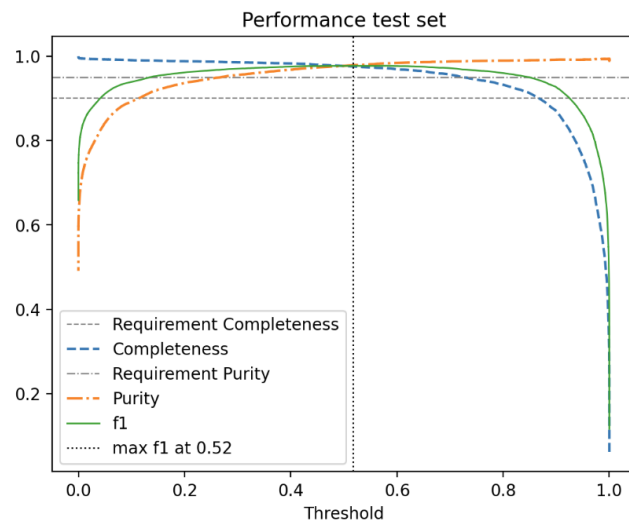


Figure 36. The purity and completeness of the reliability score is shown as a function of reliability threshold based on the testing data. A vertical line marks the threshold where the highest F1-score is obtained. The F1 score is the harmonic mean of completeness and purity. See §4.6.1 for details on the model and model training.

2594 and Dec directions, respectively. These mean residuals
 2595 are small enough to eliminate the possibility of a tim-
 2596 ing offset greater than the second-scale shutter motion,
 2597 which is consistent with the timing studies presented in
 2598 §2.2.2.

2599 The wider scatter in the RA residuals is due to ob-
 2600 jects whose measured orbital elements are less well con-
 2601 strained, translating to larger along-track positional er-
 2602 rors in the predicted positions Observations of objects
 2603 with large residuals are the most valuable ones from the
 2604 point of view of improving the orbit, which is why we

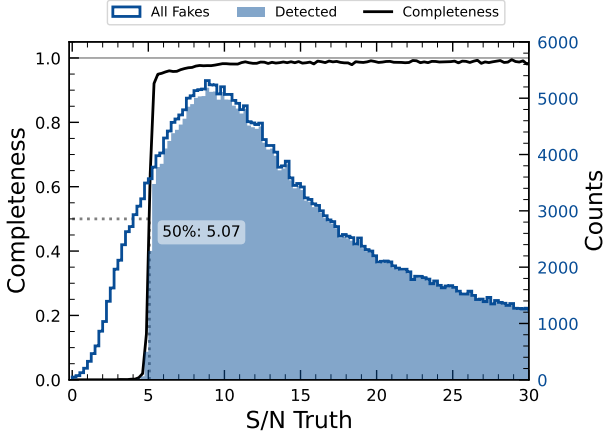


Figure 37. The difference image detection completeness for injected sources in the ECDFS field, for filters *griz*, as a function of the estimated SNR. This completeness is the ratio between the found fake sources (shaded histogram) and all the sources (solid line). The horizontal dashed line represents where the 50% completeness level is reached, at approximately $\text{SNR} \simeq 5.07$.

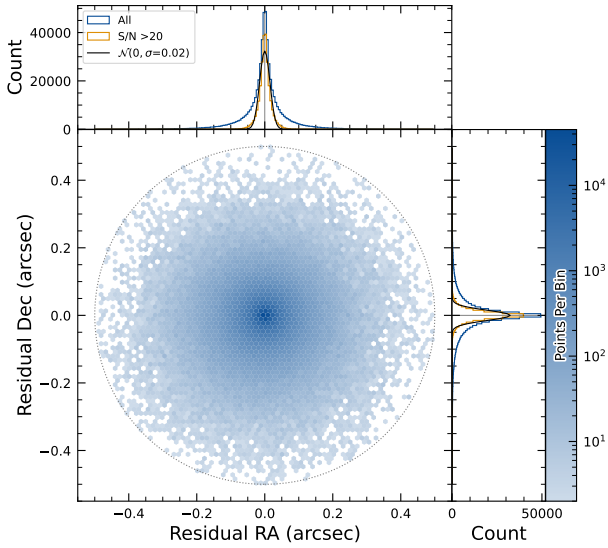


Figure 38. Coordinate residuals for detected synthetic sources in difference images, between the recovered and true positions of sources in the ECDFS field. In the top and right panels we include the distribution of these offsets, for all sources as well as for sources with $\text{SNR} > 20$. These high SNR sources show a Gaussian coordinate residual distribution with $\sigma = 0''.02$ (black solid lines). The circle reflects the matching radius of $0''.5$.

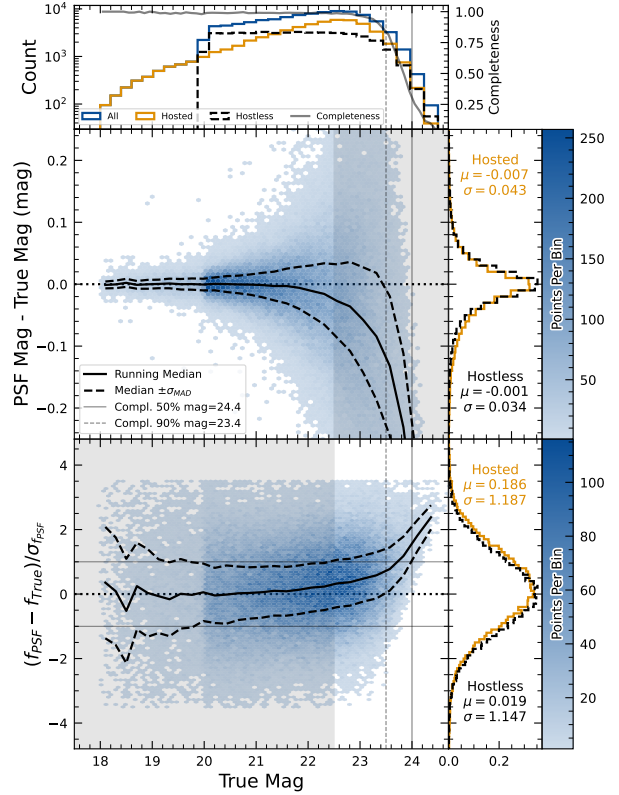


Figure 39. Magnitude residuals and flux pulls for *i*-band PSF photometry on difference images for the ECDFS field in *i* for detected injected sources. Top panel: distribution of true magnitudes for injected sources (blue), and split into hostless (black dash) and hosted (orange) sources, with detection completeness as a function of true magnitude (gray line). Vertical dashed lines indicate the 90% and 50% completeness magnitude limits. Center left panel: two-dimensional hexbin plot of PSF magnitude residuals (measured minus true) vs. true magnitude for detected sources, with the running median (solid black) and σ_{MAD} (dashed black) overlaid. Center right panel: marginalized distributions of PSF magnitude residuals for hostless (blue) and hosted (orange) sources with true magnitude $m_i < 22.5$, annotated with the robust mean and standard deviation. Bottom left panel: two-dimensional hexbin plot of PSF flux pulls vs. true magnitude for detected sources, with the running median (solid black) and σ_{MAD} (dashed black) overlaid. Bottom right panel: marginalized distributions of PSF flux pulls for hostless (blue) and hosted (orange) sources with true magnitude $m_i < 22.5$, annotated with robust mean and standard deviation.

2605 kept a generous matching radius. However, in future re-
 2606 leases we are likely to couple this with either orbit fitting

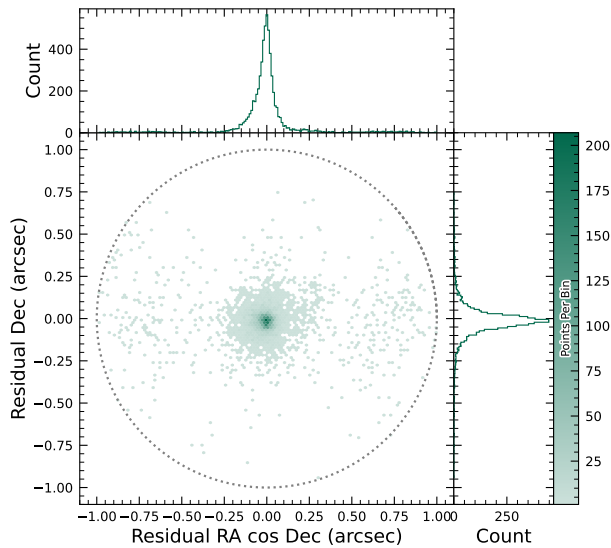


Figure 40. Astrometric residuals between expected and observed positions of solar system objects in DP1. The median residuals are $0''.001$ and $-0''.016$ in R.A. and decl. directions, with standard deviations of $0''.19$ and $0''.10$, respectively. No detectable systematic offset from zero indicates there are no major errors in either timing or astrometry delivered by the Rubin system. The wider scatter in the R.A. direction is due to objects whose measured orbital elements are less well constrained, translating to larger along-track positional errors in the predicted positions.

to verify the “singleton” match, or require two near-in-time observations (a tracklet) that match the expected motion vector as well.

Optimal moving source attribution is an area of active work that we expect to fully converge in time of Data Release 1 (DR1). In the meantime, for DP1 we have opted to start with simple, more easily understandable, criteria.

5.10. Crowded Fields

Among the seven Rubin DP1 target fields, two stand out for their severe stellar crowding: the globular cluster 47 Tucanae (47 Tuc) and the Fornax dwarf spheroidal galaxy (Fornax dSph). These fields were selected in part to stress test the LSST Science Pipelines under high-density conditions. While both exhibit high stellar densities, the nature and spatial extent of the crowding differ significantly.

47 Tuc presents extreme crowding across much of the field, encompassing its dense core and the eastern regions influenced by the Small Magellanic Cloud (SMC). This pervasive crowding leads to persistent challenges for deblending and reliable source detection, ex-

posing field-wide limitations in the current pipeline performance (Y. Choi et al. 2025). In contrast, Fornax dSph shows significant crowding only in its central region, with outer areas remaining well resolved and easier to process.

In both 47 Tuc and Fornax dSph, extreme crowding led to the deblending step being skipped frequently when memory or run-time limits were exceeded, typically due to an excessive number of peaks, or large parent footprints. However, the impact of these limitations differed: in 47 Tuc, deblending was often skipped across the entire field, resulting in large gaps and substantially reduced completeness. In Fornax dSph, these issues were largely confined to the central region, with much better recovery in the outskirts. This contrast highlights how the pipeline’s limitations depend on the spatial extent of high-density regions: 47 Tuc exposed systematic, field-wide challenges, whereas Fornax dSph revealed more localized, density-driven limits.

(T. M. Wainer et al. 2025) explored the Rubin DP1 DiaObject catalog (§3.2) in the 47 Tuc field, which contains sources detected in difference images. Because forced photometry is performed at these positions across all single-epoch images, this dataset bypasses the coadd-based detection and deblending stages that often fail in crowded regions. By computing the median of the forced photometry for each DiaObject across available visits, they recovered approximately 3 times more candidate cluster members than found in the standard Object table (Y. Choi et al. 2025). This result underscores the value of difference-imaging-based catalogs for probing dense stellar regions inaccessible to standard coadd processing in DP1.

Although the DP1 pipeline was not optimized for crowded-field photometry, these early studies of 47 Tuc and Fornax dSph provide critical benchmarks. They highlight both the limitations and opportunities for science with Rubin data in crowded environments, and they inform future pipeline development aimed at robust source recovery in complex stellar fields.

6. RUBIN SCIENCE PLATFORM

The RSP (M. Jurić et al. 2019) is a powerful, cloud-based environment for scientific research and analysis of peta-scale astronomical survey data. It serves as the primary interface for scientists to access, visualize, and conduct next-to-the-data analysis of Rubin and LSST data. The RSP is designed around a “bring the compute to the data” principle, eliminating the need for users to download massive datasets. Although DP1 is much smaller in size (3.5 TB) than many current survey datasets, future LSST datasets will be far larger and

more complex, making it crucial to colocate data and analysis for effective scientific discovery.

The RSP provides users with access to data and services through three distinct user-facing Aspects: a *Portal*, which facilitates interactive exploration of the data; a JupyterLab-based *Notebook* environment for data analysis using Python; and an extensive set of *Application Programming Interfaces (APIs)* that enable programmatic access to both data and services. The three Aspects are designed to be fully integrated, enabling seamless workflows across the RSP. The data products described in §3 are accessible via all three Aspects, and the system facilitates operations such as starting a query in one Aspect and retrieving its results in another. Figure 41 shows the RSP landing page in the Google cloud.

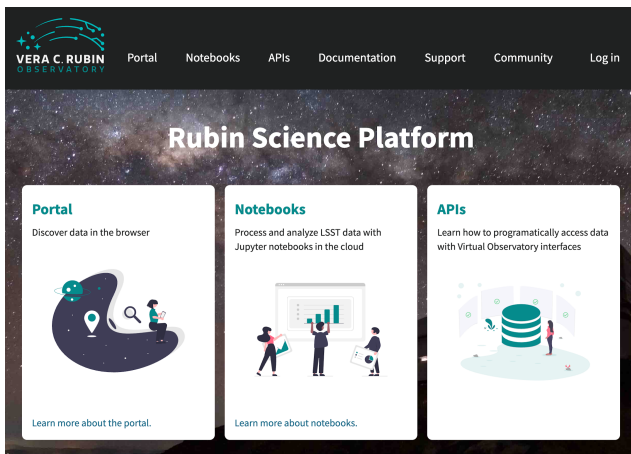


Figure 41. The RSP landing page at <https://data.lsst.cloud/> showing the three user-facing Aspects as well as links to documentation and support information.

The RSP is supported by a number of backend services, including databases, files, and batch computing. Support for collaborative work through shared workspaces is also included in the RSP.

A preview of the RSP was launched on Google Cloud in 2022, operating under a shared-risk model to support DP0 (W. O’Mullane et al. 2024a). This allowed the community to test the platform, begin preparations for science, and provide valuable feedback to inform ongoing development. It was the first time an astronomical research environment was hosted in a cloud environment. The DP1 release brings major updates to RSP services, enhancing scientific analysis capabilities. The RSP remains under active development, with incremental improvements being rolled out as they mature. During the Rubin Early Science Phase, the RSP will continue to operate under a shared-risk model. This section out-

lines the RSP functionality available at the time of the DP1 release and provides an overview of planned future capabilities.

6.1. Rubin Data Access Center

The Rubin US DAC utilizes a novel hybrid on-premises cloud architecture, which combines on-premises infrastructure at the USDF at SLAC with flexible and scalable resources in the Google cloud. This architecture has been deployed and tested using the larger simulated dataset of DP0.2 (W. O’Mullane et al. 2024b).

In this hybrid model, user-facing services are deployed in the cloud to support dynamic scaling in response to user demand and to simplify the provisioning and management of large numbers of science user accounts. The majority of the static data products described in §3 are stored on premises at the USDF to benefit from cost-effective mass storage and close integration with Rubin data processing infrastructure, also located at the USDF. For imaging data, the Data Butler (§6.2.2) provides the interface between cloud-based users and data services, and the on-premises data. For catalog data, a cloud-based TAP client (§6.2.1) submits queries to the on-premises Qserv database cluster (§6.5) and retrieves the results. In the initial DP1 deployment, catalog data are hosted at the USDF while image data are stored in the cloud. The full hybrid model will be rolled out and further tested following the release of DP1. The RSP features a single sign-on authentication and authorization system to provide secure access for Rubin data rights holders (R. Blum & the Rubin Operations Team 2020).

6.2. Application Programming Interface Aspect

The API Aspect provides a comprehensive set of user-facing interfaces for programmatic access to the DP1 data products, through both IVOA-compliant services and the Rubin Data Butler. IVOA services enable standard queries and integration with existing tools, while the Butler facilitates advanced data processing within the LSST Science Pipelines.

At the time of the DP1 release, some IVOA services are unavailable, and certain data products are only accessible via the Butler. This section provides an overview of the available IVOA services and Butler access.

6.2.1. IVOA Services

Rubin has adopted a Virtual Observatory (VO)-first design philosophy, prioritizing compliance with IVOA standard interfaces to foster interoperability, standardization, and collaboration. In cases where standardized

protocols have yet to be established, additional services have been introduced to complement these efforts. This approach ensures that the RSP can be seamlessly integrated with community-standard tools such as **Tool for Operations on Catalogues And Tables (TOPCAT)** (M. Taylor 2011) and **Aladin** (F. Bonnarel et al. 2000; T. Boch & P. Fernique 2014; M. Baumann et al. 2022), as well as libraries such as **PyVO** (M. Graham et al. 2014).

The user-facing APIs are also used internally within the RSP, creating a unified design that ensures consistent and reproducible workflows across all three Aspects. This reduces code duplication, simplifies maintenance, and ensures all users, both internal and external, access data in the same way. For example, an **Astronomical Data Query Language (IVOA standard) (ADQL)** query on the **Object** catalog via TAP yields identical results whether run from the Portal, Notebook, or an external client.

The following IVOA services are available at the time of the DP1 release.

- **TAP service:** A TAP service (P. Dowler et al. 2019) enables queries of catalog data via the IVOA-standard **ADQL**, a dialect of SQL92 with spherical geometry extensions. The main TAP service for DP1 runs on the Rubin-developed **Qserv** database (§ 6.5), which hosts the core science tables described in §3.2, as well as the **Visit** database. It also provides image metadata in the IVOA **ObsCore** format via the standard `ivoa.ObsCore` table, making it an “ObsTAP” service (M. Louys et al. 2017). The TAP service is based on the **Canadian Astronomy Data Centre (CADC)**’s open-source Java TAP implementation¹⁰⁹, modified for the exact query language accepted by Qserv. It currently supports a large subset of ADQL, with limitations documented in the Data Release materials (see §7.1) and exposed via the TAP capabilities endpoint where possible.

The TAP service provides metadata annotations consistent with the standard, including table and column descriptions, indications of foreign-key relationships between tables, and column metadata such as units and IVOA unified content descriptors (UCDs).

- **Image access services:** Rubin image access services are compliant with IVOA Simple Image Access Protocol, version 2 (SIAv2; T. Jenness et al. 2024; P. Dowler et al. 2015) for discovering and

accessing astronomical images based on metadata. SIAv2 is a **REpresentational State Transfer (REST)**-based protocol designed for the discovery and retrieval of image data. It allows, for instance, querying all images in a given band over a defined sky region and time period.

Users identify an image or observation of interest and query the service. The result set includes metadata about the image, such as the sky position, time, or band, and a data-access URL, which includes an IVOA Identifier uniquely identifying the dataset (T. Jenness & G. P. Dubois-Felsmann 2026), allowing the dataset to be retrieved or a cutout requested via **Server-side Operations for Data Access (IVOA standard) (SODA)** (SODA; F. Bonnarel et al. 2017).

- **Image Cutout Service:** The Rubin Cutout Service (R. Allbery 2023, 2024) is based on the IVOA SODA standard (F. Bonnarel et al. 2017). Users submit requests specifying sky coordinates and the cutout size as the radius from the coordinates, and the service performs the operation on the full image and returns a result set. For DP1, the Cutout Service is a single Cutout Service only where N cutout requests will require N independent synchronous calls. We expect some form of bulk Cutout Service by mid 2026.
- **HiPS Data Service:** An authenticated **HiPS** (P. Fernique et al. 2017) Data Service for seamless pan-and-zoom access to large-scale coadds. It supports fast interactive progressive image exploration at a range of resolutions.
- **Web Distributed Authoring and Versioning (WebDav):** A WebDav service is provided to enable users to remotely manage, edit, and organize files and directories on the RSP as if they were local files on their own computer. This is especially useful for local development.

6.2.2. Data Butler

The Rubin Data Butler (T. Jenness et al. 2022; N. B. Lust et al. 2023), is a high-level interface designed to facilitate seamless access to data for both users and software systems. This includes managing storage formats, physical locations, data staging, and database mappings. A Butler repository contains two components.

- The *Data Store*. A physical storage system for datasets, e.g., a **Portable Operating System In-**

¹⁰⁹ <https://github.com/opencadc/tap>

Table 7. Tract coverage of each DP1 field. The size of a tract is larger than the LSSTComCam field of view; however, since each observed field extends across more than one tract, each field covers multiple tracts.

Field Code	Tract ID
47_Tuc	453, 454
ECDFS	4848, 4849, 5062, 5063, 5064
EDFS_comcam	2234, 2235, 2393, 2394
Fornax_dSph	4016, 4017, 4217, 4218
Rubin_SV_095_-25	5305, 5306, 5525, 5526
Rubin_SV_38_7	10221, 10222, 10463, 10464, 10704, 10705
Seagull	7610, 7611, 7849, 7850

terface (POSIX) file system or (Amazon) Simple Storage Service (S3) object store.

- The *Registry*. A Structured Query Language (SQL)-compatible database that stores metadata about the datasets in the Data Store.

For DP1, the Butler repository is hosted in the Google Cloud, using an S3-compatible store for datasets and AlloyDB, a PostgreSQL-compatible database, for the Registry.

In the context of the Butler, a dataset refers to a unique data product, such as an image, catalog or map, generated by the observatory or processing pipelines. Datasets belong to one of the various types of data products, described in §3. The Butler ensures that each dataset is uniquely identifiable by a combination of three pieces of information: a data coordinate, a dataset type, and a run collection. For example, a dataset that represents a single raw image in the *i* band taken on the night starting 2024-11-11 with exposure ID 2024111100074 would be represented as `dataId='exposure':2024111100074, 'band':'i', 'instrument':'LSSTComCam'` and is associated with the `raw` dataset type. For a deep coadd on a patch of sky in the Seagull field, there would be no exposure dimensions and instead the tract, patch and band would be specified as `dataId='tract':7850, 'patch':6, 'band':'g', 'instrument':'LSSTComCam', sky map='lsst_cells_v1'` and is associated with the `deep_coadd` DatasetType. The tract identification numbers and corresponding target names for these tracts are listed in Table 7.

The data coordinate is used to locate a dataset in multidimensional space, where dimensions are defined in terms of scientifically meaningful concepts, such as

instrument, visit, detector or band. For example, a calibrated single-visit image (§3.1) has dimensions including band, instrument, and detector. In contrast, the visit table (§3.2), a catalog of all calibrated single-epoch visits in DP1, has only the instrument dimension. The main dimensions used in DP1 are listed, together with a brief description, in Table 8. To determine which dimensions are relevant for a specific dataset, the Butler defines dataset types, which associate each dataset with its specific set of relevant dimensions, as well as the associated Python type representing the dataset. The dataset type defines the kind of data a dataset represents, such as a raw image (`raw`), a processed catalog (`object_forced_source`), or a sky map (`skymap`). Table 9 lists all the dataset types available via the Butler in DP1, together with the dimensions needed to uniquely identify a specific dataset and the number of unique datasets of each type.

It is important to highlight a key difference between accessing catalog data via the TAP service versus the Butler. While the TAP service contains entire catalogs, many of the same catalogs in the Butler are split into multiple separate catalogs. This is partly due to how these catalogs are generated, but also because of the way data are stored within and retrieved from the Butler repository – it is inefficient to retrieve the entire Source catalog, for example, from the file system. Instead, because the Source catalog contains data for sources detected in the `visit_images`, there is one Source catalog in the Butler for each `visit_image`. Similarly, there is one Object catalog for each `deep_coadd`. All of the catalogs described in §3.2, aside from the `CcdVisit`, `SSObject`, `SSSource`, and `Calibration` catalogs, are split within the Butler.

A dataset is associated with one or more *Collections*. Collections are logical groupings of datasets within the Butler system that were created or processed together by the same batch operation. Collections allow multiple datasets with the same data coordinate to coexist without conflict and support flexible, parallel processing by enabling repeated analyses of the same input data using different configurations. The DP1 Butler is read only; a writable Butler is expected by mid-2026.

6.2.3. Remote Programmatic Access

The Rubin RSP API can be accessed from a local system by data rights holders outside of the RSP, by creating a user security token. This token can then be used as a bearer token for API calls to the RSP TAP service. This capability is especially useful for remote data analysis using tools such as TOPCAT, as well as enabling third-party systems, e.g., community Aalert brokers, to

Table 8. Descriptions of and valid values for the key data dimensions in DP1. YYYYMMDD signifies date and # signifies a single 0–9 digit.

Dimension	Format or Valid Values	Description
day_obs	YYYYMMDD	A day and night of observations that rolls over during daylight hours.
visit	YYYYMMDD#####	A sequence of observations processed together; synonymous with “exposure” in DP1.
exposure	YYYYMMDD#####	A single exposure of all nine LSSTComCam detectors.
instrument	LSSTComCam	The instrument name.
detector	0–8	A LSSTComCam detector.
skymap	lsst_cells_v1	A set of tracts and patches that subdivide the sky into rectangular regions with simple projections and intentional overlaps.
tract	See Table 7	A large rectangular region of the sky.
patch	0–99	A rectangular region within a tract.
physical_filter	u_02, g_01, i_06, r_03, z_03, y_04	A physical filter.
band	u, g, r, i, z, y	An conceptual astronomical passband.

Table 9. The name and number of each type of data product in the Butler and the dimensions required to identify a specific dataset.

Data Product	Name in Butler	Required Dimensions	Number in DP1
Image Data Products			
raw	raw	instrument, detector, exposure	16125
visit_image	visit_image	instrument, detector, visit	15972
deep_coadd	deep_coadd	band, skymap, tract, patch	2644
template_coadd	template_coadd	band, skymap, tract, patch	2730
difference_image	difference_image	instrument, detector, visit	15972
Catalog Data Products			
Source	source	instrument, visit	1786
Object	object	skymap, tract	29
ForcedSource	object_forced_source	skymap, tract, patch	636
DiaSource	dia_source	skymap, tract	25
DiaObject	dia_object	skymap, tract	25
ForcedSourceOnDiaObject	dia_object_forced_source	skymap, tract, patch	597
SSSource	ss_source	–	1
SSObject	ss_object	–	1
Visit	visit_table	instrument	1
CcdVisit	visit_detector_table	instrument	1

2946 access Rubin data. Additionally, it supports remote de- 2953
 2947 velopment, allowing for more flexible workflows and in- 2954
 2948 tegration with external systems. 2955

2949 6.3. Portal Aspect 2956

2950 The Portal Aspect provides an interactive web-based 2958
 2951 environment for exploratory data discovery, filtering, 2959
 2952 querying, and visualization of both image and catalog 2960

data, without requiring programming expertise. It en-
 ables users to access and analyze large datasets via tools
 for catalog queries, image browsing, time-series inspec-
 tion, and cross-matching.

The Portal is built on [Firefly](#) (X. Wu et al. 2019), a
 web application framework developed by the Infrared
 Processing and Analysis Center. [Firefly](#) provides in-
 teractive capabilities such as customizable table views,

image overlays, multipanel visualizations, and synchronized displays linking catalog and image data.

Designed to support both exploratory data access and detailed scientific investigation, the Portal delivers an intuitive user experience, allowing users to visually analyze data while retaining access to underlying metadata and query controls.

6.4. Notebook Aspect

The Notebook Aspect provides an interactive, web-based environment built on Jupyter Notebooks, enabling users to write and execute Python code directly on Rubin and LSST data without downloading it locally. It offers programmatic access to Rubin and LSST data products, allowing users to query and retrieve datasets, manipulate and display images, compute derived properties, plot results, and reprocess data using the LSST Science Pipelines (§4.1). The environment comes preinstalled with the Pipelines and a broad set of widely used astronomical software tools, supporting immediate and flexible data analysis.

6.5. Databases

The user-facing Aspects of the RSP are supported by several backend databases that store catalog data products, image metadata, and other derived datasets. The schema for DP1 and other Rubin databases are available online at <https://sdm-schemas.lsst.io>.

6.5.1. Qserv

The final 10 yr LSST catalog is expected to reach 15 PB and contain measurements for billions of stars and galaxies across trillions of detections. To support efficient storage, querying, and analysis of this dataset, Rubin Observatory developed Qserv (D. L. Wang et al. 2011; F. Mueller et al. 2025) – a scalable, parallel, distributed SQL database system. Qserv partitions data over approximately equal-area regions of the celestial sphere, replicates data to ensure resilience and high availability, and uses shared scanning to reduce overall I/O load. It also supports a package of scientific user-defined functions (SciSQL¹¹⁰) simplifying complex queries involving spherical geometry, statistics, and photometry. Qserv is built on robust production-quality components, including MariaDB¹¹¹ and XRootD¹¹². Qserv runs at the USDF and user access to catalog data is via the TAP service (§6.2.1). This

enables catalog-based analysis through both the RSP Portal and Notebook Aspects.

Although the small DP1 dataset does not require Qserv’s full capabilities, we nevertheless chose to use it for DP1 to accurately reflect the future data-access environment and to gain experience with scientifically motivated queries ahead of full-scale deployment. Qserv is open-source and available on GitHub at <https://github.com/lsst/qserv>.

7. SUPPORT FOR COMMUNITY SCIENCE

Rubin Observatory has a science community that encompasses thousands of individuals worldwide, with a broad range of experience and expertise in astronomy in general, and in the analysis of optical imaging data specifically.

Rubin’s model to support this diverse community to access and analyze DP1 emphasizes self-help via documentation and tutorials, and employs an open platform for asynchronous issue reporting that enables crowd-sourced solutions. These two aspects of community support are augmented by virtual engagement activities. In addition, Rubin supports its Users Committee to advocate on behalf of the science community, and supports the eight LSST Science Collaborations (§7.6).

All of the resources for scientists that are discussed in this section are discoverable by browsing the For Scientists pages of the Rubin Observatory website¹¹³.

7.1. Documentation

The Data Release documentation for DP1¹¹⁴ provides an overview of the LSSTComCam observations, detailed descriptions of the data products, and a high-level summary of the processing pipelines. Although much of its content overlaps significantly with this paper, the documentation is presented as a searchable, web-based resource built using Sphinx¹¹⁵, with a focus on enabling scientific use of the data products.

7.2. Tutorials

A suite of tutorials (NSF-DOE Vera C. Rubin Observatory 2021) that demonstrate how to access and analyze DP1 using the RSP accompanies the DP1 release¹¹⁶. Jupyter Notebook tutorials are available via the Tutorials drop-down menu within the Notebook aspect of the RSP. Tutorials for the Portal and API aspects of the RSP can be found in the Data Release documentation.

¹¹⁰ <https://smonkewitz.github.io/scisql/>

¹¹¹ <https://www.mariadb.org/>

¹¹² <https://xrootd.org/>

¹¹³ <https://rubinobservatory.org/for-scientists>

¹¹⁴ <https://dp1.lsst.io>

¹¹⁵ <https://www.sphinx-doc.org/>

¹¹⁶ <https://dp1.lsst.io/tutorials>

These tutorials are designed to be inclusive, accessible, clear, focused, and consistent. Their format and contents follow a set of guidelines (M. L. Graham et al. 2026) that are informed by modern standards in technical writing.

7.3. Community Forum

The venue for all user support is the Rubin Community Forum¹¹⁷. Questions about any and all aspects of the Rubin data products, pipelines, and services, including DP1, should be posted as new topics in the Support category. This includes beginner-level and “how-to” questions, advanced scientific analysis questions, technical bug reports, account and data-access issues, and everything in between. The Support category of the Forum is monitored by Rubin staff, who follow an established internal workflow for following-up and resolving all reported issues.

The Rubin Community Forum is built on the open-source Discourse platform. It was chosen because, for a worldwide community of 10,000 Rubin users, a traditional (i.e., closed) help desk represents a risk to Rubin science (e.g., many users with the same question having to wait for responses). The open nature of the Forum enables self-help by letting users search for similar issues, and enables crowd-sourced problem solving (and avoids knowledge bottlenecks) by letting users help users.

The Rubin Community Forum, and the internal staff workflows for user support, were set up, tested, and refined with DP0 so that it was ready for use with DP1.

7.4. Engagement Activities

A variety of live virtual and in-person workshops and seminars offer learning opportunities to scientists and students working with the Rubin data products, services, and tools.

- *Rubin Science Assemblies (weekly, virtual, 1 hour)*. These alternate between hands-on tutorials based on the most recent Data Release and open drop-in “office hours” with Rubin staff.
- *Rubin Data Academy (annual, virtual, 3-4 days)*. This is an intense set of hands-on tutorials based on the most recent Data Release, along with coworking and networking sessions.
- *Rubin Community Workshop (annual, virtual, 5 days)*. This is a science-focused conference of contributed posters, talks, and sessions led by mem-

bers of the Rubin science community and Rubin staff.

Following the release of DP1, all of these engagement activities focused on use of DP1 by the science community. In particular, the 2025 Rubin Data Academy was run the week of the DP1 release, in order to immediately facilitate community access. The 2025 Rubin Community Workshop had several sessions to introduce people to the DP1 dataset and demonstrate how to access and analyze it with the RSP.

For schedules, connection information, zoom recordings, and associated materials, visit the For Scientists pages of the Rubin Observatory website¹¹⁸. Requests for custom tutorials and presentations for research groups are also accommodated.

7.5. Users Committee

This committee is charged with soliciting feedback from the science community, advocating on their behalf, and recommending science-driven improvements to the LSST data products and the RSP tools and services. Community members are encouraged to attend their virtual meetings and raise issues to their attention, so they can be included in the committee’s twice-yearly reports to the Rubin Observatory Director.

Like the Forum, the Users Committee was established and began its work with DP0, and that feedback was implemented for DP1. The community’s response to DP1 will be especially valuable input to DP2 and DR1, and the Users Committee encourages all users to interact with them. For a list of members and contact information, visit the For Scientists pages of the Rubin Observatory website.

7.6. Science Collaborations

The eight LSST Science Collaborations are independent, worldwide communities of scientists, self-organized into collaborations based on their research interests and expertise. Members work together to apply for funding, build software infrastructure and analysis algorithms, and incorporate external datasets into their LSST-based research.

The Science Collaborations also provide valuable advice to Rubin Observatory on the operational strategies and data products to accomplish specific science goals, and Rubin Observatory supports the collaborations via staff liaisons and regular virtual meetings with Rubin Operations leadership.

¹¹⁷ <https://community.lsst.org/>

¹¹⁸ <https://rubinobservatory.org/for-scientists/events-deadlines>

3141 The Science Collaborations have been functioning for
 3142 many years, and their engagement and feedback on DP0
 3143 was implemented into the community science model for
 3144 DP1, as it will for future Data Releases.

3145 8. SUMMARY AND FUTURE RELEASES

3146 Rubin DP1 offers an initial look at the first on-sky
 3147 data products and access services from the Vera C. Ru-
 3148 bin Observatory. DP1 forms part of Rubin’s Early Sci-
 3149 ence Program, and provides the scientific community
 3150 with an early opportunity to familiarize themselves with
 3151 the data formats and access infrastructure for the forth-
 3152 coming Legacy Survey of Space and Time. This early
 3153 release has a proprietary period of 2 yr, during which
 3154 time it is available to Rubin data rights holders only via
 3155 the cloud-based RSP.

3156 In this paper we have described the completion status
 3157 of the observatory at the time of data acquisition, the
 3158 commissioning campaign that forms the basis of DP1,
 3159 and the processing pipelines used to produce early ver-
 3160 sions of data products. We provide details on the data
 3161 products, their characteristics and known issues, and
 3162 describe the RSP for access to and analysis of DP1.

3163 The data products described in this paper derive from
 3164 observations obtained by LSSTComCam. LSSTCom-
 3165 Cam contains only around 5% the number of CCDs as
 3166 LSSTCam, yet the DP1 dataset that it has produced
 3167 will already enable a very broad range of science. At
 3168 3.5 TB in size, DP1 covers a total area of ~ 15 deg² and
 3169 contains 1792 single-epoch images, 2644 deep coadded
 3170 images and 2.3 million distinct astrophysical objects, in-
 3171 cluding 93 new asteroid discoveries.

3172 While some data products anticipated from the LSST
 3173 are not yet available, e.g., cell-based coadds, DP1 in-
 3174 cludes several products that will not be provided in fu-
 3175 ture releases. Notably, difference images are included in
 3176 DP1 as pregenerated products; in future releases, these
 3177 will instead be generated on demand via dedicated ser-
 3178 vices. The inclusion of pregenerated difference images
 3179 in DP1 is feasible due to the relatively small size of the
 3180 dataset, an approach that will not scale to the signifi-
 3181 cantly larger data volumes expected in subsequent re-
 3182 leases.

3183 The RSP is continually under development, and new
 3184 functionality will continue to be deployed incrementally
 3185 as it becomes available, and independent of the future
 3186 Data Release schedule. User query history capabilities,
 3187 context-aware documentation and a bulk Cutout Service
 3188 are just a few of the services currently under develop-
 3189 ment.

3190 Coincident with the release of DP1, Rubin Observa-
 3191 tory begins its Science Validation Surveys with LSST-

3192 Cam. This final commissioning phase will produce a
 3193 dataset that will form the foundation for the second Ru-
 3194 bin Data Preview, DP2. Full operations, marking the
 3195 start of the LSST, are expected to commence in 2026.

3196 ACKNOWLEDGMENTS

3197 . This material is based upon work supported in part by
 3198 the National Science Foundation through Cooperative
 3199 Agreements AST-1258333 and AST-2241526 and Co-
 3200 operative Support Agreements AST-1202910 and AST-
 3201 2211468 managed by the Association of Universities for
 3202 Research in Astronomy (AURA), and the Department of
 3203 Energy under Contract No. DE-AC02-76SF00515 with
 3204 the SLAC National Accelerator Laboratory managed
 3205 by Stanford University. Additional Rubin Observatory
 3206 funding comes from private donations, grants to univer-
 3207 sities, and in-kind support from LSST-DA Institutional
 3208 Members.

3209 This work has been supported by the French Na-
 3210 tional Institute of Nuclear and Particle Physics (IN2P3)
 3211 through dedicated funding provided by the National
 3212 Center for Scientific Research (CNRS).

3213 This work has been supported by STFC fund-
 3214 ing for UK participation in LSST, through grant
 3215 ST/Y00292X/1.

3216 *Facilities:* Rubin:Simonyi (LSSTComCam), Ru-
 3217 bin:USDAC

3218 *Software:* Rubin Data Butler (T. Jenness et al.
 3219 2022), LSST Science Pipelines (Rubin Observatory Sci-
 3220 ence Pipelines Developers 2025), LSST Feature Based
 3221 Scheduler v3.0 (P. Yoachim et al. 2024; E. Naghib et al.
 3222 2019) Astropy (Astropy Collaboration et al. 2013, 2018,
 3223 2022) PIFF (M. Jarvis et al. 2021a), GBDES (G. M.
 3224 Bernstein 2022), Qserv (D. L. Wang et al. 2011; F.
 3225 Mueller et al. 2025), Slurm, HTCondor, CVMFS, FTS3,
 3226 ESNNet

APPENDIX

REFERENCES

- 3228 Abazajian, K., Adelman-McCarthy, J. K., Agüeros, M. A.,
3229 et al. 2004, *AJ*, 128, 502, doi: [10.1086/421365](https://doi.org/10.1086/421365)
- 3230 Ahumada, R., Allende Prieto, C., Almeida, A., et al. 2020,
3231 *ApJS*, 249, 3, doi: [10.3847/1538-4365/ab929e](https://doi.org/10.3847/1538-4365/ab929e)
- 3232 Aihara, H., AIsayyad, Y., Ando, M., et al. 2022, *PASJ*, 74,
3233 247, doi: [10.1093/pasj/psab122](https://doi.org/10.1093/pasj/psab122)
- 3234 Allbery, R. 2023, IVOA SODA implementation experience,
3235 SQuaRE Technical Note SQR-063, NSF-DOE Vera C.
3236 Rubin Observatory. <https://sqr-063.lsst.io/>
- 3237 Allbery, R. 2024, Draft IVOA SODA web service
3238 specification, SQuaRE Technical Note SQR-093,
3239 NSF-DOE Vera C. Rubin Observatory.
3240 <https://sqr-093.lsst.io/>
- 3241 AIsayyad, Y. 2018, Coaddition Artifact Rejection and
3242 CompareWarp, Data Management Technical Note
3243 DMTN-080, NSF-DOE Vera C. Rubin Observatory,
3244 doi: [10.71929/rubin/2583441](https://doi.org/10.71929/rubin/2583441)
- 3245 Ansel, J., Yang, E., He, H., et al. 2024, in 29th ACM
3246 International Conference on Architectural Support for
3247 Programming Languages and Operating Systems, Volume
3248 2 (ASPLOS '24) (ACM), doi: [10.1145/3620665.3640366](https://doi.org/10.1145/3620665.3640366)
- 3249 Antilogus, P., Astier, P., Doherty, P., Guyonnet, A., &
3250 Regnault, N. 2014, *Journal of Instrumentation*, 9,
3251 C03048, doi: [10.1088/1748-0221/9/03/C03048](https://doi.org/10.1088/1748-0221/9/03/C03048)
- 3252 Astropy Collaboration, Robitaille, T. P., Tollerud, E. J.,
3253 et al. 2013, *A&A*, 558, A33,
3254 doi: [10.1051/0004-6361/201322068](https://doi.org/10.1051/0004-6361/201322068)
- 3255 Astropy Collaboration, Price-Whelan, A. M., Sipőcz, B. M.,
3256 et al. 2018, *AJ*, 156, 123, doi: [10.3847/1538-3881/aabc4f](https://doi.org/10.3847/1538-3881/aabc4f)
- 3257 Astropy Collaboration, Price-Whelan, A. M., Lim, P. L.,
3258 et al. 2022, *ApJ*, 935, 167, doi: [10.3847/1538-4357/ac7c74](https://doi.org/10.3847/1538-4357/ac7c74)
- 3259 Baumann, M., Boch, T., Pineau, F.-X., et al. 2022, in
3260 *Astronomical Society of the Pacific Conference Series*,
3261 Vol. 532, *Astronomical Data Analysis Software and*
3262 *Systems XXX*, ed. J. E. Ruiz, F. Pierfederici, &
3263 P. Teuben, 7
- 3264 Bechtol, K., Sevilla-Noarbe, I., Drlica-Wagner, A., et al.
3265 2026, *ApJS*, 282, 62, doi: [10.3847/1538-4365/ae18d3](https://doi.org/10.3847/1538-4365/ae18d3)
- 3266 Berk, A., Anderson, G. P., Bernstein, L. S., et al. 1999, in
3267 *Society of Photo-Optical Instrumentation Engineers*
3268 *(SPIE) Conference Series*, Vol. 3756, *Optical*
3269 *Spectroscopic Techniques and Instrumentation for*
3270 *Atmospheric and Space Research III*, ed. A. M. Larar,
3271 348–353, doi: [10.1117/12.366388](https://doi.org/10.1117/12.366388)
- 3272 Bernstein, G. M. 2022, gbdes: DECcam instrumental
3273 signature fitting and processing programs,, *Astrophysics*
3274 *Source Code Library*, record ascl:2210.011
3275 <http://ascl.net/2210.011>
- 3276 Bernstein, G. M., & Jarvis, M. 2002, *AJ*, 123, 583,
3277 doi: [10.1086/338085](https://doi.org/10.1086/338085)
- 3278 Bernstein, G. M., Armstrong, R., Plazas, A. A., et al. 2017,
3279 *PASP*, 129, 074503, doi: [10.1088/1538-3873/aa6c55](https://doi.org/10.1088/1538-3873/aa6c55)
- 3280 Bertin, E. 2011, in *Astronomical Society of the Pacific*
3281 *Conference Series*, Vol. 442, *Astronomical Data Analysis*
3282 *Software and Systems XX*, ed. I. N. Evans,
3283 A. Accomazzi, D. J. Mink, & A. H. Rots, 435
- 3284 Bianco, F. B., Ivezić, Ž., Jones, R. L., et al. 2022, *ApJS*,
3285 258, 1, doi: [10.3847/1538-4365/ac3e72](https://doi.org/10.3847/1538-4365/ac3e72)
- 3286 Blum, R., & the Rubin Operations Team. 2020, Vera C.
3287 Rubin Observatory Data Policy, Data Management
3288 Operations Controlled Document RDO-013, NSF-DOE
3289 Vera C. Rubin Observatory. <https://ls.st/RDO-013>
- 3290 Boch, T., & Fernique, P. 2014, in *Astronomical Society of*
3291 *the Pacific Conference Series*, Vol. 485, *Astronomical*
3292 *Data Analysis Software and Systems XXIII*, ed.
3293 N. Manset & P. Forshay, 277
- 3294 Bonnarel, F., Dowler, P., Demleitner, M., Tody, D., &
3295 Dempsey, J. 2017, IVOA Server-side Operations for Data
3296 Access Version 1.0., IVOA Recommendation 17 May 2017
3297 doi: [10.5479/ADS/bib/2017ivoa.spec.0517B](https://doi.org/10.5479/ADS/bib/2017ivoa.spec.0517B)
- 3298 Bonnarel, F., Fernique, P., Bienaymé, O., et al. 2000,
3299 *A&AS*, 143, 33, doi: [10.1051/aas:2000331](https://doi.org/10.1051/aas:2000331)
- 3300 Bosch, J., Armstrong, R., Bickerton, S., et al. 2018, *PASJ*,
3301 70, S5, doi: [10.1093/pasj/psx080](https://doi.org/10.1093/pasj/psx080)
- 3302 Broughton, A., Utsumi, Y., Plazas Malagón, A. A., et al.
3303 2024, *PASP*, 136, 045003, doi: [10.1088/1538-3873/ad3aa2](https://doi.org/10.1088/1538-3873/ad3aa2)
- 3304 Burke, D. L., Rykoff, E. S., Allam, S., et al. 2018, *AJ*, 155,
3305 41, doi: [10.3847/1538-3881/aa9f22](https://doi.org/10.3847/1538-3881/aa9f22)
- 3306 Chambers, K. C., Magnier, E. A., Metcalfe, N., et al. 2016,
3307 *arXiv e-prints*, arXiv:1612.05560,
3308 doi: [10.48550/arXiv.1612.05560](https://doi.org/10.48550/arXiv.1612.05560)

- 3309 Choi, Y., Olsen, K. A. G., Carlin, J. L., et al. 2025, The
 3310 Astrophysical Journal, 992, 47,
 3311 doi: [10.3847/1538-4357/adfb70](https://doi.org/10.3847/1538-4357/adfb70)
- 3312 de Vaucouleurs, G. 1948, *Annales d’Astrophysique*, 11, 247
 3313 de Vaucouleurs, G. 1953, *MNRAS*, 113, 134,
 3314 doi: [10.1093/mnras/113.2.134](https://doi.org/10.1093/mnras/113.2.134)
- 3315 Dowler, P., Bonnarel, F., & Tody, D. 2015, IVOA Simple
 3316 Image Access Version 2.0., IVOA Recommendation 23
 3317 December 2015
 3318 doi: [10.5479/ADS/bib/2015ivoa.spec.1223D](https://doi.org/10.5479/ADS/bib/2015ivoa.spec.1223D)
- 3319 Dowler, P., Rixon, G., Tody, D., & Demleitner, M. 2019,
 3320 Table Access Protocol Version 1.1., IVOA
 3321 Recommendation 27 September 2019
 3322 doi: [10.5479/ADS/bib/2019ivoa.spec.0927D](https://doi.org/10.5479/ADS/bib/2019ivoa.spec.0927D)
- 3323 Eggl, S., Juric, M., Moeyens, J., & Jones, L. 2020, in
 3324 AAS/Division for Planetary Sciences Meeting Abstracts,
 3325 Vol. 52, AAS/Division for Planetary Sciences Meeting
 3326 Abstracts, 211.01
- 3327 Esteves, J. H., Utsumi, Y., Snyder, A., et al. 2023, *PASP*,
 3328 135, 115003, doi: [10.1088/1538-3873/ad0a73](https://doi.org/10.1088/1538-3873/ad0a73)
- 3329 Euclid Collaboration, Romelli, E., Kümmel, M., et al. 2025,
 3330 arXiv e-prints, arXiv:2503.15305,
 3331 doi: [10.48550/arXiv.2503.15305](https://doi.org/10.48550/arXiv.2503.15305)
- 3332 Fagrelus, P., & Rykoff, E. S. 2025, Rubin Observatory
 3333 Baseline Calibration Plan, Commissioning Technical
 3334 Note SITCOMTN-086, NSF-DOE Vera C. Rubin
 3335 Observatory, doi: [10.71929/rubin/2583850](https://doi.org/10.71929/rubin/2583850)
- 3336 Ferguson, P. S., Rykoff, E. S., Carlin, J. L., Saunders, C., &
 3337 Parejko, J. K. 2025, The Monster: A reference catalog
 3338 with synthetic ugrizy-band fluxes for the Vera C. Rubin
 3339 observatory, Data Management Technical Note
 3340 DMTN-277, NSF-DOE Vera C. Rubin Observatory,
 3341 doi: [10.71929/rubin/2583688](https://doi.org/10.71929/rubin/2583688)
- 3342 Fernique, P., Allen, M. G., Boch, T., et al. 2015, *A&A*, 578,
 3343 A114, doi: [10.1051/0004-6361/201526075](https://doi.org/10.1051/0004-6361/201526075)
- 3344 Fernique, P., Allen, M., Boch, T., et al. 2017, HiPS -
 3345 Hierarchical Progressive Survey Version 1.0., IVOA
 3346 Recommendation 19 May 2017
 3347 doi: [10.5479/ADS/bib/2017ivoa.spec.0519F](https://doi.org/10.5479/ADS/bib/2017ivoa.spec.0519F)
- 3348 Finkbeiner, D. P., Davis, M., & Schlegel, D. J. 1999, *ApJ*,
 3349 524, 867, doi: [10.1086/307852](https://doi.org/10.1086/307852)
- 3350 Fortino, W. F., Bernstein, G. M., Bernardinelli, P. H., et al.
 3351 2021, *AJ*, 162, 106, doi: [10.3847/1538-3881/ac0722](https://doi.org/10.3847/1538-3881/ac0722)
- 3352 Gaia Collaboration, Montegriffo, P., Bellazzini, M., et al.
 3353 2023a, *A&A*, 674, A33,
 3354 doi: [10.1051/0004-6361/202243709](https://doi.org/10.1051/0004-6361/202243709)
- 3355 Gaia Collaboration, Vallenari, A., Brown, A. G. A., et al.
 3356 2023b, *A&A*, 674, A1, doi: [10.1051/0004-6361/202243940](https://doi.org/10.1051/0004-6361/202243940)
- 3357 Górski, K. M., Hivon, E., Banday, A. J., et al. 2005, *ApJ*,
 3358 622, 759, doi: [10.1086/427976](https://doi.org/10.1086/427976)
- 3359 Graham, A. W., & Driver, S. P. 2005, *PASA*, 22, 118,
 3360 doi: [10.1071/AS05001](https://doi.org/10.1071/AS05001)
- 3361 Graham, M., Plante, R., Tody, D., & Fitzpatrick, M. 2014,
 3362 PyVO: Python access to the Virtual Observatory,,
 3363 Astrophysics Source Code Library, record ascl:1402.004
- 3364 Graham, M. L., Carlin, J. L., Adair, C. L., et al. 2026,
 3365 Guidelines for User Tutorials, Technical Note RTN-045,
 3366 NSF-DOE Vera C. Rubin Observatory,
 3367 doi: [10.71929/rubin/2584020](https://doi.org/10.71929/rubin/2584020)
- 3368 Gray, B. 2025, find_orb: Orbit determination from
 3369 observations, https://github.com/Bill-Gray/find_orb
- 3370 Guy, L. P., AlSayyad, Y., Bechtol, K., et al. 2026, Rubin
 3371 Observatory Plans for an Early Science Program,
 3372 Technical Note RTN-011, NSF-DOE Vera C. Rubin
 3373 Observatory, doi: [10.71929/rubin/2584021](https://doi.org/10.71929/rubin/2584021)
- 3374 Heinze, A., Eggl, S., Juric, M., et al. 2022, in AAS/Division
 3375 for Planetary Sciences Meeting Abstracts, Vol. 54,
 3376 AAS/Division for Planetary Sciences Meeting Abstracts,
 3377 504.04
- 3378 Heinze, A., Juric, M., & Kurlander, J. 2023, heliolineX: Open
 3379 Source Solar System Discovery Software,
 3380 <https://github.com/heliolineX/heliolineX>
- 3381 Hirata, C., & Seljak, U. 2003, *MNRAS*, 343, 459,
 3382 doi: [10.1046/j.1365-8711.2003.06683.x](https://doi.org/10.1046/j.1365-8711.2003.06683.x)
- 3383 Holman, M. J., Payne, M. J., Blankley, P., Janssen, R., &
 3384 Kuindersma, S. 2018, *AJ*, 156, 135,
 3385 doi: [10.3847/1538-3881/aad69a](https://doi.org/10.3847/1538-3881/aad69a)
- 3386 Howard, J., Reil, K., Claver, C., et al. 2018, in Society of
 3387 Photo-Optical Instrumentation Engineers (SPIE)
 3388 Conference Series, Vol. 10700, Ground-based and
 3389 Airborne Telescopes VII, ed. H. K. Marshall &
 3390 J. Spyromilio, 107003D, doi: [10.1117/12.2312684](https://doi.org/10.1117/12.2312684)
- 3391 Illingworth, G., Magee, D., Bouwens, R., et al. 2016, arXiv
 3392 e-prints, arXiv:1606.00841,
 3393 doi: [10.48550/arXiv.1606.00841](https://doi.org/10.48550/arXiv.1606.00841)
- 3394 Ingraham, P., Fagrelus, P., Stubbs, C. W., et al. 2022, in
 3395 Society of Photo-Optical Instrumentation Engineers
 3396 (SPIE) Conference Series, Vol. 12182, Ground-based and
 3397 Airborne Telescopes IX, ed. H. K. Marshall,
 3398 J. Spyromilio, & T. Usuda, 121820R,
 3399 doi: [10.1117/12.2630185](https://doi.org/10.1117/12.2630185)
- 3400 Ivezić, Ž., Kahn, S. M., Tyson, J. A., et al. 2019a, *ApJ*,
 3401 873, 111, doi: [10.3847/1538-4357/ab042c](https://doi.org/10.3847/1538-4357/ab042c)
- 3402 Ivezić, Ž., Kahn, S. M., Tyson, J. A., et al. 2019b, *ApJ*,
 3403 873, 111, doi: [10.3847/1538-4357/ab042c](https://doi.org/10.3847/1538-4357/ab042c)
- 3404 Jarvis, M., Meyers, J., Leget, P.-F., & Davis, C. 2021a, Piff:
 3405 PSFs In the Full FOV,, Astrophysics Source Code
 3406 Library, record ascl:2102.024 <http://ascl.net/2102.024>
- 3407 Jarvis, M., Bernstein, G. M., Amon, A., et al. 2021b,
 3408 *MNRAS*, 501, 1282, doi: [10.1093/mnras/staa3679](https://doi.org/10.1093/mnras/staa3679)

- 3409 Jenness, T., & Dubois-Felsmann, G. P. 2026, IVOA
3410 Identifier Usage at the Rubin Observatory, Data
3411 Management Technical Note DMTN-302, NSF-DOE Vera
3412 C. Rubin Observatory, doi: [10.71929/rubin/2583848](https://doi.org/10.71929/rubin/2583848)
- 3413 Jenness, T., Voutsinas, S., Dubois-Felsmann, G. P., &
3414 Salnikov, A. 2024, arXiv e-prints, arXiv:2501.00544,
3415 doi: [10.48550/arXiv.2501.00544](https://doi.org/10.48550/arXiv.2501.00544)
- 3416 Jenness, T., Bosch, J. F., Salnikov, A., et al. 2022, in
3417 Society of Photo-Optical Instrumentation Engineers
3418 (SPIE) Conference Series, Vol. 12189, Software and
3419 Cyberinfrastructure for Astronomy VII, 1218911,
3420 doi: [10.1117/12.2629569](https://doi.org/10.1117/12.2629569)
- 3421 Jones, R. L., Yoachim, P., Ivezić, Ž., Neilsen Jr., E. H., &
3422 Ribeiro, T. 2021, Survey Strategy and Cadence Choices
3423 for the Vera C. Rubin Observatory Legacy Survey of
3424 Space and Time (LSST), Project Science Technical Note
3425 PSTN-051, NSF-DOE Vera C. Rubin Observatory,
3426 doi: [10.71929/rubin/2584084](https://doi.org/10.71929/rubin/2584084)
- 3427 Juric, M. 2025, mpsky: Multi-purpose sky catalog
3428 cross-matching, <https://github.com/mjuric/mpsky>
- 3429 Jurić, M., Ciardi, D., Dubois-Felsmann, G., & Guy, L.
3430 2019, LSST Science Platform Vision Document, Systems
3431 Engineering Controlled Document LSE-319, NSF-DOE
3432 Vera C. Rubin Observatory, doi: [10.71929/rubin/2587242](https://doi.org/10.71929/rubin/2587242)
- 3433 Jurić, M., Axelrod, T. S., Becker, A. C., et al. 2023, Data
3434 Products Definition Document, Systems Engineering
3435 Controlled Document LSE-163, NSF-DOE Vera C. Rubin
3436 Observatory, doi: [10.71929/rubin/2587118](https://doi.org/10.71929/rubin/2587118)
- 3437 Kannawadi, A. 2025, Consistent galaxy colors with
3438 Gaussian-Aperture and PSF photometry, Data
3439 Management Technical Note DMTN-190, NSF-DOE Vera
3440 C. Rubin Observatory, doi: [10.71929/rubin/2583849](https://doi.org/10.71929/rubin/2583849)
- 3441 Kron, R. G. 1980, ApJS, 43, 305, doi: [10.1086/190669](https://doi.org/10.1086/190669)
- 3442 Kuijken, K. 2008, A&A, 482, 1053,
3443 doi: [10.1051/0004-6361:20066601](https://doi.org/10.1051/0004-6361:20066601)
- 3444 Lange, T., Nordby, M., Pollek, H., et al. 2024, in Society of
3445 Photo-Optical Instrumentation Engineers (SPIE)
3446 Conference Series, Vol. 13096, Ground-based and
3447 Airborne Instrumentation for Astronomy X, ed. J. J.
3448 Bryant, K. Motohara, & J. R. D. Vernet, 130961O,
3449 doi: [10.1117/12.3019302](https://doi.org/10.1117/12.3019302)
- 3450 Léget, P. F., Astier, P., Regnault, N., et al. 2021, A&A,
3451 650, A81, doi: [10.1051/0004-6361/202140463](https://doi.org/10.1051/0004-6361/202140463)
- 3452 Lim, K.-T. 2023, Proposal and Prototype for Prompt
3453 Processing, Data Management Technical Note
3454 DMTN-219, NSF-DOE Vera C. Rubin Observatory,
3455 doi: [10.71929/rubin/2585429](https://doi.org/10.71929/rubin/2585429)
- 3456 Louys, M., Tody, D., Dowler, P., et al. 2017, Observation
3457 Data Model Core Components, its Implementation in the
3458 Table Access Protocol Version 1.1., IVOA
3459 Recommendation 09 May 2017
3460 doi: [10.5479/ADS/bib/2017ivoa.spec.0509L](https://doi.org/10.5479/ADS/bib/2017ivoa.spec.0509L)
- 3461 LSST Dark Energy Science Collaboration (LSST DESC),
3462 Abolfathi, B., Alonso, D., et al. 2021, ApJS, 253, 31,
3463 doi: [10.3847/1538-4365/abd62c](https://doi.org/10.3847/1538-4365/abd62c)
- 3464 Lupton, R., Blanton, M. R., Fekete, G., et al. 2004, PASP,
3465 116, 133, doi: [10.1086/382245](https://doi.org/10.1086/382245)
- 3466 Lust, N. B., Jenness, T., Bosch, J. F., et al. 2023, arXiv
3467 e-prints, arXiv:2303.03313,
3468 doi: [10.48550/arXiv.2303.03313](https://doi.org/10.48550/arXiv.2303.03313)
- 3469 Mandelbaum, R., Hirata, C. M., Seljak, U., et al. 2005,
3470 MNRAS, 361, 1287,
3471 doi: [10.1111/j.1365-2966.2005.09282.x](https://doi.org/10.1111/j.1365-2966.2005.09282.x)
- 3472 Megias Homar, G., Kahn, S. M., Meyers, J. M., Crenshaw,
3473 J. F., & Thomas, S. J. 2024a, ApJ, 974, 108,
3474 doi: [10.3847/1538-4357/ad6cdc](https://doi.org/10.3847/1538-4357/ad6cdc)
- 3475 Megias Homar, G., Tighe, R., Thomas, S., et al. 2024b, in
3476 Society of Photo-Optical Instrumentation Engineers
3477 (SPIE) Conference Series, Vol. 13094, Ground-based and
3478 Airborne Telescopes X, ed. H. K. Marshall, J. Spyromilio,
3479 & T. Usuda, 130943C, doi: [10.1117/12.3019031](https://doi.org/10.1117/12.3019031)
- 3480 Melchior, P., Moolekamp, F., Jerdee, M., et al. 2018,
3481 Astronomy and Computing, 24, 129,
3482 doi: [10.1016/j.ascom.2018.07.001](https://doi.org/10.1016/j.ascom.2018.07.001)
- 3483 Merritt, S. R., Fedorets, G., Schwamb, M. E., et al. 2025,
3484 AJ, 170, 100, doi: [10.3847/1538-3881/add3ec](https://doi.org/10.3847/1538-3881/add3ec)
- 3485 Mueller, F., Gaponenko, I., Gates, J., et al. 2025, in
3486 Astronomical Society of the Pacific Conference Series,
3487 Vol. 538, Astronomical Data Analysis Software and
3488 Systems XXXII, ed. S. Gaudet, D. Bohlender, S. Gwyn,
3489 A. Hincks, & P. Teuben, 114, doi: [10.26624/XCPI7375](https://doi.org/10.26624/XCPI7375)
- 3490 Naghib, E., Yoachim, P., Vanderbei, R. J., Connolly, A. J.,
3491 & Jones, R. L. 2019, AJ, 157, 151,
3492 doi: [10.3847/1538-3881/aafec](https://doi.org/10.3847/1538-3881/aafec)
- 3493 NSF-DOE Vera C. Rubin Observatory. 2021, Rubin
3494 Observatory LSST Tutorials [Computer Software],
3495 NSF-DOE Vera C. Rubin Observatory,
3496 doi: [10.11578/rubin/dc.20250909.20](https://doi.org/10.11578/rubin/dc.20250909.20)
- 3497 NSF-DOE Vera C. Rubin Observatory. 2025a, Legacy
3498 Survey of Space and Time Data Preview 1 [Data set],
3499 NSF-DOE Vera C. Rubin Observatory,
3500 doi: [10.71929/RUBIN/2570308](https://doi.org/10.71929/RUBIN/2570308)
- 3501 NSF-DOE Vera C. Rubin Observatory. 2025b, Legacy
3502 Survey of Space and Time Data Preview 1: raw dataset
3503 type [Data set], NSF-DOE Vera C. Rubin Observatory,
3504 doi: [10.71929/RUBIN/2570310](https://doi.org/10.71929/RUBIN/2570310)

- 3505 NSF-DOE Vera C. Rubin Observatory. 2025c, Legacy
3506 Survey of Space and Time Data Preview 1: visit_image
3507 dataset type [Data set], NSF-DOE Vera C. Rubin
3508 Observatory, doi: [10.71929/RUBIN/2570311](https://doi.org/10.71929/RUBIN/2570311)
- 3509 NSF-DOE Vera C. Rubin Observatory. 2025d, Legacy
3510 Survey of Space and Time Data Preview 1: deep_coadd
3511 dataset type [Data set], NSF-DOE Vera C. Rubin
3512 Observatory, doi: [10.71929/RUBIN/2570313](https://doi.org/10.71929/RUBIN/2570313)
- 3513 NSF-DOE Vera C. Rubin Observatory. 2025e, Legacy
3514 Survey of Space and Time Data Preview 1:
3515 template_coadd dataset type [Data set], NSF-DOE Vera
3516 C. Rubin Observatory, doi: [10.71929/RUBIN/2570314](https://doi.org/10.71929/RUBIN/2570314)
- 3517 NSF-DOE Vera C. Rubin Observatory. 2025f, Legacy
3518 Survey of Space and Time Data Preview 1:
3519 difference_image dataset type [Data set], NSF-DOE Vera
3520 C. Rubin Observatory, doi: [10.71929/RUBIN/2570312](https://doi.org/10.71929/RUBIN/2570312)
- 3521 NSF-DOE Vera C. Rubin Observatory. 2025g, Legacy
3522 Survey of Space and Time Data Preview 1: Source
3523 searchable catalog [Data set], NSF-DOE Vera C. Rubin
3524 Observatory, doi: [10.71929/RUBIN/2570323](https://doi.org/10.71929/RUBIN/2570323)
- 3525 NSF-DOE Vera C. Rubin Observatory. 2025h, Legacy
3526 Survey of Space and Time Data Preview 1: Object
3527 searchable catalog [Data set], NSF-DOE Vera C. Rubin
3528 Observatory, doi: [10.71929/RUBIN/2570325](https://doi.org/10.71929/RUBIN/2570325)
- 3529 NSF-DOE Vera C. Rubin Observatory. 2025i, Legacy
3530 Survey of Space and Time Data Preview 1: ForcedSource
3531 searchable catalog [Data set], NSF-DOE Vera C. Rubin
3532 Observatory, doi: [10.71929/RUBIN/2570327](https://doi.org/10.71929/RUBIN/2570327)
- 3533 NSF-DOE Vera C. Rubin Observatory. 2025j, Legacy
3534 Survey of Space and Time Data Preview 1: DiaSource
3535 searchable catalog [Data set], NSF-DOE Vera C. Rubin
3536 Observatory, doi: [10.71929/RUBIN/2570317](https://doi.org/10.71929/RUBIN/2570317)
- 3537 NSF-DOE Vera C. Rubin Observatory. 2025k, Legacy
3538 Survey of Space and Time Data Preview 1: DiaObject
3539 searchable catalog [Data set], NSF-DOE Vera C. Rubin
3540 Observatory, doi: [10.71929/RUBIN/2570319](https://doi.org/10.71929/RUBIN/2570319)
- 3541 NSF-DOE Vera C. Rubin Observatory. 2025l, Legacy
3542 Survey of Space and Time Data Preview 1:
3543 ForcedSourceOnDiaObject searchable catalog [Data set],
3544 NSF-DOE Vera C. Rubin Observatory,
3545 doi: [10.71929/RUBIN/2570321](https://doi.org/10.71929/RUBIN/2570321)
- 3546 NSF-DOE Vera C. Rubin Observatory. 2025m, Legacy
3547 Survey of Space and Time Data Preview 1: SSOBJECT
3548 searchable catalog [Data set], NSF-DOE Vera C. Rubin
3549 Observatory, doi: [10.71929/RUBIN/2570335](https://doi.org/10.71929/RUBIN/2570335)
- 3550 NSF-DOE Vera C. Rubin Observatory. 2025n, Legacy
3551 Survey of Space and Time Data Preview 1: SSSource
3552 searchable catalog [Data set], NSF-DOE Vera C. Rubin
3553 Observatory, doi: [10.71929/RUBIN/2570333](https://doi.org/10.71929/RUBIN/2570333)
- 3554 NSF-DOE Vera C. Rubin Observatory. 2025o, Legacy
3555 Survey of Space and Time Data Preview 1: CcdVisit
3556 searchable catalog [Data set], NSF-DOE Vera C. Rubin
3557 Observatory, doi: [10.71929/RUBIN/2570331](https://doi.org/10.71929/RUBIN/2570331)
- 3558 NSF-DOE Vera C. Rubin Observatory. 2025p, Legacy
3559 Survey of Space and Time Data Preview 1: survey
3560 property dataset type [Data set], NSF-DOE Vera C.
3561 Rubin Observatory, doi: [10.71929/RUBIN/2570315](https://doi.org/10.71929/RUBIN/2570315)
- 3562 Oke, J. B., & Gunn, J. E. 1983, ApJ, 266, 713,
3563 doi: [10.1086/160817](https://doi.org/10.1086/160817)
- 3564 O'Mullane, W., Economou, F., Huang, F., et al. 2024a, in
3565 Astronomical Society of the Pacific Conference Series,
3566 Vol. 535, Astronomical Data Analysis Software and Systems
3567 XXXI, ed. B. V. Hugo, R. Van Rooyen, & O. M.
3568 Smirnov, 227, doi: [10.48550/arXiv.2111.15030](https://doi.org/10.48550/arXiv.2111.15030)
- 3569 O'Mullane, W., AlSayyad, Y., Chiang, J., et al. 2024b, in
3570 Society of Photo-Optical Instrumentation Engineers
3571 (SPIE) Conference Series, Vol. 13101, Software and
3572 Cyberinfrastructure for Astronomy VIII, ed. J. Ibsen &
3573 G. Chiozzi, 131012B, doi: [10.1117/12.3018005](https://doi.org/10.1117/12.3018005)
- 3574 Onken, C. A., Wolf, C., Bessell, M. S., et al. 2019, PASA,
3575 36, e033, doi: [10.1017/pasa.2019.27](https://doi.org/10.1017/pasa.2019.27)
- 3576 Park, H. Y., Nomerotski, A., & Tsybychev, D. 2017,
3577 Journal of Instrumentation, 12, C05015,
3578 doi: [10.1088/1748-0221/12/05/C05015](https://doi.org/10.1088/1748-0221/12/05/C05015)
- 3579 Petrosian, V. 1976, ApJL, 210, L53,
3580 doi: [10.1086/18230110.1086/182253](https://doi.org/10.1086/18230110.1086/182253)
- 3581 Plazas, A. A., Shapiro, C., Smith, R., Huff, E., & Rhodes, J.
3582 2018, PASP, 130, 065004, doi: [10.1088/1538-3873/aab820](https://doi.org/10.1088/1538-3873/aab820)
- 3583 Plazas Malagón, A. A., Digel, S. W., Roodman, A., et al.
3584 2026, LSSTCam and LSSTComCam Focal Plane
3585 Layouts, Camera Technical Note CTN-001, NSF-DOE
3586 Vera C. Rubin Observatory, doi: [10.71929/rubin/2584019](https://doi.org/10.71929/rubin/2584019)
- 3587 Plazas Malagón, A. A., Waters, C., Broughton, A., et al.
3588 2025, Journal of Astronomical Telescopes, Instruments,
3589 and Systems, 11, 011209,
3590 doi: [10.1117/1.JATIS.11.1.011209](https://doi.org/10.1117/1.JATIS.11.1.011209)
- 3591 Porter, M. N., Tucker, D. L., Smith, J. A., & Adair, C. L.
3592 2026, Photometric Transformation Relations for the
3593 LSST Data Preview 1, Technical Note RTN-099,
3594 NSF-DOE Vera C. Rubin Observatory,
3595 doi: [10.71929/rubin/3006074](https://doi.org/10.71929/rubin/3006074)
- 3596 Refregier, A. 2003, ARA&A, 41, 645,
3597 doi: [10.1146/annurev.astro.41.111302.102207](https://doi.org/10.1146/annurev.astro.41.111302.102207)
- 3598 Reiss, D. J., & Lupton, R. H. 2016, Implementation of
3599 Image Difference Decorrelation, Data Management
3600 Technical Note DMTN-021, NSF-DOE Vera C. Rubin
3601 Observatory, doi: [10.71929/rubin/2586490](https://doi.org/10.71929/rubin/2586490)

- Roodman, A., Rasmussen, A., Bradshaw, A., et al. 2024, in Society of Photo-Optical Instrumentation Engineers (SPIE) Conference Series, Vol. 13096, Ground-based and Airborne Instrumentation for Astronomy X, ed. J. J. Bryant, K. Motohara, & J. R. D. Vernet, 130961S, doi: [10.1117/12.3019698](https://doi.org/10.1117/12.3019698)
- Rubin, V. C., & Ford, Jr., W. K. 1970, *ApJ*, 159, 379, doi: [10.1086/150317](https://doi.org/10.1086/150317)
- Rubin, V. C., Ford, Jr., W. K., & Thonnard, N. 1980, *ApJ*, 238, 471, doi: [10.1086/158003](https://doi.org/10.1086/158003)
- Rubin Observatory Science Pipelines Developers. 2025, The LSST Science Pipelines Software: Optical Survey Pipeline Reduction and Analysis Environment, Project Science Technical Note PSTN-019, NSF-DOE Vera C. Rubin Observatory, doi: [10.71929/rubin/2570545](https://doi.org/10.71929/rubin/2570545)
- Rubin's Survey Cadence Optimization Committee, Bauer, F. E., Brough, S., et al. 2022, Survey Cadence Optimization Committee's Phase 1 Recommendation, Project Science Technical Note PSTN-053, NSF-DOE Vera C. Rubin Observatory, doi: [10.71929/rubin/2584276](https://doi.org/10.71929/rubin/2584276)
- Rubin's Survey Cadence Optimization Committee, Bauer, F. E., Bianco, F. B., et al. 2023, Survey Cadence Optimization Committee's Phase 2 Recommendations, Project Science Technical Note PSTN-055, NSF-DOE Vera C. Rubin Observatory, doi: [10.71929/rubin/2585249](https://doi.org/10.71929/rubin/2585249)
- Rubin's Survey Cadence Optimization Committee, Bianco, F. B., Jones, R. L., et al. 2025, Survey Cadence Optimization Committee's Phase 3 Recommendations, Project Science Technical Note PSTN-056, NSF-DOE Vera C. Rubin Observatory, doi: [10.71929/rubin/2585402](https://doi.org/10.71929/rubin/2585402)
- Rykoff, E. S., Tucker, D. L., Burke, D. L., et al. 2023, arXiv e-prints, arXiv:2305.01695, doi: [10.48550/arXiv.2305.01695](https://doi.org/10.48550/arXiv.2305.01695)
- Saunders, C. 2024, Astrometric Calibration in the LSST Pipeline, Data Management Technical Note DMTN-266, NSF-DOE Vera C. Rubin Observatory, doi: [10.71929/rubin/2583846](https://doi.org/10.71929/rubin/2583846)
- Schutt, T., Jarvis, M., Roodman, A., et al. 2025, *The Open Journal of Astrophysics*, 8, 26, doi: [10.33232/001c.132299](https://doi.org/10.33232/001c.132299)
- Sérsic, J. L. 1963, *Boletín de la Asociación Argentina de Astronomía La Plata Argentina*, 6, 41
- Sersic, J. L. 1968, *Atlas de Galaxias Australes (Cordoba, Argentina: Observatorio Astronomico)*
- Shanks, T., Metcalfe, N., Chehade, B., et al. 2015, *MNRAS*, 451, 4238, doi: [10.1093/mnras/stv1130](https://doi.org/10.1093/mnras/stv1130)
- SLAC National Accelerator Laboratory, & NSF-DOE Vera C. Rubin Observatory. 2024, LSST Commissioning Camera, SLAC National Accelerator Laboratory (SLAC), Menlo Park, CA (United States), doi: [10.71929/RUBIN/2561361](https://doi.org/10.71929/RUBIN/2561361)
- Slater, C. T., Ivezić, Ž., & Lupton, R. H. 2020, *AJ*, 159, 65, doi: [10.3847/1538-3881/ab6166](https://doi.org/10.3847/1538-3881/ab6166)
- Smith, G. E. 2010, *Reviews of Modern Physics*, 82, 2307, doi: [10.1103/RevModPhys.82.2307](https://doi.org/10.1103/RevModPhys.82.2307)
- Stalder, B., Reil, K., Claver, C., et al. 2020, in Society of Photo-Optical Instrumentation Engineers (SPIE) Conference Series, Vol. 11447, Ground-based and Airborne Instrumentation for Astronomy VIII, ed. C. J. Evans, J. J. Bryant, & K. Motohara, 114470L, doi: [10.1117/12.2561132](https://doi.org/10.1117/12.2561132)
- Stalder, B., Reil, K., Aguilar, C., et al. 2022, in Society of Photo-Optical Instrumentation Engineers (SPIE) Conference Series, Vol. 12184, Ground-based and Airborne Instrumentation for Astronomy IX, ed. C. J. Evans, J. J. Bryant, & K. Motohara, 121840J, doi: [10.1117/12.2630184](https://doi.org/10.1117/12.2630184)
- Stalder, B., Munoz, F., Aguilar, C., et al. 2024, in Society of Photo-Optical Instrumentation Engineers (SPIE) Conference Series, Vol. 13094, Ground-based and Airborne Telescopes X, ed. H. K. Marshall, J. Spyromilio, & T. Usuda, 1309409, doi: [10.1117/12.3019266](https://doi.org/10.1117/12.3019266)
- Swinbank, J. D., Axelrod, T. S., Becker, A. C., et al. 2020, Data Management Science Pipelines Design, Data Management Controlled Document LDM-151, NSF-DOE Vera C. Rubin Observatory, doi: [10.71929/rubin/2587108](https://doi.org/10.71929/rubin/2587108)
- Taranu, D. S. 2025, The MultiProFit astronomical source modelling code, Data Management Technical Note DMTN-312, NSF-DOE Vera C. Rubin Observatory, doi: [10.71929/rubin/2584108](https://doi.org/10.71929/rubin/2584108)
- Taylor, M. 2011, TOPCAT: Tool for Operations on Catalogues And Tables, Astrophysics Source Code Library, record ascl:1101.010
- Thomas, S., Connolly, A., Crenshaw, J. F., et al. 2023, in Adaptive Optics for Extremely Large Telescopes (AO4ELT7), 67, doi: [10.13009/AO4ELT7-2023-069](https://doi.org/10.13009/AO4ELT7-2023-069)
- Tonry, J. L., Denneau, L., Heinze, A. N., et al. 2018, *PASP*, 130, 064505, doi: [10.1088/1538-3873/aabadf](https://doi.org/10.1088/1538-3873/aabadf)
- Wainer, T. M., Davenport, J. R. A., Bellm, E. C., et al. 2025, *Research Notes of the American Astronomical Society*, 9, 171, doi: [10.3847/2515-5172/adecef](https://doi.org/10.3847/2515-5172/adecef)
- Wang, D. L., Monkewitz, S. M., Lim, K.-T., & Becla, J. 2011, in *State of the Practice Reports, SC '11* (New York, NY, USA: ACM), 12:1–12:11, doi: [10.1145/2063348.2063364](https://doi.org/10.1145/2063348.2063364)
- Waters, C. Z., Magnier, E. A., Price, P. A., et al. 2020, *ApJS*, 251, 4, doi: [10.3847/1538-4365/abb82b](https://doi.org/10.3847/1538-4365/abb82b)
- Whitaker, K. E., Ashas, M., Illingworth, G., et al. 2019, *ApJS*, 244, 16, doi: [10.3847/1538-4365/ab3853](https://doi.org/10.3847/1538-4365/ab3853)

- 3700 Wu, X., Roby, W., Goldian, T., et al. 2019, in *Astronomical*
3701 *Society of the Pacific Conference Series*, Vol. 521,
3702 *Astronomical Data Analysis Software and Systems*
3703 *XXVI*, ed. M. Molinaro, K. Shortridge, & F. Pasian, 32
- 3704 Xin, B., Claver, C., Liang, M., et al. 2015, *ApOpt*, 54,
3705 9045, doi: [10.1364/AO.54.009045](https://doi.org/10.1364/AO.54.009045)
- 3706 Yoachim, P. 2022, *Survey Strategy: Rolling Cadence*,
3707 *Project Science Technical Note PSTN-052*, NSF-DOE
3708 *Vera C. Rubin Observatory*, doi: [10.71929/rubin/2584109](https://doi.org/10.71929/rubin/2584109)
- 3709 Yoachim, P., Jones, L., Eric H. Neilsen, J., & Becker, M. R.
3710 2024, *lsst/rubin_scheduler: v3.0.0*, v3.0.0 Zenodo,
3711 doi: [10.5281/zenodo.13985198](https://doi.org/10.5281/zenodo.13985198)
- 3712 Zhang, T., Almoubayyed, H., Mandelbaum, R., et al. 2023,
3713 *MNRAS*, 520, 2328, doi: [10.1093/mnras/stac3350](https://doi.org/10.1093/mnras/stac3350)